Influence of Cu Nano-Layer on Nonlinear Optical Response of BTO, STO and BST Thin Films Fabricated via Pulsed Laser Deposition

DOCTOR OF PHILOSOPHY

by

SASMITA BEHERA

DEPARTMENT OF PHYSICS

INDIAN INSTITUTE OF TECHNOLOGY GUWAHATI

GUWAHATI -781039, INDIA

DECEMBER 2021

Influence of Cu Nano-Layer on Nonlinear Optical Response of BTO, STO and BST Thin Films Fabricated via Pulsed Laser Deposition

A Thesis submitted in partial fulfillment of the requirements for the award of the degree of

DOCTOR OF PHILOSOPHY

by

SASMITA BEHERA

DEPARTMENT OF PHYSICS

INDIAN INSTITUTE OF TECHNOLOGY GUWAHATI

GUWAHATI -781039, INDIA

DECEMBER 2021

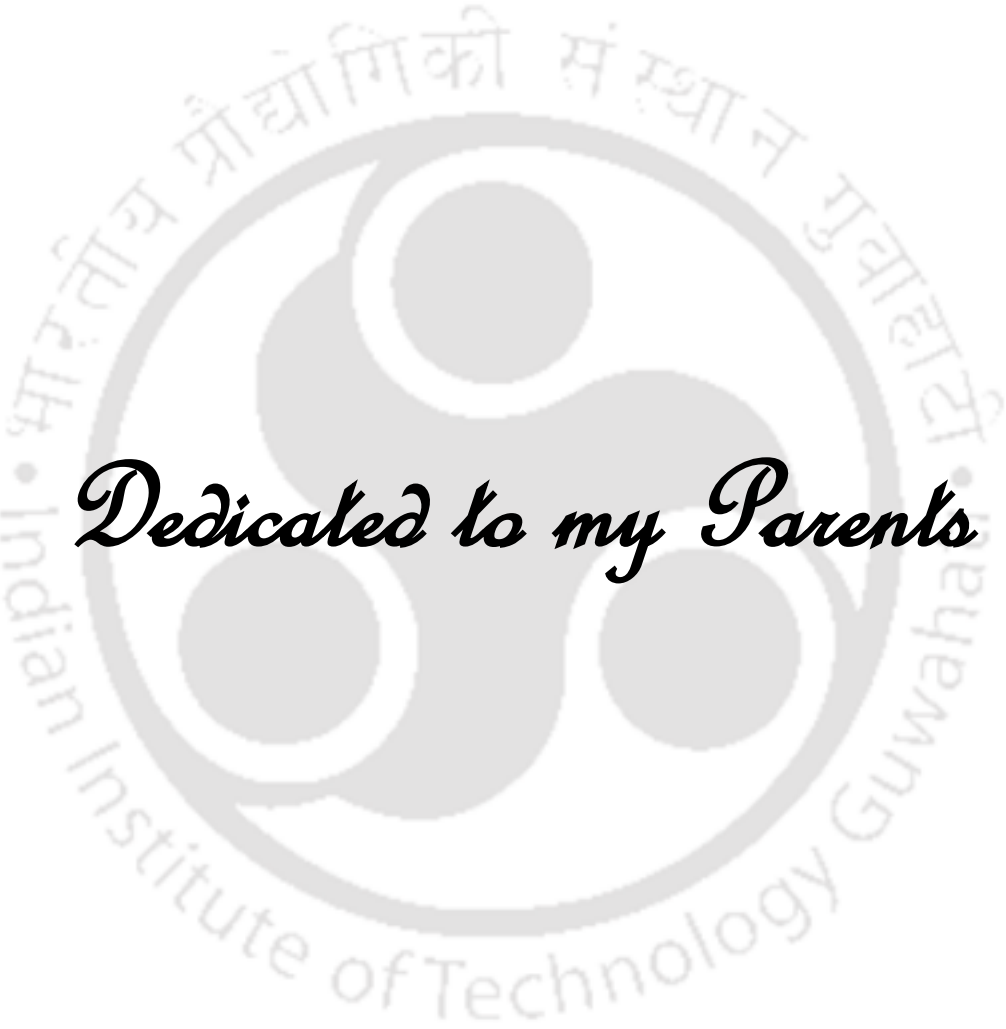

Dedicated to my Parents

Sasmita Behera
Registration No. 146121030
Department of Physics
Indian Institute of Technology Guwahati
Guwahati-781039, Assam, India

Statement

I hereby declare that the matter embodied in this thesis is the result of investigations carried out by me at the Department of Physics, Indian Institute of Technology Guwahati, Guwahati, India, under the supervision of **Prof. Alika Khare**. This thesis has not been submitted to any university, institute or elsewhere for the award of the any degree, diploma or associate-ship.

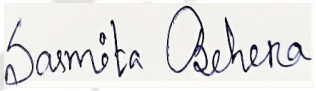

Date 30/05/2022 **Sasmita Behera**

भारतीय प्रौद्योगिकी संस्थान गुवाहाटी
Indian Institute of Technology Guwahati
Department of Physics
Guwahati-781039, Assam State, INDIA
Phone: +91 361 2582705, 2582750, 2690321 to 328 (extn. 2705),
Fax: +91 361 2582749
Dr. Alika Khare
Professor
E-mail: alika@iitg.ac.in, k_alika@yahoo.com

Date: Dec 22, 2021

Certificate

This is to certify that work contained in the thesis entitled '**Influence of Cu Nano-layer on Nonlinear optical response of BTO, STO and BST Thin Films fabricated via Pulsed Laser Deposition'** by **Ms Sasmita Behera** (Roll no 146121030), a student of Department of Physics, Indian Institute of Technology Guwahati, for the award of degree of Doctor of Philosophy, has been carried out under my supervision and the same has not been submitted elsewhere for the award of any other degree.

(Alika Khare)

Acknowledgement

First and foremost, I would like to thank my thesis supervisor, Prof. Alika Khare, for giving me opportunity to work under her supervision and for her constant support, precious advice and valuable suggestions which helped me to complete my thesis work. Even, during the tough period of the completion of thesis work, she was kind enough and understood the situation and helped in to overcome the mental tension.

I am also very grateful to my doctoral committee members, Prof. Amarendra Kumar Sarma, Dr. D. Pamu, Prof. Jubaraj Baruah for their timely reviewing and giving me necessary suggestions to improve my work. Their valuable suggestions are helped me to improve the work to shape the present thesis.

I am also taking the opportunity to thank the present and former head of department of Physics, IIT Guwahati and head of the central instrumental facility for providing me the necessary facilities to fulfil my PhD thesis objectives. I sincerely extend my gratitude to all the faculty members of the Department of Physics, who supported me in helping me in several ways during my PhD tenure. I would like to extend my sincere thanks to Dr. Sidananda Sarma, technical and nontechnical staffs of IIT Guwahati to help me with various instruments operations.

I sincerely thank University Grants Commission (UGC), New Delhi for financial assistance. I specially would like to acknowledge the Equal Opportunity Cum Special Reservation Cell, IIT Guwahati for the financial assistance.

It was lifetime good experience and pleasure to work with my research lab members Dr. Indrajit, Dr. Partha, Dr. Shanta Kumar, Dr. Gyan Prakash, Dr. Rahul, Dr. Prahlad, Dr. Eshita, Dr. Gobinda, Sumit and Nagendra. I want to special thank seniors for their suggestions, helped me learning basics of the instrument and teach me to handle the instrument.

Friends I have met in IIT Guwahati; Jhulan, Sagarika, Dr. Jagan, Dr. Jyoti, Dr. Monika, Dr. Sunayana, Dr. Aakhansa, Dr. Indu, Dr. Ranjan, Dr. Joy, Dr. Gobinda, Dr. Goutam, Dr. Nawaz, Dr. Kishor,Shyam are invaluable to me. I also met some juniors inside the campus; Sumit, Nagendra,

Karuna, Sunil, Pilik, Juhi, Manavendra, Jayshree, Prajna, Dhriti, Susmita, Anupama, Shashi, Apurba, Abhishek, Archana, Sudarshan, Pooja, Ankan, Lwithwsa, Vikash who made my life enjoyable outside the lab by giving me love and constant support during my PhD, whenever I needed. I must acknowledge Eshita di, Pallavi, Sneha, Subhashree, Raju and Rajesh for their unconditional love, affection, encouragements to push me move ahead in my life.

My special gratitude goes to my family members; Father-in-Law Anand Chandra Mahakul, Mother-in-Law Pramila Mahakul, Brother Goutam Kumar Behera, Sister-in-Law Swapnashree Pardhi, Archana Mahakul, Niece Parul Princy, and Nephew OM for their love and constant support in my life. I thank my father Late Dayanidhi Behera, mother Late Kanchan Bala Behera having faith in me and have blessing always in my life. I miss them always for every steps of my life. Last, but not the least I want to thank my love of my life my dear husband Ashish Kumar Mahakul for his love, care, trust and encouragement in every step. I don't have any words to express what their support and love mean to me throughout this journey. Finally, I owe my sincere gratitude to Almighty God who gives me always a positive energy to face every problem of my life.

Sasmita Behera

Abstract

The present thesis was focused on the fabrication and characterization of perovskite thin films of $BaTiO_3$, $SrTiO_3$, $Ba_{1-x}Sr_xTiO_3$ ($0 \leq x \leq 1$) via pulsed laser deposition (PLD) technique. The optimized substrate temperature and background oxygen pressure were found to be 700 °C and 0.1 mbar, respectively. The morphology, structural, linear, and nonlinear optical properties of all thin films were studied by AFM and FESEM, XRD, Raman, UV-Visible-NIR spectroscopy, and modified *Z*-scan technique. The values of nonlinear absorption coefficient (β) for $BaTiO_3$, $SrTiO_3$, and $Ba_{0.5}Sr_{0.5}TiO_3$ thin films fabricated at optimized conditions were found to be (57.54 ± 0.05), (63.51 ± 0.13), (73.24 ± 0.32) cm/W, respectively. It has already been known that the NLO properties can be further enhanced by embedding with metallic nanoparticles. Therefore, the effect of Cu nano-layer on structural, linear, and nonlinear optical properties of host matrix of $BaTiO_3$, $SrTiO_3$, and $Ba_{0.5}Sr_{0.5}TiO_3$ thin films have been studied and observed that the sequence of Cu nano-layer is important for SPR and enhancement in NLO properties. The nonlinear absorption coefficients (β) of Cu infused $BaTiO_3$, $SrTiO_3$, and $Ba_{0.5}Sr_{0.5}TiO_3$ thin films were found to be (155.04 ± 5.39), (182.34 ± 7.23) and (188 ± 0.45) cm/W, respectively. The values of the third-order nonlinear optical coefficients (β, n_2, and $\chi^{(3)}$) in $Ba_{1-x}Sr_xTiO_3$ ($0 \leq x \leq 1$) thin films were found to be in the range of (64.74 – 74.85) cm/W, (0.18– 6.35) $\times 10^{-3}$ cm^2/W and (12.43-63.11) $\times$ 10^{-4} esu, respectively. The optical limiting response of $BaTiO_3$, $SrTiO_3$, and $Ba_{0.5}Sr_{0.5}TiO_3$ thin films deposited on quartz and MgO substrates was analysed and measured the optical limiting threshold as well. The obtained high third-order nonlinearity and low optical limiting threshold in present films are promising for optoelectronics and photonics devices and can be used as optical limiters and optical switching applications.

Contents

List of Figures

List of Tables

Abbreviation

AFM	Atomic Force Microscopy
Ar.Ion	Argon Ion
Arb. unit	Arbitrary Unit
BTO	$BaTiO_3$
BST-0.3	$Ba_{0.7}Sr_{0.3}TiO_3$
BST-0.4	$Ba_{0.6}Sr_{0.4}TiO_3$
BST-0.5	$Ba_{0.5}Sr_{0.5}TiO_3$
BST-0.7	$Ba_{0.3}Sr_{0.7}TiO_3$
CA	Close aperture
CCD	Charge coupled device
cw	Continuous wave
EHT	Electron high tension
EDX	Energy dispersive X-ray
FE	Ferroelectric
FESEM	Field emission scanning electron microscopy
FWHM	Full width at half maximum
Kg	Kilogram
LIP	Laser induced plasma
LO	Longitudinal optical mode
MBE	Molecular beam epitaxy
Nd:YAG	Neodymium Yttrium Aluminium Garnet
NIR	Near infrared
NLO	Nonlinear optical
NP	Nanoparticle
O_2	Oxygen partial pressure
OA	Open aperture
OL	Optical limiting
OPA	Optical Parametric amplification
PLD	Pulsed laser deposition

PL	Photoluminescence
RMS	Root mean square
RT	Room temperature
RSA	Reverse saturation absorption
SPs	Surface plasmons
SPR	Surface plasmon resonance
SA	Saturation absorption
STO	$SrTiO_3$
T_s	Substrate temperature
TO	Transverse optical mode
TPA	Two photon absorption
UV	Ultraviolet
viz.	Namely
Vis	Visible
Wt.	Weight
w.r.t.	With respect to
XRD	X-Ray diffraction

Symbols

~	Approximately	P_0	Power measured before the sample
α	Absorption coefficient	L_{eff}	Effective thickness of the thin film
θ	Angle	λ	Wavelength
Å	Angstrom	At%	Atomic percentage
a, b, c	Lattice parameters	σ	Stress
β	Nonlinear absorption coefficient	s	Strain
c	Velocity of light	$h\nu$	Photon energy
D	Crystallite Size	V	Unit cell volume
^{o}C	Centigrade (degree)	μm	Micrometer
eV	Electron volt	Cu	Copper
E_g	Optical bandgap	Ag	Silver
esu	Electrostatic unit	Au	Gold
ε_0	Free space permittivity	Fe	Iron
ε_{m2}	Imaginary part of metal dielectric function	Ni	Nickel
ε_{m1}	Real part of metal dielectric function	Rh	Rhodium
ε_m	Metal dielectric constant	n	Refractive index
f	Focal length	n_d	Refractive index of dielectric
GPa	Giga pascal	n_0	Complex refractive index
gm	Gram	n_2	Nonlinear refractive index coefficient
h	Planck's constant	n_0'	Imaginary part of linear refractive index coefficient
h, k, l	Miller indices	n_2'	Imaginary part of nonlinear refractive index coefficient
I_0	Incident light intensity	n_s	Refractive index of quartz substrate

I_c	Intensity at the center of focus point	mm	Milimeter
I_{input}	Input intensity of the sample	mbar	milibar
J	Joule	min	minute
k	wave vector	hr.	Hour
L	Thickness of thin film	S	Aperture size
$\chi^{(3)}$	Third order nonlinear susceptibility	Si	Silicon
$\chi_R^{(3)}$	Real part of third order nonlinear susceptibility	cm	Centimeter
$\chi_I^{(3)}$	Imaginary part of third order nonlinear susceptibility	μm	Micrometer
$\chi_{complex}^{(3)}$	Complex third order nonlinear susceptibility	m	Meter
T_C	Curie temperature	nm	Nanometer
T_s	Substrate temperature	W	Watt
T_{close}	Close aperture transmission	ω_0	Beam waist
T_{open}		$\omega(z)$	Beam radius
T_{max}	Transmission maxima of transmission spectra	wt %	Weight percentage
T_{min}	Transmission minima of transmission spectra	z_f	Focus of the lens
Cu_2O	Cuprous oxide	z_0	Rayleigh length
CuO	Cupric oxide	z	Sample position w.r.t focus

Chapter 1 : Introduction

Nowadays, nanocomposite dielectric thin films implanted with metal nanoparticles are in the spotlight owing to specific exceptional properties that lead to several device applications in miniaturized form with a great degree of precision. The performance of these nanocomposite thin film-based devices are highly dependent on thickness, surface conditioning, plasmonic behavior, linear, and nonlinear optical properties, and electrical properties [1-3]. The infusion of metallic nano-layer (e.g., copper (Cu), silver (Ag), gold (Au), nickel (Ni), rhodium (Rh), iron (Fe), etc.) in the dielectric films enhances its property by orders of magnitude within the plasmonic structure [4-12]. Therefore, various light-matter interaction processes are significantly improved, including photoluminescence (PL) response, Raman scattering, photocatalysis, heat generation, and optical nonlinearity.

The nanoparticles of noble metals (Cu, Ag, and Au) fabricated onto the suitable dielectric matrix exhibit the surface plasmons (SPs) phenomena [9, 13, 14]. SPs are the collective oscillations of the free conduction electrons at the metal-dielectric interface and confined on the metallic surface, which decays exponentially in the neighboring media [15]. The resonant interaction between electrons near the surface of the metal and the electromagnetic field of the incident radiation results in a phenomenon called surface plasmon resonance (SPR) [16]. The importance of the SPR originates from its ability to absorb and scatter the incident light in both the UV and visible regions. The nonlinear optical (NLO) property is also greatly enhanced near SPR frequency by amplification of local electric field in that region [17]. However, the nonlinearity of the noble metals is due to the contribution of

intraband transition, interband transition, and hot electron formation (plasmon-enhanced photon absorption) [18].

Furthermore, SPR possess a fast response time of the order of picosecond. Therefore, it is the root cause of near-field spectroscopy, surface-enhanced Raman spectroscopy (SERS), enormously large data storage, sensors, improved efficiency of solar cells, etc. [15, 19]. Also, it can be utilized to fabricate the fast plasmonics circuits, bio-sensors, plasmonic chips, etc. It offers promising applications involving all photonic devices, waveguides, optical switching devices, etc., due to its excellent NLO properties and ultrafast response time [20-22]. The SPR and NLO properties depend on the nanoparticle size, shape, type of surrounding dielectric material, interfacial layer, and composition of the metallic thin film [23, 24]. Among various noble metals exhibiting SPR, Cu metal is an inexpensive one and is mainly used in electrical and plasmonic devices simultaneously. Thereby, a single chip can be foreseen to carry the electrical and optical information simultaneously [2, 25]. It is also used in optoelectronic devices as optical limiters due to both saturation absorption and reverse saturation absorption behavior [13, 26, 27]. Besides its NLO properties, it has a plethora of applications in the area of medicine, electronics, manufacturing of lubrication nanofluids, filler, conductive films, antimicrobial, antiseptic material, metallic inks, wound dressing and biocidal properties, gas sensors, catalytic process, high-temperature superconductors, high-speed devices, solar cells [28-34], etc.

The host dielectric matrix greatly impacts SPR properties, the perovskite materials stand very well in this regard as a suitable dielectric host. Perovskite materials have been extensively studied in bulk and the thin film forms for their outstanding response for ferroelectric, piezoelectric, nonlinear optical properties, and electro-optic applications [35-37].

1.1 Structure of perovskite

Perovskites name was coined after the scientist Count Lev Aleksevich Von Perovskite, who identified the structure of the calcium titanium oxide ($CaTiO_3$). This was first discovered in the Ural Mountains of Russia by Gustav Rose in 1839 [38]. Thereafter, it is named after a Russian nobleman and mineralogist Count Lev Aleksevich Von Perovskite [39]. Perovskites have the general formula ABX_3 where A and B are two cations of very different sizes and X is an anion that bonds with two cations [40]. X is often oxygen but can also be other large ions such as halides, sulfides, and nitrides. The perovskite structures exist in different forms such as: ABO_3-perovskite (e.g.: $BaTiO_3$ (BTO), $CaTiO_3$, $SrTiO_3$ (STO), and $Ba_{1-x}Sr_xTiO_3$ ($0 \leq x \leq 1$) (BST)), A_2BO_4-Layered perovskite (e.g.: Sr_2RuO_4, K_2NiF_4), $A_2BB'O_6$-Double perovskite (e.g.: Ba_2TiRuO_6) and $A_2A'B_2B'O_9$-Triple perovskite (e.g.: $La_2SrCo_2FeO_9$), etc.[41-43]. But, perovskite of the form ABO_3, is one of the most frequently encountered structures in solid-state physics, and it accommodates most of the metal ions in the periodic table with a significant number of different anions. It exhibits notable physical characteristics of large spontaneous polarization, high dielectric constant, high optical transparency, and large nonlinear response. The schematic of the ideal cubic structure with ABO_3 perovskite per unit cell is shown in Figure 1-1. Among perovskite oxide material, thin films of BTO, STO, and BST have attracted considerable attention for their remarkable structure, properties, and wide range of applications.

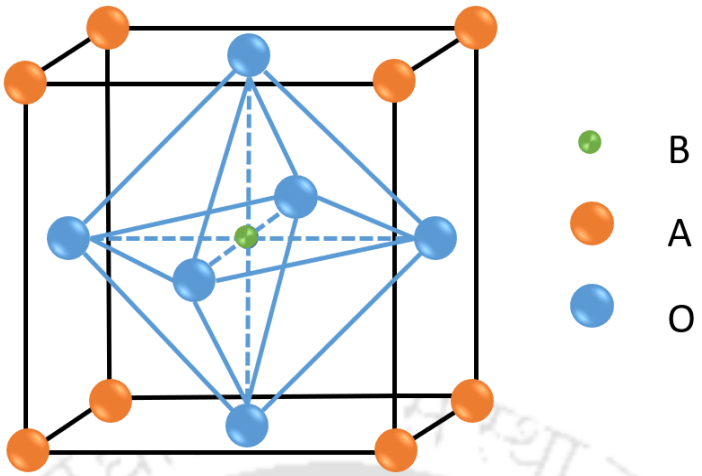

Figure 1-1 *Schematic of ideal cubic structure with ABO_3 perovskite.*

1.1.1 Barium titanate (BTO) thin films

BTO thin films have garnered considerable attention over the past decades owing to their excellent dielectric, ferroelectric, and nonlinear optical properties. Since the discovery of BTO by Wul and Goldman in 1945, the bulk physical properties and crystal structure of BTO have been intensively investigated [44]. Wainer and Solomon identified BTO as a high dielectric constant ferroelectric material [38]. In BTO, the Ba^{2+} cations are located on the A site whereas Ti^{4+} at B sites as shown in Figure 1-1. In addition, the coordination number of Ba^{2+} ions is 12, while that of Ti^{4+} is 6. The Barium (Ba) and Oxygen (O) ions form an FCC lattice in bulk BTO crystal. The Ti^{4+} ions reside in octahedral interstitial positions coordinated by six O^{2-} ions. The octahedral interstitial position is large compared to the size of the Ti^{4+} ions. Thereby, Ti^{4+} ions are too small to be stable in [TiO_6], an octahedral position having 4+ charges. The Titanium (Ti) ions can easily shift from random to aligned positions by applying an electric field which results in high bulk polarization. It also undergoes temperature-dependent phase transition from rhombohedral *3m* phase at 183 K to an orthorhombic *mm2* phase at 278 K, a tetragonal *4mm* phase at 293 K, and finally to cubic *m3m* phase at 403 K [45]. It behaves like ferroelectric

in the three low-temperature phases (rhombohedral, orthorhombic, and tetragonal) whereas paraelectric in the cubic phase [35]. Crystal structure symmetry and variation of the cube root of the cell volume with temperature for various phases of BTO are shown in Figure 1-2 (a) - (b), respectively. BTO has a direct bandgap of 3.2 eV, but it can change its nature of bandgap depending on the strain and disorder present in the thin films [46]. Its tetragonal (noncentrosymmetric) and cubic phases (centrosymmetric) show numerous nonlinear effects such as second harmonic generation, two-wave mixing, four-wave mixing, and slowing down of light, etc., at room temperature [47-49].

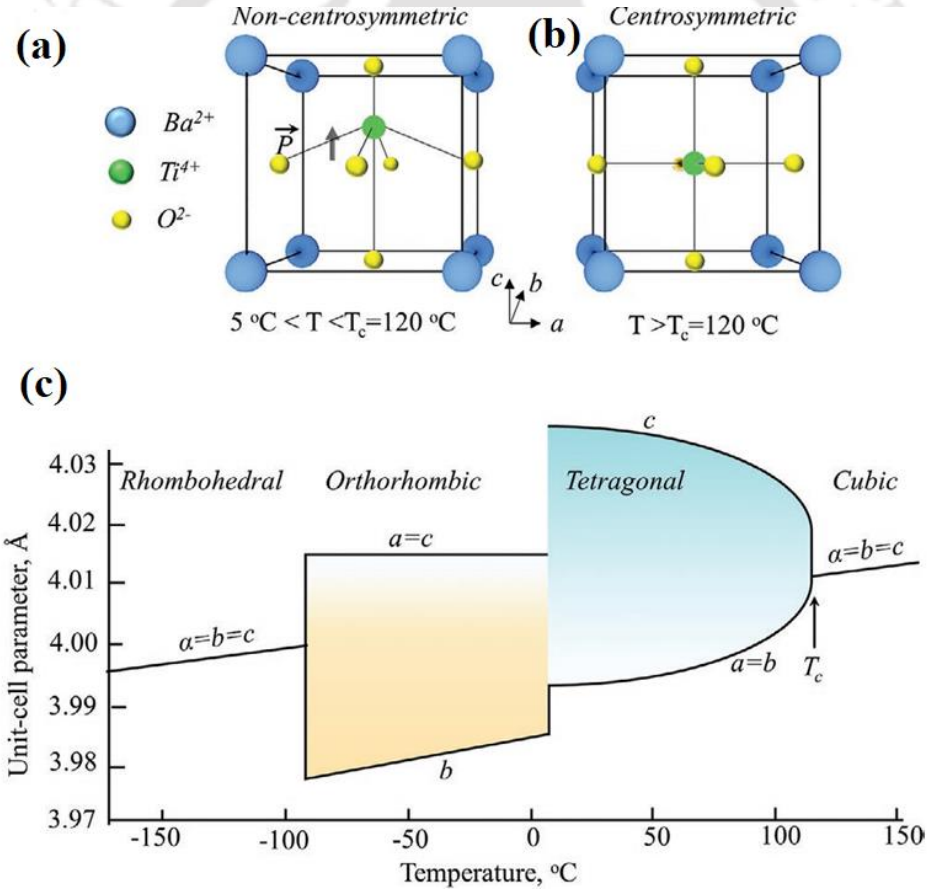

Figure 1-2 *Crystal structure symmetry and temperature-phase diagram of $BaTiO_3$. (a) The noncentrosymmetric unit cell structure of $BaTiO_3$ for tetragonal phase (below Curie temperature), (b) centrosymmetric unit cell structure of $BaTiO_3$ for cubic phase (above Curie temperature), (c) variation of the cube root of the volume of the cell with temperature for various phases of $BaTiO_3$ [1].*

In addition, the thin films of BTO have a large electro-optic coefficient (r_{51} =1640 pm/V), low optical losses, and excellent optical transparency in the visible to near-infrared region, and remarkable phase conjugate reflectivity [50-52]. It is a good material platform to be utilized in various ways such as photonic waveguides due to small optical losses, photonic metasurfaces, photonic crystals, and photonic bandgap, owing to the large refractive index (n = 2.45 at 550 nm) in comparison with commonly available substrates, e.g., quartz [44]. To improve the functional qualities; modify the structure, tuning of linear and nonlinear optical properties, and extend the areas of application of BTO, different doping elements have been employed to occupy A or the B site [36, 53-55]. Due to doping, BTO alters its structure and morphology, and it becomes the origin of PL in thin films [56-59]. There are few articles reporting the extrinsic and intrinsic defects, self-trapped exciton, and free excitons responsible for PL emissions in BTO thin films [60, 61].

1.1.2 Strontium titanate (STO) thin films

STO, another member of the perovskite family similar to BTO, is an important dielectric material having ferroelectric transition (tetragonal phase – cubic phase) at 110 K. STO is also considered as an ideal perovskite having a lattice parameter of 3.905 Å and exhibits a high static dielectric constant at room temperature (RT). It has a cubic phase with a $P_{m\text{-}3m}$ space group. In this cubic structure, Ti ions are located at corners, whereas Strontium (Sr) ion is body-centered (BC). The oxygen is face-centered at twelve edges of the cube, which gives shared corner strings of TiO_6 octahedral, and it extends in three dimensions. Above transition temperature of 110 K, STO remains in a single stable cubic phase. The indirect bandgap for the bulk is 3.25 eV at RT, while the direct bandgap is about 3.75 eV. The bandgap originates from separating the dominant O 2*p* states (a little contribution arises from Ti 3*d* states) and the

hybridized O 2*p* –Ti 3*d* states [62]. A high dielectric constant, excellent optical properties and a simple cubic structure with stable stoichiometry above the transition temperature of 110 K, STO has attracted attention in the form of thin films, having prospective applications in microelectronics and optoelectronic fields. Due to a favorable lattice match, STO is one of the most widely used substrate materials for the epitaxial synthesis of other perovskite systems [63]. STO is combined with other perovskites in fabricating heterostructures and superlattices that yield artificial materials with entirely tailor-made properties with enhanced ferroelectric polarization [64, 65]. In addition, the optical properties of ferroelectric BTO and paraelectric STO multilayer structures are investigated as a possible material choice for thin-film electro-optic devices. The electro-optic (EO) coefficient (r_{33}) of the BTO-STO superlattice is about 72 pm/V which is higher than that of BTO thin film of thickness ~ 400 nm having r_{33} = 23 pm/V [66]. The third-order optical properties of STO thin films are investigated under nanosecond laser using the *Z*-scan technique. These films have a high nonlinear absorption coefficient (β) and nonlinear refractive index coefficient (n_2) compared to BTO thin films [67]. The picosecond third-order optical nonlinearities of noble Au and Ni nanoparticles embedded in STO matrices are investigated using the single-beam Z-scan technique [68]. These nanocomposite STO thin films have potential applications in optical processing, computing, and optical limiters due to high Figure of Merit (FOM) values.

1.1.3 Barium strontium titanate (BST) thin films

Another perovskite material, $Ba_{1-x}Sr_xTiO_3$ ($0 \leq x \leq 1$), BST, is formed by alloying of BTO and STO in the proper portions to obtain the desired stoichiometric balance, by variation of Sr concentration (*x*). BST material is non-volatile and easy to fabricate. BST is of great importance; it takes advantage of the high dielectric constant of BTO and the structural stability

of STO simultaneously. BST thin films have high transparency in the visible and infrared wavelength range, a relatively high refractive index, a unique combination of electro-optical coefficient, and low optical losses of both constituents. Moreover, the above characteristics of BST could be widely utilized for its ferroelectric, pyroelectric, and electro-optical properties because it allows a wide range of properties depending on the different concentrations of Sr. Moreover, BST is currently one of the most interesting ferroelectric materials due to its composition-dependent Curie temperature (30 – 400 K). The BST films can be transformed from ferroelectric to a paraelectric phase by controlling the Ba/Sr ($\frac{1-x}{x}$) ratio. The bandgap of BST material is controlled by percentages of BTO and STO in any given sample [69]. For BST, Ti ions are displaced towards the oxygen ions at the apices of the octahedron, increasing the Ti - O bond length. This indicates that the displacement of the Ti ion from its equilibrium position plays a vital role in determining the tuning properties of BST thin films. Thus, it can perform as a highly transparent insulating layer that has been used in the electroluminescent device [70]. The EO characterizations of BST films reveal an EO coefficient with a very large saturation value of the field-induced birefringence at the wavelength of 632.8 nm [71]. The optical second-harmonic generation (SHG) has also been observed in the NIR wavelength of 1.06 μm using a Q-switched Nd:YAG laser and at 760 nm using mode-locked Ti: Sapphire laser [72]. The nonlinear optical absorption and refraction coefficient of the polycrystalline $Ba_{0.7}Sr_{0.3}TiO_3$ film on quartz substrate have been reported as 1.2×10^{-6} m/W and 6.52×10^{-14} m^2/W, respectively [73]. Liu et al. reported NLO properties of $Ba_{0.6}Sr_{0.4}TiO_3$ film on (001) MgO substrate near 800 nm, and the n_2 values were ~ 10^{-14} cm^2/W [74]. Wang et al. reported NLO studies in $Ba_{0.5}Sr_{0.5}TiO_3$ film grown with PLD technique at 800 °C using 55 ps pulses at an excitation wavelength of 532 nm. They observed a large saturable absorption type

of nonlinearity with the magnitude of $\chi^{(3)}$ ~10^{-7} esu [75]. Venugopal et al. reported the large three photon absorption coefficient of $Ba_{0.5}Sr_{0.5}TiO_3$ thin films using Z-scan technique[76]. Due to this large NLO coefficients, BST thin films are used as optical switcher, optical limiter, Q switcher, mode locker, harmonic generator, etc.

1.2 Applications

Based on their structure and interesting properties mentioned above for BTO, STO, and BST, all the three kinds of thin films have been observed to be applicable in dynamic random access memories (DRAM) [77], non-volatile memories [78], electro-optic switches [50], pyroelectric detectors [79], optical waveguide modulators [80], thin-film capacitors [81], tunable microwave devices [82], piezoelectric devices [62], sensors [83], actuators [84], transducers[85], varistors [86], gas sensors [83], solid oxide electronic devices [87], solar cell electrodes [88], thermal energy conversion devices [89], wireless communications [49], surface acoustic wave (SAW) devices [90], photonics band gap [91], optical switch [92], optical limiters [67], delay line [93], etc.

1.3 Thin film deposition technique

To fulfill the advanced integrated electronic photonics circuit requirements such as photonic and optoelectronics devices, perovskite thin films in nanoscale and appropriate crystallinity and surface morphology are required. A variety of deposition techniques have been used to fabricate BTO, STO, and BST perovskite thin films. The various techniques of depositing thin film are summarized in Table 1-1.These involve magnetron sputtering [94], sol-gel [95], ion implantation [94], molecular beam epitaxy [96], and pulsed laser deposition (PLD) techniques [7, 97]. In the present thesis, the PLD technique is adopted for the fabrication of thin films of BTO, STO, and BST and infusion of thin Cu layer in them. PLD was proposed

for the very first time by Smith and Turner in 1965, immediately after the advent of high power lasers [98]. Later on, it has emerged as a powerful deposition tool for fabricating various materials, multilayer, and nanostructures since 1980s. A brief description of the PLD technique and its advantages are discussed in the following section. The setup of this technique employed in the present thesis work is detailed in Section 2.3, Chapter 2.

Table 1-1 *Different deposition techniques for preparation of perovskite thin films.*

Sr. No	Thin Film	Growth technique	Reference
1	BTO	Metal-organic chemical vapour deposition (MOCVD)	[99]
		Chemical solution deposition	[100, 101]
		Sol-gel	[102-104]
		Rf magnetron sputtering	[105, 106]
		PLD	[107, 108]
2	STO	MOCVD	[109]
		Chemical solution deposition	[110]
		Sol-gel	[111]
		Rf magnetron sputtering	[112]
		PLD	[113]
3	BST	MOCVD	[114]
		Chemical solution deposition	[115]
		Sol-gel	[116-118]
		Rf magnetron sputtering	[119]
		PLD	[82, 120]

1.3.1 Pulsed laser deposition technique

Pulsed laser deposition (PLD) , a relatively new technique, has gained wide acceptance recently for the deposition of high-quality thin films and simultaneous infusion of metallic nanoparticles in a single step [121, 122]. Properties of thin films via PLD are dependent on substrate and its temperature, background gas pressure, properties of gas used during deposition, and the laser parameters (wavelength, laser fluence, etc.) [123]. In the PLD technique, the texture of the nanostructures can be controlled by changing deposition parameters.

This technique offers various advantages as compared to those of other deposition techniques in terms of (a) stoichiometric transfer of material of any composition from target to the substrate, (b) relatively high deposition rates at moderate laser fluences, (c) precise control over film thickness [124], (d) fabrication of crystalline thin films even at room temperature and (e) applicable to any material including those having a very high melting point.

In the PLD technique, a high-power laser beam (laser intensity ~ 10^9 – 10^{11} W/cm^2) is focused onto the target inside a high vacuum chamber (pressure is 10^{-6} mbar or in the presence of suitable low-pressure gas). This results in the formation of laser-induced plasma (LIP) of the target material. The LIP plume comprises of highly energetic electrons, ions, and atoms/molecules of the target material. This plume expands adiabatically and cools down while moving towards the substrate placed a few cm apart from the target and deposited on it. The thin film grows on the substrate when the condensation rate is higher than the rate of particles supplied by ablation, and the thermal equilibrium condition is satisfied. When the target is placed in a gaseous ambient, the surrounding gas molecules also undergo ionization, dissociation, and plasma formation via multiphoton absorption of laser energy. If the gaseous

medium is reactive, e.g., oxygen, then the oxygen-rich film can be deposited. In this case, both target plasma and background gas plasma undergo adiabatic cooling to form the molecular species. In the PLD chamber, the substrate holder is fitted with a substrate heater to raise the substrate temperature during the film growth process as per requirement. The substrate temperature is an essential parameter for modifying the crystallographic structure, density, and morphology of thin films. The PLD chamber can be pressurized by various types of background gases using appropriate gas inlet ports based on the requirements. The role of the background gas is also to thermalize the highly energetic plasma species and compensate for the loss of an essential component from the plasma plume of the target. The background gas also helps in the formation of stoichiometric films.

1.4 Characterization tools for thin films

The physical properties of thin films are studied by various characterization tools. The structural characterization of the thin films is performed by X-Ray Diffraction (XRD) technique and micro Raman spectroscopy to unveil crystalline nature, strain, and bonding. Field-effect scanning electron microscopy (FESEM) images are captured to investigate the surface morphology of thin films. The atomic composition of the thin films can be determined using the electron diffraction X-Ray spectroscopic (EDX) technique attached with the FESEM instrument. Further, the thickness of films is measured by Stylus Profilometer and cross-sectional FESEM images. Atomic force microscopy (AFM) images of the thin films are captured to study the surface morphology. The transparent and semitransparent thin films are subjected to UV-Visible-NIR spectroscopy to study the linear absorption coefficient, film thickness, and bandgap energy. The surface plasmon resonance (SPR) of the plasmonic films

can be detected by UV Visible-NIR spectrometer. Photoluminescence (PL) measurement is performed to understand the defects levels present in the thin films.

1.4.1 Nonlinear optical properties of thin films

The NLO properties of materials have been utilized for optical switching, optical waveguide, optical limiting, harmonic generation, information storage, etc. Self-focusing observed due to positive nonlinear refraction phenomena may be helpful in reducing the optical beam-spot size below the diffraction limit and hence can be applied for optical data storage. The NLO coefficients can be particle size-dependent; below or close to its excitonic Bohr radius. A variety of techniques have been developed to measure the NLO properties of materials. These techniques include nonlinear interferometry [125], degenerate four-wave mixing [126], ellipse rotation [127], beam distortion measurements [128] and *Z*-scan technique [129]. The first three techniques are sensitive but require a relatively complex experimental setup for NLO analysis. In contrast, the beam distortion measurement is relatively sensitive, simple but needs detailed wave propagation analysis. The *Z*-scan technique, proposed by Sheik-Bahae et al. in 1989, is based on the spatial narrowing and broadening of the far-field pattern of a focused Gaussian beam [129]. This technique is relatively simple and sensitive technique to measure the values of β and n_2 of bulk, thin-film as well as liquid samples [130-132]. In this technique, the translation of the sample across the focal plane leads to the change of irradiance at the sample, resulting in changes in the intensity-dependent optical properties. The intensity transmitted through the sample is recorded as a function of sample location *z* with respect to the focal plane. The major advantage of this technique is its ability to obtain both the NLO coefficients and to determine the signs of the two components. The technique includes an open aperture (OA) and closed aperture (CA) *Z*-

scan measurements, which determine nonlinear absorption (NLA) coefficient, β, and nonlinear refractive index (NLR) coefficients, n_2. In the present thesis, the modified *Z*-scan set-up is employed to measure NLO properties of the thin films[133], and details of the experimental setup are described in Section 2.4.8, Chapter 2.

NLO materials under continuous-wave (cw) laser illumination have many applications in image processing, optical limiters, optical switching, etc.[134]. With the advent of lasers operating over wide ranges of wavelength and power, the necessity for protecting sensors, optical components, and human eyes from laser-inflicted damage has increased enormously. In this context, optical limiters which display decreasing transmittance as a function of laser irradiance are of great importance. Optical limiting (OL) materials with low thresholds can be used for the protection of eyes and sensitive optical devices from laser-induced damage. OL can be achieved by employing various nonlinear optical mechanisms, including self-focusing, self-defocusing, induced scattering, induced refraction, induced aberration, excited state absorption (ESA), two photon absorption (TPA), photo-refraction, and free carrier absorption (FCA) in nonlinear optical media [135]. BTO thin films are also explored with a great interest for potential optical limiters, optical switches, and waveguides [136-138].

1.5 Motivations and objectives

Owing to the numerous of applications and utility in the various fields, there is a need to study the perovskite materials, particularly BTO, STO, and BST, in the thin-film geometry. Therefore, this is a dire need to optimize the deposition parameters, the types of dopants and their composition. The substrate temperature, thickness, and background gas pressure play a pivotal role in determining the morphology, stoichiometry, crystallinity, and strain, structural and optical properties of thin films. Therefore, an in-depth understanding is required to

optimize the deposition parameters to obtain the desired thin film with specific structural and optical properties in any type of deposition technique. Moreover, BTO, STO, and BST films and their infusion with the metal nano-layer thin film via PLD are not much explored. NLO properties of these kinds of films are also not very well studied particularly with a cw laser. Therefore, the present thesis is focused on the fabrication of perovskite thin films of BTO, STO, and BST and infusion with Cu nano-layer via the PLD technique. Further, the thesis is aimed to investigate the dependence of linear, NLO properties and PL spectrum on the deposition parameters, viz; background gas oxygen pressure and the substrate temperature as well as the type of substrate.

1.6 Objective and organization of the present thesis

The present dissertation is aimed towards systematic studies on linear and NLO properties of PLD deposited perovskite thin films so as to obtain the optimum parameters. The effect of Cu nano-layer on NLO properties of BTO, STO, and BST thin films deposited at optimum parameters is undertaken. For structural, morphology, and optical studies, PLD thin films are deposited on to quartz, Si (100), and MgO substrates. The room temperature PL properties of some of these thin films are studied. The possible origins of PL of the thin films are also investigated. The modified *Z*-scan technique measured the NLA and NLR coefficients. The effect of substrate temperature, oxygen pressure, thickness, and substrate on the third-order NLO properties under cw laser illumination has been investigated. The major objective of the NLO studies of BTO, STO, BST, and infusion of Cu nano-layer thin films is to understand how film stoichiometry, crystallinity, and strain affect their NLA, NLR coefficients, and OL property in these films.

The present thesis work is divided into eight chapters as listed below:

Chapter 1: "*Introduction*" – presents relevant literature on the core topics of the thesis. Thin film deposition techniques and characterization tools for analysing structural, compositional, and the linear as well as nonlinear optical properties of the perovskite thin films are briefly studied. Finally, the thesis organization is briefed.

Chapter 2: "*Experimental details*" – describes the PLD setup used for the fabrication of BTO, STO, and BST thin films. The various commercially available instruments used in the present thesis work for the characterization of PLD films are documented in this chapter. An in-house assembled modified *Z* scan technique to measure the nonlinear absorption and nonlinear refraction coefficients is discussed.

Chapter 3: "*Influence of substrate temperature, and oxygen pressure on the linear and nonlinear optical properties of $BaTiO_3$ thin films grown by PLD*" – includes the effect of substrate temperature, oxygen pressure, thickness on the morphological, structural, linear, and nonlinear optical properties of BTO thin films and from these analysis, the optimum conditions for PLD growth of BTO film are assessed.

Chapter 4: "*Influence of Cu nano-layer on linear, nonlinear and photoluminescence properties of $BaTiO_3$ thin films fabricated via PLD*" is on the influence of Cu thin layer on the SPR and NLO properties of BTO thin films.

Chapter 5: "*Influence of Cu nano-layer on the linear, and nonlinear properties of PLD $SrTiO_3$ thin films*" – includes the effect of Cu thin layer on STO host matrix on morphology, structural, linear, nonlinear optical properties and SPR property.

Chapter 6: "*Compositional dependence on structural, linear, and nonlinear optical properties of PLD deposited $Ba_{1-x}Sr_xTiO_3$ ($0 \leq x \leq 1$) thin films*" – discusses the $Ba_{1-x}Sr_xTiO_3$ ($0 \leq x \leq 1$) thin films fabricated by the PLD technique at optimum deposition parameters obtained in Chapter 3. The effect of Sr concentration on the structural, surface morphology, linear optical properties (transmission, absorption, bandgap energy, refractive index), and NLO properties (modified *Z*-scan) are discussed vividly. The influence of Cu nano-layer on optimized BST composition is also presented at the optimized deposition conditions.

Chapter 7: "*Influence of Cu nano-layer on optical limiting in BTO, STO, and BST PLD thin films*" – discusses the optical limiting response of BTO, STO and BST-0.5 thin films fabricated via PLD on quartz and MgO substrates for 180 minutes duration. The effect of Cu nano-layer embedded on these three thin films deposited on quartz substrate for 60 minutes onto the OL response is also detailed.

Chapter 8: "*Conclusions and Future scope*" – sums up the salient features of the present research work with the possible applications in the future.

Chapter 2 : Experimental details

The present chapter describes the synthesis of $BaTiO_3$ (BTO), $SrTiO_3$ (STO) and $Ba_{1-x}Sr_xTiO_3$ ($0 \leq x \leq 1$) (BST) & Cu-BTO/STO/$Ba_{0.5}Sr_{0.5}TiO_3$ thin films via the pulsed laser deposition (PLD) technique on Si, quartz and MgO. Initially BTO films were deposited by varying the substrate temperature and background oxygen pressure to obtain the optimized value of these important deposition parameters. Remaining samples of BTO, STO and BST reported in this thesis were deposited at these optimized conditions only. Few two samples were also prepared to study the influence of nanostructured Cu thin film on BTO and STO. The structural characterization of all the samples were carried out via X-ray diffraction (XRD) and Raman spectrometer. The surface morphology was unveiled by field emission scanning electron microscope (FESEM) and atomic force microscopy (AFM). The linear optical properties were analyzed by UV-Visible NIR spectrometer. The NLA and NLR coefficients were measured via in-house assembled modified *Z*-scan set up. The same set- up was also employed to study the optical limiting (OL) properties of BTO, STO and $Ba_{0.5}Sr_{0.5}TiO_3$ PLD thin films. Photoluminescence (PL) measurement was performed for studying the influence of Cu on BTO films.

2.1 Target preparation

To fabricate BTO, STO and different compositions of BST thin films via PLD, the respective targets were prepared by solid-state synthesis method. The steps involved in preparing the BTO target were discussed below.

For preparing pure BTO and STO targets, the respective powders of high purity were procured from Alfa Aesar, 99% purity.

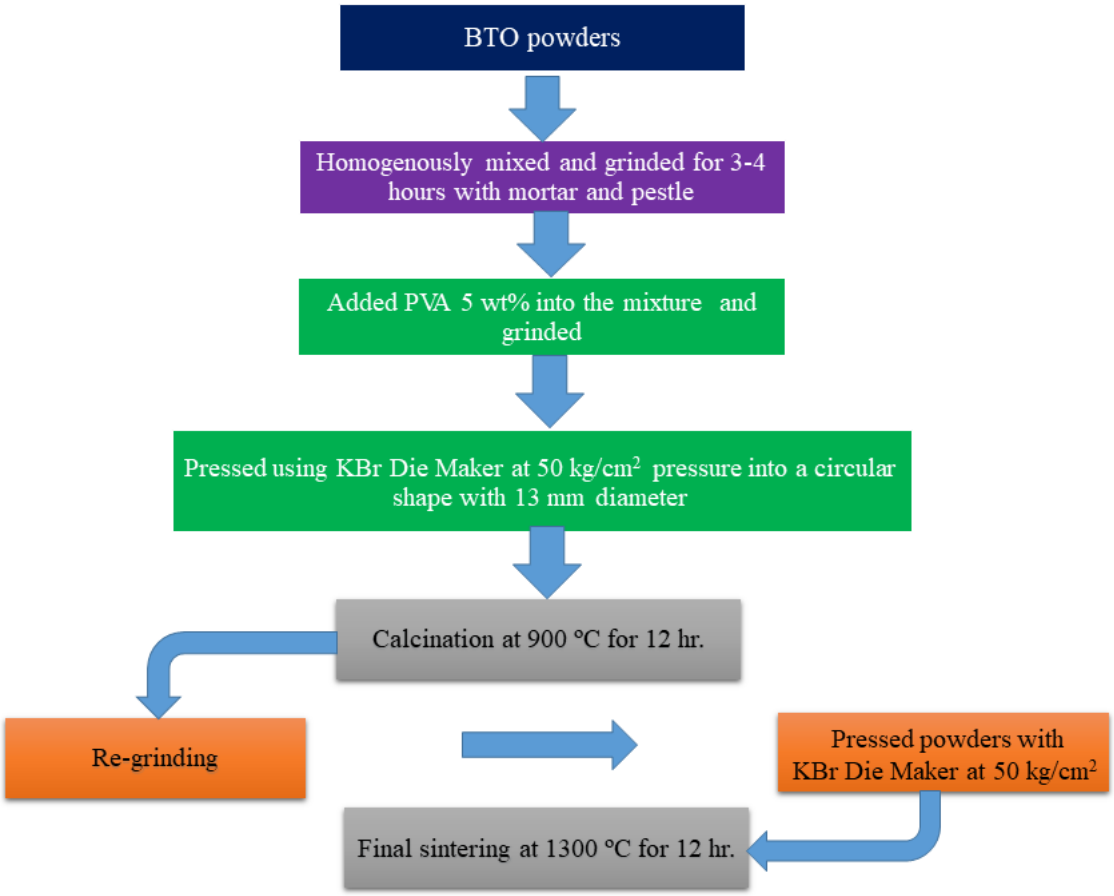

Figure 2-1 *Flowchart of the steps involved in solid state synthesis method for making BTO targets.*

The flowchart of various steps involved in the preparation of BTO targets is shown in Figure 2-1. This process was common for STO as well as BST targets. But, in case of BST, the appropriate amount of both the powders as listed in Table 2-1, were mixed before making the targets.

For each and every pellet, respective powder (or powders) were mixed well with propanol and stirred well by using of spatula and grinded into fine powder using mortar and pestle. An organic binder, polyvinyl alcohol (PVA) of 5 wt. % was added into this powder and grinded again for 4 to 5 hrs. For the preparation of 5% PVA solution, 5 gm of PVA powder

was mixed in 100 mL of distilled water and thoroughly mixed using magnetic stirrer in order to obtain a homogeneous solution.

Table 2-1 *Amount of BTO and STO powder for* $Ba_{1-x}Sr_xTiO_3$ *(*$0 \leq x \leq 1$*) (BST) for target preparation.*

Sample	$Ba_{1-x}Sr_xTiO_3$ ($0 \leq x \leq 1$) BST targets composition	Wt. of BTO (gm.)	Wt. of STO (gm.)
BTO	x = 0	5.0000	0.0000
BST-0.3	x = 0.3	3.7390	1.2609
BST-0.4	x = 0.4	3.2796	1.7204
BST-0.5	x = 0.5	2.7982	2.2018
BST-0.7	x = 0.7	1.7630	3.2370
STO	x = 1	0.0000	5.0000

By using a KBr Die Maker (model *Techno search instrument M-20, India*) at 50 kg/cm^2 pressure, the finally grinded powder was converted into a dense pellet in the form of a circular disc having ~ 13 mm diameter and ~ 5 mm thickness. All the pellets were calcinated at 900 ºC for 12 hrs to evaporate the binder separately in a furnace. For proper sintering process, each and every calcinated pellet was again crushed and grinded for 4 to 5 hrs to reduce air spacing in between particles. These pellets were finally sintered to reduce porosity at 1300 ºC for 12 hrs in the furnace (make *LHT 04/18, Naberthem GmbH, Germany*; Temperature range: 25 ºC to 1800 ºC) with systematic slow heating followed by a slow cooling process to obtain a dense crack free pellet as shown in Figure 2-2. In this way, finally a dense hard targets having low porosity were obtained.

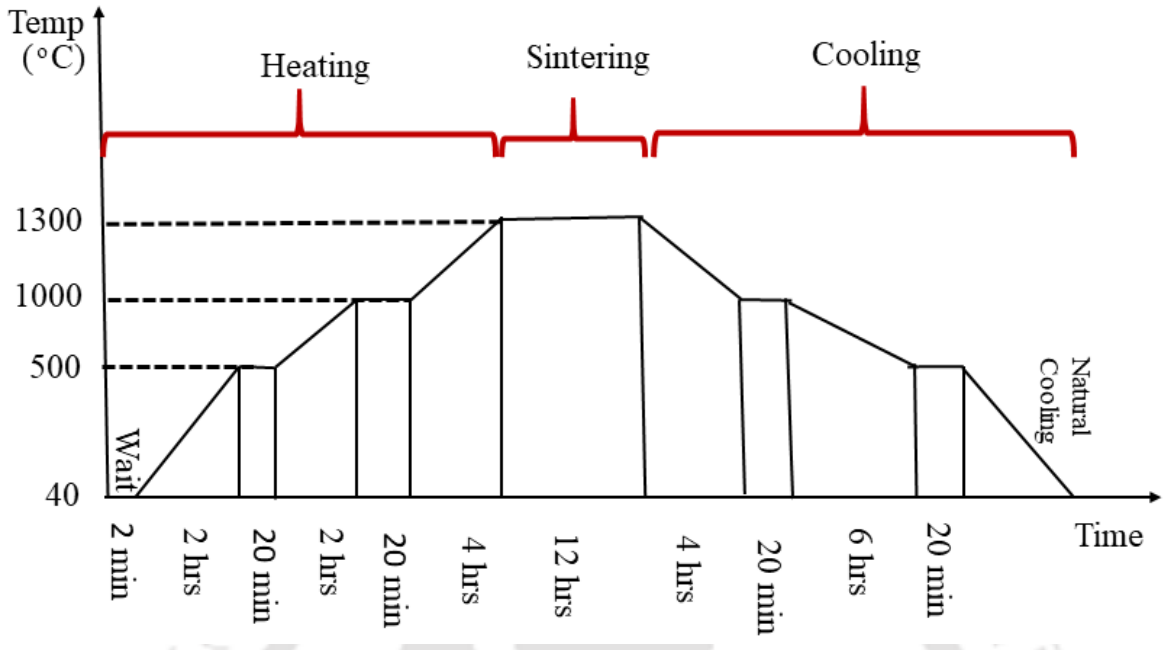

Figure 2-2 *Heating and cooling process during sintering process.*

Figure 2-3 (a), (b) and (c) shows the images of unsintered, sintered BTO and BST (finally sintered) targets, respectively.

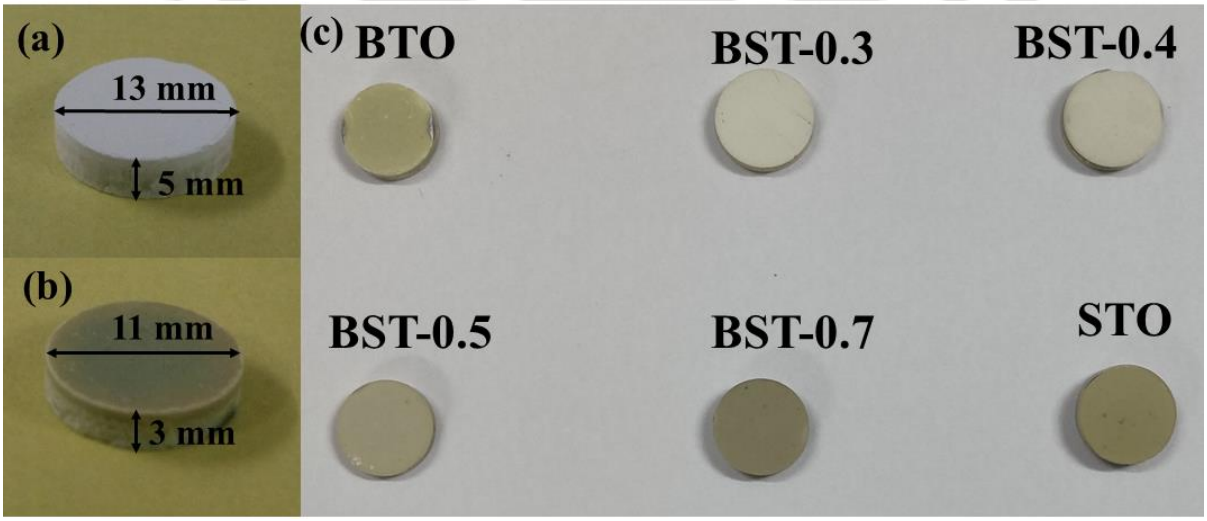

Figure 2-3 *Photograph of (a) unsintered (b) sintered BTO target, and (c) sintered BST targets.*

2.2 Substrate preparation

PLD thin films were deposited on polished silicon (n - type) (1cm × 1cm), quartz (1cm × 1cm) and MgO (1cm × 1cm) substrates. Before deposition, each and every substrate was cleaned ultrasonically for 25 - 30 minutes in acetone and dried, and then mounted on the substrate holder stage of the PLD deposition chamber.

2.3 PLD set up for fabrication of BTO, STO, BST and Cu thin films

Figure 2-4 and Figure 2-5 show the schematic and photograph of the PLD setup used for deposition of all the thin films reported in this thesis, respectively.

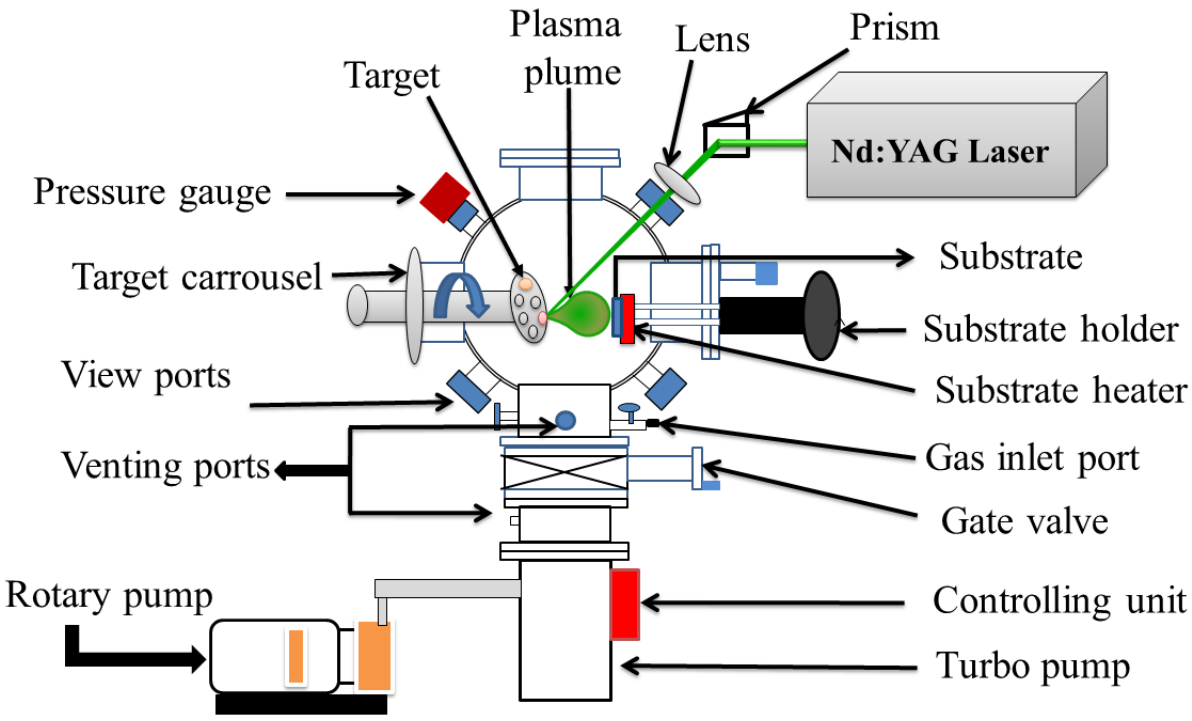

Figure 2-4 *Schematic of PLD setup.*

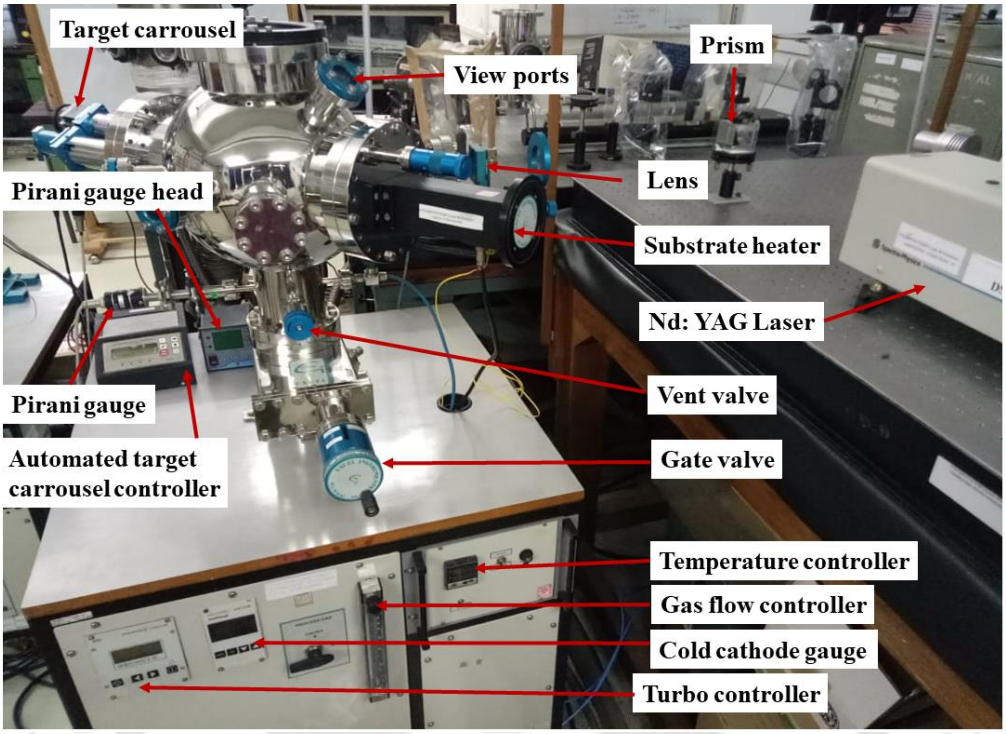

Figure 2-5 *Photograph of PLD setup.*

The PLD chamber is made up of stainless steel (SS) spherical vessel of 12″ chamber equipped with multiple viewports, target holder carrousel stage having microprocessor-controlled rastering facility, substrate holder along with provision for the programmable heater to elevate the substrate temperature, pressure gauges, gas inlet port and a turbo molecular pump (*Pfeiffer, Hi Pace 300 C*) backed by a rotary pump (*Pfeiffer, DUO 10MC*). The turbo pump is connected to the bottom 100 CF port via a 100 CF gate value of the PLD chamber. The gas line from the oxygen cylinder is connected to the chamber via a gas flow controller to one of the 16 CF port of the chamber. The pressure inside the chamber is monitored by a compact cold cathode gauge (*Pfeiffer, IKR 251*) and Pirani gauges (*Pfeiffer, PCR 280 and Hind HiVac, HPS-2*) working in the low-pressure regime (10^{-2}-10^{-7} mbar) and high-pressure regime (10^{3}-10^{-3} mbar), respectively. The PLD target (sintered pellets) is mounted onto a motorized target carrousel which is installed inside the PLD chamber through one of the 150 CF port. The

substrate (quartz / Si / MgO) is mounted on the substrate holder stage inserted via another 150 CF port opposite to the target carrousel port. The substrate holder is equipped with a resistive heating to maintain the desired temperature during deposition. Before deposition, the chamber is evacuated in the range of 10^{-5} to 10^{-6} mbar base pressure using turbo molecular pump backed by rotary pump and then pressurized with background oxygen gas at required pressure for the deposition of BTO, STO and BST thin films. The deposition of nano-layer Cu thin films was performed under high vacuum (~ 10^{-6} mbar).

All the thin films of BTO, STO, BST & Cu sanwiched in between BTO/STO/ BST-0.5 and substrate were deposited at a fixed laser fluence of 10J/cm^2 from a high power, 2nd harmonic (λ =532 nm), of a Q-switched Nd: YAG laser (make: *Spectra-Physics*, model *Quanta–Ray INDI*) of pulse width ~ 10 ns and repetition rate of 10 Hz. The laser was focused using a 35 cm convex lens onto the target resulting in the ablation and plasma formation. It was deposited on the substrate placed parallel to and 4 cm away from the target. The required targets were mounted on the µ processer programmble target holder carrousel stage. During the deposition, the target holder was continuously rotated and rastered so as to avoid repeated impingment of laser shots on the same point. For optimizing the substrate temperature (T_s) and oxygen pressure (O_2), the two sets of films for BTO, as listed in Table 2-2 were deposited, the first one by varying only the substrate temperature while maintaining background oxygen pressure fixed at 0.1 mbar in order to obtain the optimised deposition temperature. The second set of films was prepared by varying the oxygen pressure while keeping the optimum substrate temperature fixed at 700ºC. For both the sets, in order to obtain the optimized deposition temperature and pressure, each and every film was deposited for 60 minutes duration.

Table 2-2 *Deposition parameters of BTO thin films.*

Set	Substrate temperature(°C)	Oxygen pressure (mbar)	Substrate	Deposition time (min.)
Set 1	400	0.1	Quartz, n-type Si (100)	60
	500			
	600			
	650			
	700			
Set 2	700	0.005		
		0.05		
		0.1		
		0.5		
		1		

To study the effect of metal infusion on the NLO and PL properties, three different configurations viz; pure BTO (BTO1), Cu-BTO (BTO2) and BTO-Cu (BTO3) thin films were grown onto quartz and n-type Si (100) substrates via PLD technique under the optimum deposition parameters as shown in Figure 2-6 and listed in Table 2-3. For the infusion of the metal nanolayer of Cu, a pure copper metal sheet (1 cm × 1cm) (Alfa Aesar, 99% purity) was used as the PLD target.

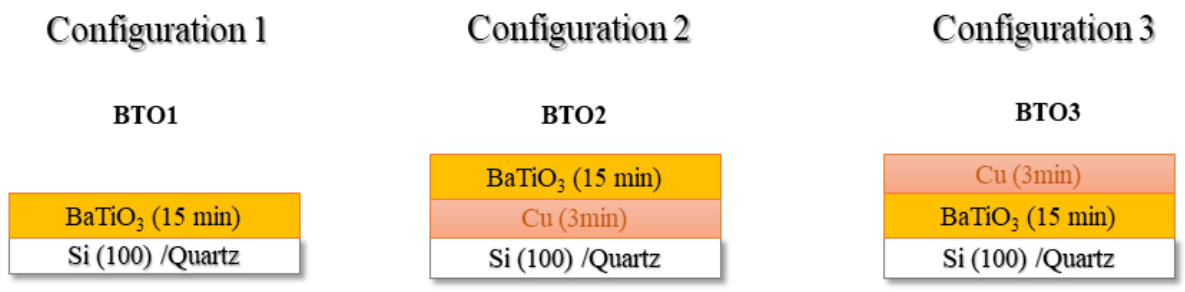

Figure 2-6 *Cu infused BTO thin film configurations.*

The first configuration, BTO1, BTO was directly deposited on the substrate for 15 minutes. In the second configuration, BTO2, initially Cu film was deposited via PLD at a temperature of 700 ºC under vacuum (~ 10^{-6} mbar) for 3 minutes duration followed by deposition of BTO film over it for 15 minutes duration under optimised O_2 pressure of 0.1 mbar at 700 ºC. In the third configuration, BTO3, BTO was first deposited directly on the substrate at optimised parameters and top of it Cu layer was deposited under vacuum for 3 minutes.

Table 2-3 *Deposition parameters for BTO and nanostructured Cu thin layer infused BTO thin films.*

Thin film		**Pressure (mbar)**	**Deposition time (min.)**	**Substrate**	**Substrate temperature (°C)**
BTO1		O_2 (0.1)	15	Quartz, n-type Si (100)	700
BTO2 (Cu-BTO)	Cu	Vacuum (~ 10^{-6})	3		
	BTO	O_2 (0.1)	15		
BTO3 (BTO-Cu)	BTO	O_2 (0.1)	15		
	Cu	Vacuum (~ 10^{-6})	3		
BTO		O_2 (0.1)	60		
BTO2_1 (Cu-BTO)	Cu	Vacuum (~ 10^{-6})	3		
	BTO	O_2 (0.1)	60		

The best NLO and SPR properties were obtained for the second configuration (BTO2). Therefore, another thin film , BTO2_1, was prepared in similar manner just by changing the deposition time for BTO from 15 to 60 minutes while Cu layer was sanwiched in between substrate and BTO in this manner smilar to BTO2 configuration, Table 2-3.

To study the effect of infusion of Cu nanolayer on STO films (another important photorefractive system), the film deposition was repeated by replacing BTO with STO target and these are labelled as STO, STO2_1, and STO3_1 as listed in Table 2-4.

Table 2-4 *Deposition parameters for STO and nano-structured Cu infused thin films of STO.*

Thin film		**Pressure (mbar)**	**Deposition time (min.)**	**Substrate**	**Substrate temperature (°C)**
STO		O_2 (0.1)	60	Quartz	700
STO2_1 (Cu-STO)	Cu	Vacuum (~ 10^{-6})	3		
	STO	O_2 (0.1)	60		
STO3_1 (STO-Cu)	STO	O_2 (0.1)	60		
	Cu	Vacuum (~ 10^{-6})	3		

Table 2-5 *Deposition parameters of BST thin films.*

Thin Film	**Substrate**	**Substrate Temperature (ºC)**	**Oxygen pressure (mbar)**	**Thickness (nm)**
BTO	Si, Quartz	700	0.1	360 ± 10
BST-0.3				
BST-0.4				
BST-0.5				
BST-0.7				
STO				

In order to study the effect of percentage composition of BTO and STO in the composite thin film of BST, thin films were prepared via PLD at the same optimized deposition

parameters as that of BTO and the deposition time was maintained in such a way so as to obtain nearly the same thickness for all the films as listed in Table 2-5. Further, to investigate the effect of Cu nano-layer on BST dielectric matrix, at optimum BST composition, Cu nano-layer was embedded directly on the substrate and then BST thin film was deposited on top of it for 60 min. duration, Table 2-6. All these deposition parameters for depositing these thin films are listed in Table 2-6.

Table 2-6 *Deposition parameters of nanocomposites of BST-0.5 thin film.*

<table>
<tr><th colspan="2">Thin film</th><th>Pressure (mbar)</th><th>Deposition time (min.)</th><th>Substrate</th><th>Substrate temperature (°C)</th></tr>
<tr><td colspan="2">BST-0.5_1</td><td>O_2 (0.1)</td><td>60</td><td rowspan="3">Quartz</td><td rowspan="3">700</td></tr>
<tr><td rowspan="2">BST-0.5_2 (Cu-BST-0.5)</td><td>Cu</td><td>Vacuum (~ 10^{-6})</td><td>3</td></tr>
<tr><td>BST -0.5</td><td>O_2 (0.1)</td><td>60</td></tr>
</table>

To study the effect of thickness and substrate, BTO, STO and BST-0.5 thin films were deposited on quartz and MgO substrate for 180 min. duration at same optimised temperature 700ºC and oxygen pressure 0.1 mbar as listed in Table 2-7. BTO, STO, and BST-0.5 thin films deposited on quartz substrate were abbreviated as BTO_Q, STO_Q, and BST-0.5_Q, respectively. On the other hand, BTO, STO, and BST-0.5 thin films deposited on MgO substrate were labelled as BTO_M, STO_M, and BST-0.5_M, respectively.

Table 2-7 *Deposition parameters for BTO, STO, and BST-0.5 thin films on different substrates.*

Thin Film	Substrate	Substrate Temperature (ºC)	Oxygen Pressure (mbar)	Deposition time (min.)
BTO_Q	Quartz	700	0.1	180
BTO_M	MgO			
STO_Q	Quartz			
STO_M	MgO			
BST-0.5_Q	Quartz			
BST-0.5_M	MgO			

2.4 Characterization of PLD thin films of BTO, STO, BST, Cu layer infused BTO, STO and BST

All the thin films fabricated via PLD as detailed in Section 2.3 in the present thesis work were subjected to several characterizations as briefed below:

2.4.1 Stylus Profilometer

The overall thickness of each and every deposited thin film was measured using Stylus Profilometer (model *Veeco DekTak 150*). In the PLD chamber, the substrate was placed intact on the substrate holder with the help of the two clips during deposition. These clips acted as natural masks and provided the substrate-film step for the measurement of thickness. The profilometer was scanned at five different locations by a diamond-tipped stylus across this step. The final thickness of the films from this measurement were obtained after taking the average over all the scanned locations for each and every film.

2.4.2 X-Ray diffraction (XRD)

XRD technique is a non-contact and non-destructive measurement tool to study the crystalline phases present in the sample (bulk or thin film) and to measure the crystallite size,

unit cell dimensions, strain, stress, defect structures, etc. [139]. In the present thesis work, the XRD spectra of the thin films were recorded by an X-Ray diffractometer (model *Rigaku, TTRAX III 18 kW*) operating at 1.5406 Å of Cu-$K_{\alpha 1}$ line within 2θ range of 20-70 º in a step size, $\Delta\theta$ = 0.02 º and a scan rate of 3 º per min. The analysis of XRD spectra was performed by Rietveld refinement method using Fullproof suite software [140].

2.4.3 Raman spectroscopy

Raman Spectroscopy is a very sensitive tool to identify the crystal structure, bonding, and chemical composition of the material and does not require any sample preparation [141]. Micro-Raman measurements were performed using a high-resolution Raman spectrometer (model *Horiba, LabRam HR 800*) with an excitation wavelength of 488 nm. The excitation source was focused by a 100X objective lens and the laser power of 10 mW was maintained in order to avoid laser heating and damage to the films.

2.4.4 Field emission scanning electron microscope (FESEM)

All the films were subjected to FESEM (model *Zeiss Sigma 300*) to scan the surface morphology of the films. Cross-sectional FESEM images were captured to determine the thickness of some of the thin films particularly Cu infused film. A thin layer of gold coating was applied on all the samples before loading them inside the instrument.

2.4.5 Energy-dispersive X-ray Spectroscope (EDX)

The stoichiometry of PLD deposited thin films were investigated by energy dispersive X-ray spectroscopy (EDX) (model *M/s Sigma Zeiss, Germany*). In this instrument, a thin gold layer was also required on top of the thin film before loading them inside the vacuum chamber to avoid the charging effect during the measurement and here, EHT of 5 KV was also used.

2.4.6 Atomic force microscopy (AFM)

AFM is another powerful imaging technique used to measure the surface morphology and roughness of the films. The AFM model *Oxford Cypher* was used in non-contact mode using a silicon cantilever to image the surface morphology of the film. The root means square (RMS) surface roughness was determined via open-source Gwyddion software [142].

2.4.7 Assessment of linear optical parameters via UV-Visible-NIR spectrometer

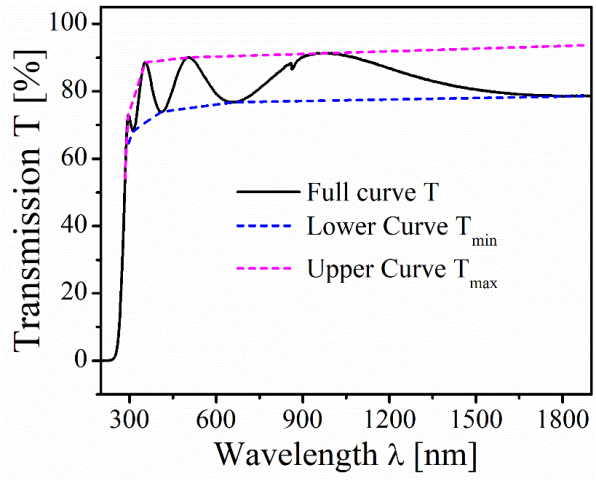

Figure 2-7 *Transmission spectrum of a thin film.*

The linear absorption coefficient, transmittance, and bandgap energy were determined using a UV- Visible NIR Spectrometer (model *Perkin Elmer, Lambda 950*). The UV-Visible NIR transmission spectrum of one of the film deposited on a quartz substrate is shown in Figure 2-7 as an example. It clearly exhibits few maxima and minima corresponding to the interference fringes. The Swanpoel envelope technique is applied for the estimation of the linear refractive index (n) and thickness (L) of these films [143]. The refractive indices for all the films as a function of wavelength (λ) were calculated using the expression given by;

$$n = [N + (N^2 - n_s^2)^{1/2}]^{1/2} \tag{2.1}$$

where

$$N = 2n_s\left(\frac{T_{max} - T_{min}}{[T_{max}T_{min}]}\right) + \frac{n_s^2 + 1}{2} \tag{2.2}$$

where T_{max} and T_{min} are the consecutive transmission maxima and minima of transmission spectra, respectively. The refractive index of the quartz substrate is denoted as n_s (n_s = 1.45). The calculated values of n as a function of λ are fitted to the Cauchy dispersion relation, given by;

$$n = A_0 + \frac{B_0}{\lambda^2} \tag{2.3}$$

In equation (2.3), the static refractive index is denoted as A_0 and the slope of the plot of n vs $1/\lambda^2$ is denoted as B_0. The thickness of these films was calculated using the following expression;

$$L = \frac{\lambda_a \lambda_b}{2[\lambda_b n_a - \lambda_a n_b]} \tag{2.4}$$

where n_a and n_b are refractive indices corresponding to the wavelengths λ_a and λ_b of adjacent maxima or minima, respectively.

The linear absorption coefficient was estimated from the Beer- Lambert's Law [144],

$$I = I_0 \exp(-\alpha L) \tag{2.5}$$

In equation (2.5), I_0 is the incident light intensity, I is the intensity of the light transmitted through the sample and α is the corresponding linear absorption coefficient, which is related to the transmittance of the thin films from equation (2.5) as;

$$\alpha = \frac{-\ln T}{L} \tag{2.6}$$

where T , $(=\frac{I}{I_0})$, is the transmittance of the thin film. From Figure 2-7, T is recorded as a function of λ and hence α can be obtained as a function of wavelength. The absorption coefficient , α , is related to the photon energy ($h\nu$) and the bandgap (E_g) by the following equation [145];

$$\alpha h\upsilon = A\left(h\upsilon - E_g\right)^m \tag{2.7}$$

where A is the Tauc slope and the exponent m is dependent upon type of electronic transition (m =1/2, 3/2 and 2 for the direct, forbidden and indirect transitions, respectively), determined by the nature of the material [146]. In the present thesis, E_g was calculated by assuming an indirect electronic transition (m = 2). The linear region of the Tauc plot, $(\alpha h\nu)^{1/2}$ versus $h\nu$ curve is fitted with a straight line and the intercept of this straight line measures the optical bandgap, E_g of the sample under consideration.

2.4.8 Nonlinear optical characterization via *Z*-scan

To study the NLO properties of the PLD this films, a modified *Z*-scan technique was adopted [133].

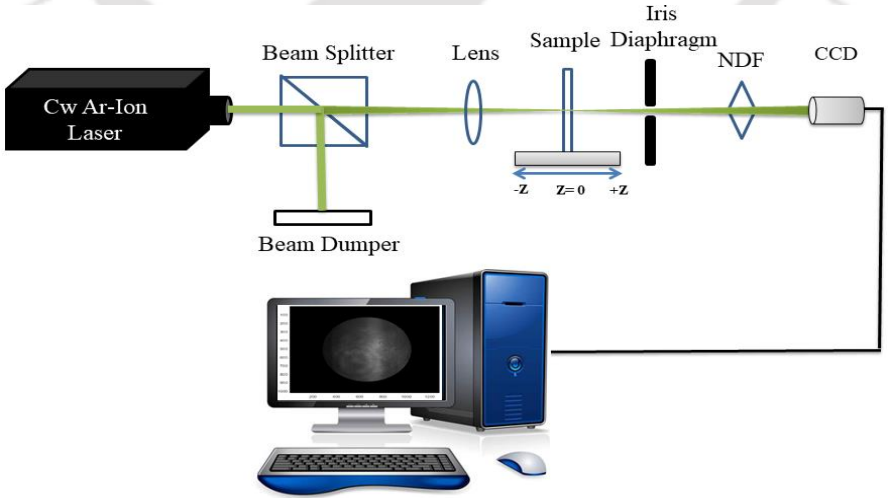

Figure 2-8 *Schematic of modified Z-scan technique.*

In a conventional *Z*-scan setup, a photodiode as a detector is used to record the data for open aperture (OA) and close aperture (CA) *Z*-scan separately [129]. In the modified *Z*-scan setup, the photodiode is replaced by CCD, and the OA, as well as CA data, are extracted by a single scan only [133]. The schematic of the modified *Z*-scan setup assembled in house is shown in Figure 2-8. In this setup, a continuous wave (cw) Ar ion laser (make: *Melles Griot, 35-LAP- 431-230,* model *400-A03*) of 95 mW operating at a wavelength (λ) of 488 nm was used. As the power of the laser was large enough to spoil the sample, therefore laser beam was divided into 60:40 ratios by a cube beam splitter (BS) placed before the lens as shown in Figure

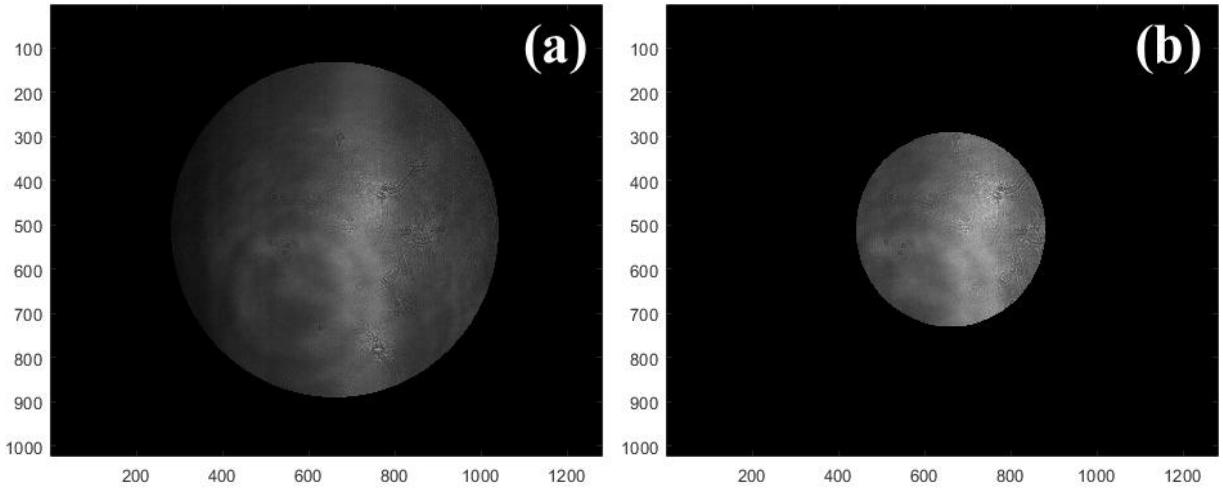

Figure 2-9 *CCD Images of (a) open and (b) close aperture Z-scan transmitted beam.*

2-8. The transmitted beam (40 %) was allowed to fall on the sample via a lens having a focal length (*f*) of 5 cm and the reflected beam from BS was just dumped. The sample was scanned 20 mm along the optics axis (the *z*-direction) around both sides of the focus of the lens (z_f). The transmitted beam through the sample was imaged on CCD (PCO Pixel fly) interfaced to the computer. One such recorded image through CCD is shown in Figure 2-9 (a).

The integrated intensity over the entire image as a function of sample position, *z*, w.r.t focus of the lens, z_f , gives the OA curve and is used for the measurement of nonlinear

absorption coefficient of the film [133]. The CA *Z*-scan data was extracted by placing a suitable synthetic aperture by a MATLAB program in the central region of the image of OA *Z*- scan. One such cropped image obtained from Figure 2-9 (a) is shown in Figure 2-9 (b). The integrated intensity of these partially masked images of CA as a function of *z* determined the nonlinear refractive index coefficient. A neutral density filter (4 OD) was placed in front of CCD for avoiding its saturation. An aperture of ~ 3 mm diameter was placed after the sample in order to prevent the scattered light from entering into CCD. The beam waist of the laser, $w_0 = \frac{f\lambda}{D}$ where *D* is laser beam diameter ~1 mm and Rayleigh length, ($z_0 = \frac{\pi w_0^2}{\lambda}$), were found to be 24.4 µm and 3.83 mm, respectively. The synthetic aperture size (S) was maintained in such a manner so that the linear aperture transmittance, the ratio of CA and OA signal (S = CA/OA) was ~ 0.4, which was the optimum value to exclude the contribution of the absorptive nonlinearity for the determination of refractive nonlinearity [133]. The nonlinear absorption coefficient (β) was obtained after fitting the experimental data for OA using equation (2.8).

$$T_{open} = 1 \pm \frac{\beta I_c L_{eff}}{2^{3/2}\left[1+\left(\frac{z}{z_0}\right)^2\right]} \tag{2.8}$$

In equation (2.8), T_{open} is the normalized transmittance for OA *Z*- scan and the positive and negative signs indicate the saturation absorption (SA; peak at center) and reverse saturation absorption (RSA; valley at center), respectively. I_c (= 0.34 kW/cm^2) is the peak irradiance at the center of the focal spot. L_{eff} is the effective film thickness and it is expressed by the equation (2.9),

$$L_{eff} = \frac{1-\exp(-\alpha L)}{\alpha} \tag{2.9}$$

The nonlinear refractive index coefficient (n_2) was extracted by fitting the normalized CA data to the equation (2.10) [129],

$$T_{close} = 1 \pm \frac{4 n_2 I_c L_{eff} \left(z / z_0 \right) k}{\left[9 + \left(\frac{z}{z_0} \right)^2 \right] \left[1 + \left(\frac{z}{z_0} \right)^2 \right]} \tag{2.10}$$

where T_{close} is normalized transmittance for CA *Z*- scan and k ($= \frac{2\pi}{\lambda}$) is the magnitude of the wave vector. Here, the positive and negative signs indicate self-focusing (valley followed by peak) and self-defocusing effect (peak followed by valley), respectively. The third-order nonlinear susceptibility ($\chi^{(3)}$) was determined from n_2 and β.

The relation between complex nonlinear refractive index ($n_{2,complex}$) and third order complex susceptibility ($\chi^{(3)}_{complex}$)is expressed by equation [147, 148],

$$n_{2,complex} = \frac{12\pi^2 \chi^{(3)}_{complex}}{n_0 n c} \tag{2.11}$$

$$n_{2,complex} = n_2 + i n_2^{'} \tag{2.12}$$

$$n_0 = n + i n_0^{'} \tag{2.13}$$

where n_0 is the complex refractive index. In addition, n and n_0' are the real and imaginary part of linear refractive index and n_2 and n_2' are the corresponding nonlinear refractive index coefficients, respectively.

The complex susceptibility ($\chi^{(3)}_{complex}$)is defined by the equation (2.14);

$$\chi^{(3)}_{complex} = \chi^{(3)'} + i\chi^{(3)''} \tag{2.14}$$

where $\chi^{(3)'}$ and $\chi^{(3)''}$ are the real and imaginary part of the third-order optical susceptibility, respectively. From equation (2.11) - (2.14), real and imaginary parts of the $\chi^{(3)}_{complex}$, was separated and are given by,

$$\chi^{(3)'} = 10^{-7} \frac{nc}{12\pi^2}(nn_2 - n_0' n_2') \tag{2.15}$$

$$\chi^{(3)''} = 10^{-7} \frac{nc}{12\pi^2}(nn_2' + n_0' n_2) \tag{2.16}$$

where the linear extinction coefficient, $n_0' = \frac{\alpha\lambda}{4\pi}$ and imaginary part of the nonlinear refractive index, $n_2' = \frac{\beta\lambda}{4\pi}$. From the measurement of n, n_2 and β, the real and imaginary parts of $\chi^{(3)}$ was determined for BST thin films as well as BTO, STO and BST films deposited for 180 min. duration.

2.4.9 Optical limiting (OL) set-up

Optical limiting (OL) is a property exhibited by nonlinear absorbing material where transmitted laser power initially increases with the incident laser power linearly up to certain point and beyond that the output power begins to saturate [149]. The point of onset deviation from linearity of the plot of output laser intensity versus incident laser is termed as OL threshold [150]. Alternatively, the transmission, T, ratio of output power to the input power, remains constant with the increase in laser power to a certain point and beyond this, it starts falling down with the incidence laser intensity.

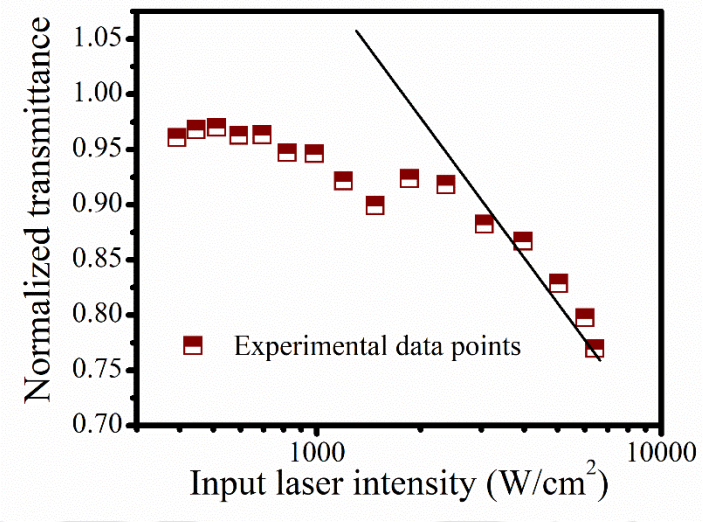

Figure 2-10 *Optical limiting behavior of a thin film.*

As an example, the OL response of one of the thin film is illustrated in Figure 2-10. The lower the values of the OL threshold, better the optical limiter [151]. Multi-photon absorption (MPA), RSA, excited state absorption (ESA), free carrier absorption (FCA), self-focusing and self-defocusing as well as nonlinear scattering all these nonlinear optical phenomena can be used to achieve OL. The OA data of the film listed in Table 2-7 and Cu layer infused BTO, STO and BST can be used to access the OL point. In OA, the intensity is varying with *z*, the distance w.r.t to focal spot. The input intensity (I_{input}) required for OL was calculated from the equation (2.17),

$$I_{input}(z) = \frac{P_0}{\frac{\pi w^2(z)}{4}} \tag{2.17}$$

where P_0 (= 30 mW) is the power measured just before the sample and w (z) is the beam radius as a function of z falling on the sample, represented by equation (2.18),

$$w^2(z) = w_0^2\left(1+\frac{z^2}{z_0^2}\right) \tag{2.18}$$

From equation (2.17) and (2.18), I_{input} (z) was falling on the sample and corresponding normalized output intensity obtained as detailed in Section 2.4.8 and transmittance of the film as a function of intensity was worked out by taking the ration of later to the former intensity.

2.4.10 Photoluminescence spectrometer

Photoluminescence (PL) spectroscopy is a widely used technique for characterizing the optical and electronic properties of semiconductors. PL is a contactless, nondestructive method of probing the electronic structure of materials. Light is directed onto the sample, where it is absorbed causing the photo-excitation. In this process, the excess energy can be dissipated by the sample through the emission of light, or luminescence. In the case of photo-excitation, this luminescence is called PL [152]. In the present thesis, steady-state PL measurements are carried out using a commercial PL spectrometer (model *Triax 550*) coupled to cooled CCD detector (make: *Jovin Yvon*) using an excitation wavelength of 355 nm.

2.5 Conclusions

In this chapter, the PLD setup for fabrication of perovskite and Cu nano-layer embedded perovskite thin films of BTO, STO and BST on quartz, Si (100) and MgO substrates has been described. The various characterization techniques adopted to investigate the structural, linear and nonlinear optical properties of PLD films were briefly discussed. The Z-scan set-up employed for the determination of NLO parameters was detailed.

Chapter 3 : Influence of substrate temperature and oxygen pressure on the linear, and nonlinear optical properties of $BaTiO_3$ thin films grown by PLD

Barium titanate ($BaTiO_3$, BTO) has been extensively studied in thin-film forms due to its high relative permittivity, dielectric constant, and large electro-optic coefficient [153-155]. BTO thin films have also been explored for potential applications in optical limiters, optical switches, and waveguides [136-138]. There are several techniques for fabricating the thin films of BTO as mentioned in Chapter 1. In the present chapter, the BTO thin films via PLD are detailed. The composition of particle plume in laser induced plasma and their kinetic energy in the PLD technique is commanded by the background gas pressure apart from the initial laser fluence focused on the target material. Therefore, the present chapter is devoted to the influence of background gas oxygen pressure and substrate temperature on structural, linear, and nonlinear optical properties of BTO thin films by the PLD technique.

3.1 Experimental details

Preparation of BTO target and details of the PLD setup have already been detailed in Section 2.1 and Section 2.3, Chapter 2, respectively. Two sets of BTO thin films via PLD were fabricated to study the role of temperature and background gas pressure on the properties of thin film. The films were deposited on silicon as well as on quartz substrate. The first set of films was deposited for 1 hr. duration each by varying T_s from 400 – 700 °C at a fixed laser fluence of 10 J/cm^2 and O_2 pressure of 0.1 mbar. The second set of films was fabricated to study the effect of O_2 gas pressure in the range of 0.005 to 1 mbar at a substrate temperature

of 700 °C keeping all the other deposition parameters same as stated above. All the films were subjected to FESEM and AFM for the morphological characterisation and surface roughness. The stoichiometry of the film was examined by EDX. The crystal structure, crystallite size, stress and strain of thin films was obtained by XRD analysis. Raman Spectrometer investigated the phase and vibrational modes of the thin films. Prior to film deposition, BTO target was also analysed for the elemental analysis and crystal structure. The linear optical properties (transmission, absorbance, thickness, and refractive index) of the films deposited on quartz substrate were studied by the UV-Visible-NIR spectrometer. Nonlinear optical properties of the films were characterized by a modified *Z*-scan technique using a cw Ar-Ion laser at 488 nm wavelength [133].

3.2 Characterization of BTO target

Figure 3-1 (a) shows the FESEM image of the sintered pellet of BTO. It exhibits very compact surface, and the grain distribution is uniform.

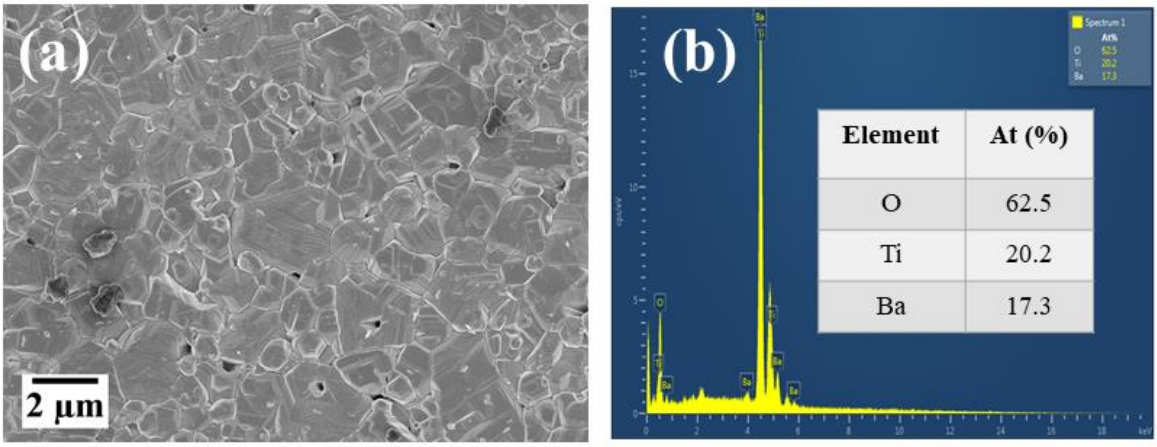

Figure 3-1 *(a) FESEM micrograph (b) EDX spectra of BTO sintered target and inset table shows the atomic percentage of barium, titanium, and oxygen elements of BTO target.*

The EDX measurement of BTO pellet is shown in Figure 3-1(b). The stoichiometry of the target was found to be $Ba_{0.88}Ti_{1.01}O_{3.12}$ having slight deviation from actual stoichiometry (Ba:Ti:O:: 1:1:3).

The XRD spectra of the BTO pellet along with Rietveld refinement is illustrated in Figure 3-2.

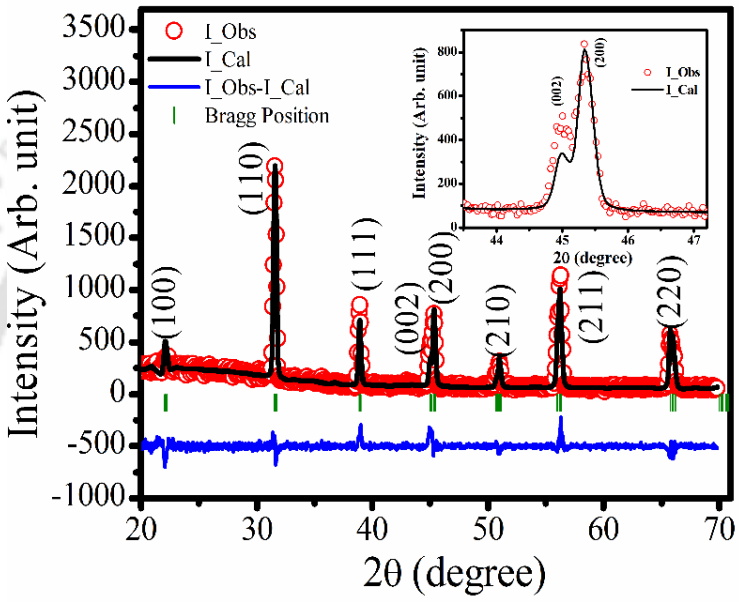

Figure 3-2 *Rietveld refined XRD spectra of BTO sintered pellet, and inset shows the splitting of (002) and (200) plane of BTO sintered pellet around 45°*

The presence of different diffraction planes (100), (110), (111), (002), (200), (210), (211), and (220), confirmed the formation of the tetragonal phase of BTO that belongs to the P_{4mm} space group (PDF Card No.: 01-084-9618) [156]. The splitting of the peak at 2θ = 45 º shown in the inset of Figure 3-2, corresponds to (200) and (002) twin crystal planes of the tetragonal structure of BTO [156]. The average crystallite size *(D)* of the BTO pellet was assessed using Debye-Scherer's formula equation (3.1), [157] and tabulated in Table 3-1.

$$D = \frac{k\lambda}{\delta \cos\theta} \tag{3.1}$$

where the shape factor (*k)* is 0.94 for spherical particles, the X-Ray wavelength (*λ)* is 1.5406 Å, $\delta$is FWHM of peaks, and θ is the Bragg's angle of diffraction.

The phase, lattice parameters (*a, b, c*), cell volume (*V*), cell density and crystallite size extracted from Reitveld analysis and are tabulated in Table 3-1.

Table 3-1 *Phase, a, b, c, cell volume (V), cell density and crystallite size (D) of BTO sintered pellet.*

Material	**Phase**	***a = b* (Å)**	***c* (Å)**	**Cell density (gm/cm^3)**	**Cell volume (*V*) ($Å)^3$**	**Crystallite size (*D*) (nm)**
BTO pellet	Tetragonal	3.99	4.03	6.02	64.42	66

BTO perovskite structure belongs to the O_h point group, and it has one molecule (5 atoms) per unit cell. Therefore, there are twelve (3x5-3) optical phonon modes. In the ideal cubic phase of BTO ($P_{m\text{-}3m}$), the zone center optical phonon modes belong to the Γ_{opt}^{cubic} = $3F_{1u}+F_{2u}$ irreducible representations and no first-order Raman active modes exist [45]. Raman modes arise when crystal symmetry breaking takes place in the material. In its tetragonal phase, each triply degenerate cubic F_{1u} mode splits into A_1+E modes, while the F_{2u} silent vibrational mode splits into B_1+E modes, resulting in $3A_1 + B_1 + 4E$ modes. Thus, $\Gamma_{opt}^{tetragonal}$ = $3A_1$+ 4E +B_1 [158]. Due to the long-range electrostatic forces associated with lattice ionicity, these modes were further divided into longitudinal (LO) and transverse (TO) components [159]. Thus, the following distinct Raman-active optical lattice vibrations for the BTO pellet in its tetragonal phase were obtained: $3A_1$ (TO) + $3A_1$ (LO) + 3E (TO) + 3E (LO) + 1E (LO + TO) + $1B_1$. Figure 3-3 shows the Raman spectra of the BTO target in the range of 100-900 cm^{-1} obtained by exciting it with a 488 nm line of Argon ion laser.

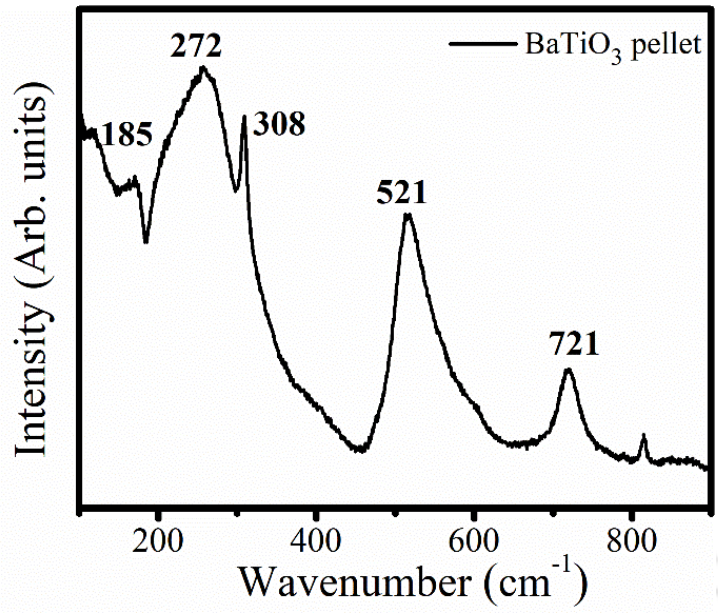

Figure 3-3 *Raman spectra of a BTO sintered pellet.*

The observed bands located at 185, 272, 308, 521, and 721 cm^{-1} were in good agreement with the Raman bands of BTO single crystal, as reported in the literature [160]. The A_1 (TO_1) mode was ~185 $cm^{-1,}$ whereas a broad A_1 (TO_2) mode was spotted around 272 cm^{-1}. Next, the third asymmetric A_1 (TO_3) mode was observed at around ~532 cm^{-1} also coupled weakly with the A_1 (TO_2) mode. The E (TO_2) mode at 308 cm^{-1} was mixed with the broad band A_1 (TO_2) mode, and another Raman band was seen at ~742 cm^{-1} (A_1 (LO_3), specific to the tetragonal phase of BTO. Thus, the Raman spectra also confirmed that the BTO pellet has a tetragonal structure, in agreement with the XRD results.

3.3 Effect of substrate temperature on PLD deposited BTO thin films

In this section, effect of substrate temperature on structural, optical, and nonlinear optical properties of BTO thin films via PLD is detailed.

3.3.1 Surface characterization and EDX analysis of BTO thin films via PLD as a function of substrate temperature

Figure 3-4 (a) – (e) shows the FESEM images of BTO thin films deposited on a quartz substrate at various deposition temperatures, T_s, of 400, 500, 600, 650, and 700 °C, respectively at a background O_2 gas pressure of 0.1 mbar.

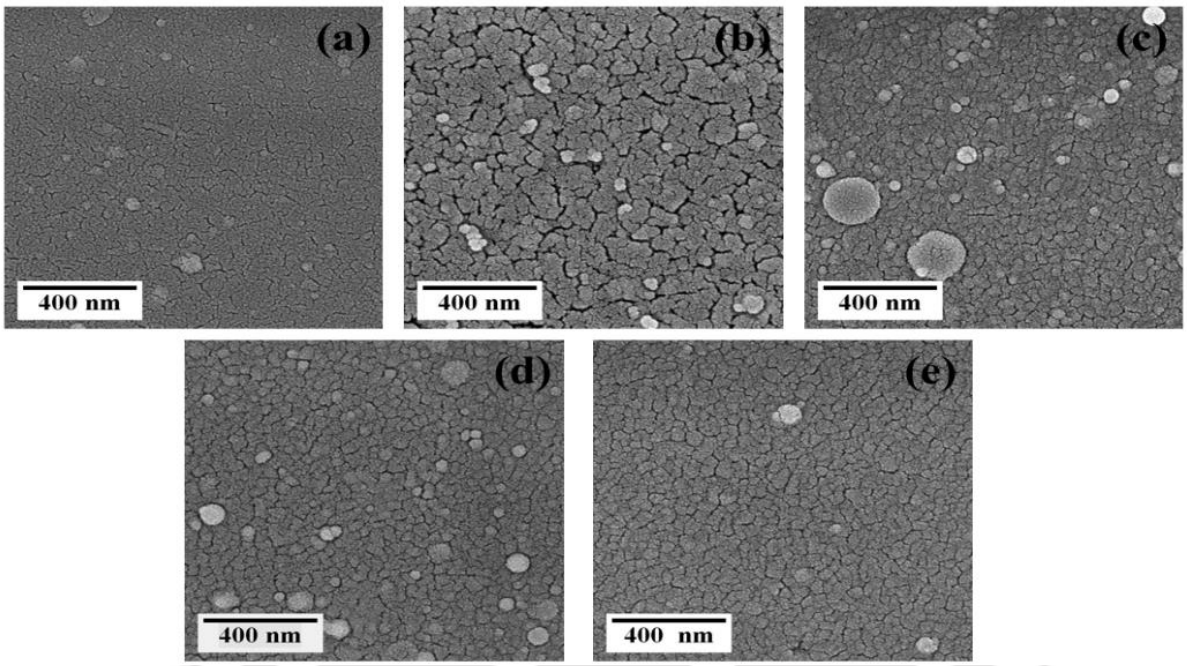

Figure 3-4 *FESEM images of PLD deposited BTO thin films for 1 hr. deposition at T_s (a) 400, (b) 500, (c) 600, (d) 650, and (e) 700 °C on quartz substrate.*

The BTO thin film deposited at 400°C showed a relatively uniform surface. The appearance of a well-defined granular structure was visible for the rest of the samples, along with some droplet formations. The film deposited at 700 °C exhibited a uniform and densely packed structure. This is due to the dependence of diffusion process on the temperature.

The relationship between the surface diffusion coefficient (D_s) and the temperature (T) is given by [161],

$$D_s = D_{so} \exp(\frac{-E_A}{K_B T}) \tag{3.2}$$

where D_{so} is the pre-exponential factor, E_A is the activation energy for the surface diffusion jump, K_B is the Boltzmann constant, and T is the substrate temperature in kelvin. According to equation (3.2), an increase in substrate temperature causes a high diffusivity of the adatoms, leading to the uniform smooth and compact surface.

Figure 3-5 (a) – (e) displays the EDX spectra of BTO thin films deposited on a Si substrate as a function of substrate temperature at a background O_2 pressure of 0.1 mbar. EDX spectra indicate the presence of barium, titanium, and oxygen in all these thin films. The stoichiometry of thin film fabricated at a substrate temperature of 700 ºC, was more close to that of the BTO target.

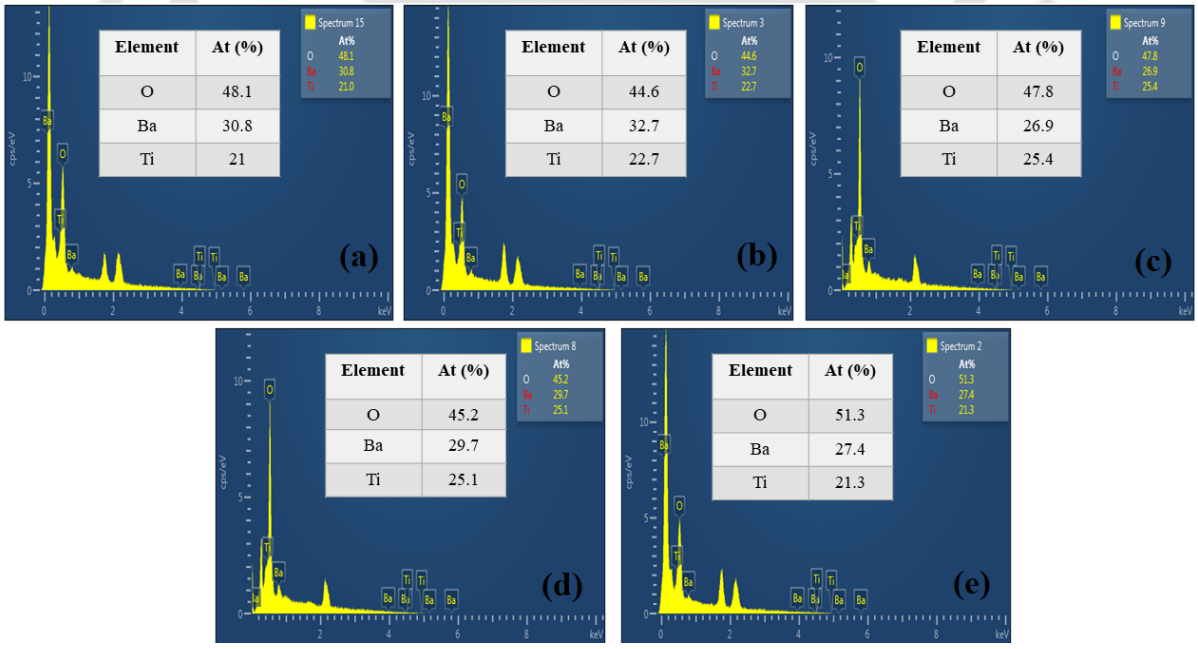

Figure 3-5 *EDX spectra of PLD deposited BTO thin films for 1 hr. deposition at T_s (a) 400, (b) 500, (c) 600, (d) 650, and (e) 700 °C on Si substrate and inset table shows the atomic percentages of barium, titanium and oxygen elements.*

Two-dimensional AFM images of BTO thin films are shown in Figure 3-6 (a) – (e). The RMS roughness of the BTO thin films is plotted as a function of substrate temperature in Figure 3-6 (f).

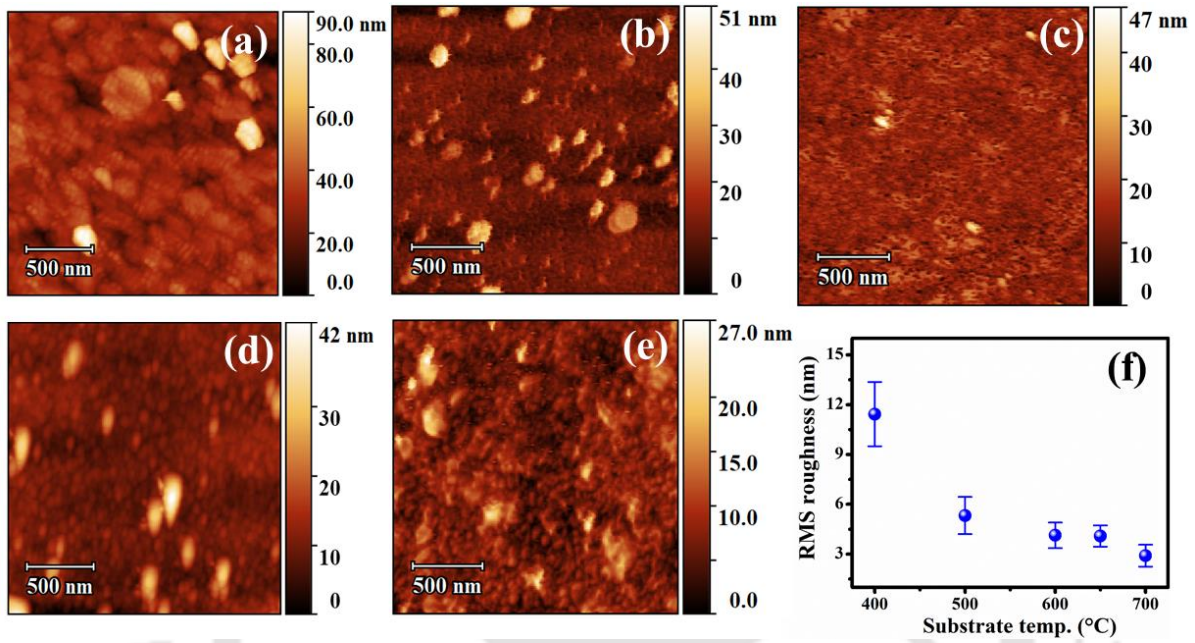

Figure 3-6 *Two dimensional AFM images of BTO thin films deposited at T_s (a) 400, (b) 500, (c) 600, (d) 650, and (e) 700 °C on quartz substrate and (f) average RMS roughness of the BTO thin films as a function of T_s. The vertical error bar on each data point represents the standard deviation of RMS roughness deduced from three scan areas.*

It was observed to be 11.43 ± 1.93, 5.32 ± 1.12, 4.15 ± 0.77, 3.19 ± 0.64 and 2.93 ± 0.66 nm for T_s of 400, 500, 600, 650 and 700 °C, respectively. The decrease in RMS roughness value with an increase in temperature is attributed due to uniform grain growth at higher T_s. Similar behaviour was reported in the literature for some other thin films [135].

3.3.2 XRD analysis of BTO thin films as a function of substrate temperature

Figure 3-7 (a) - (b) illustrate the XRD spectra of the BTO thin films fabricated at T_s of 400 and 500 °C on n-type Si (100) substrate, respectively. These films exhibited broad and weak characteristic XRD peaks at 2θ = 28.7º corresponding to the (110) plane of BTO. The peak marked (*) was due to the crystalline silicon substrate. Figure 3-7 (c) – (e) shows the Reitveld refined XRD pattern of thin films deposited at T_s 600, 650, and 700 °C, respectively.

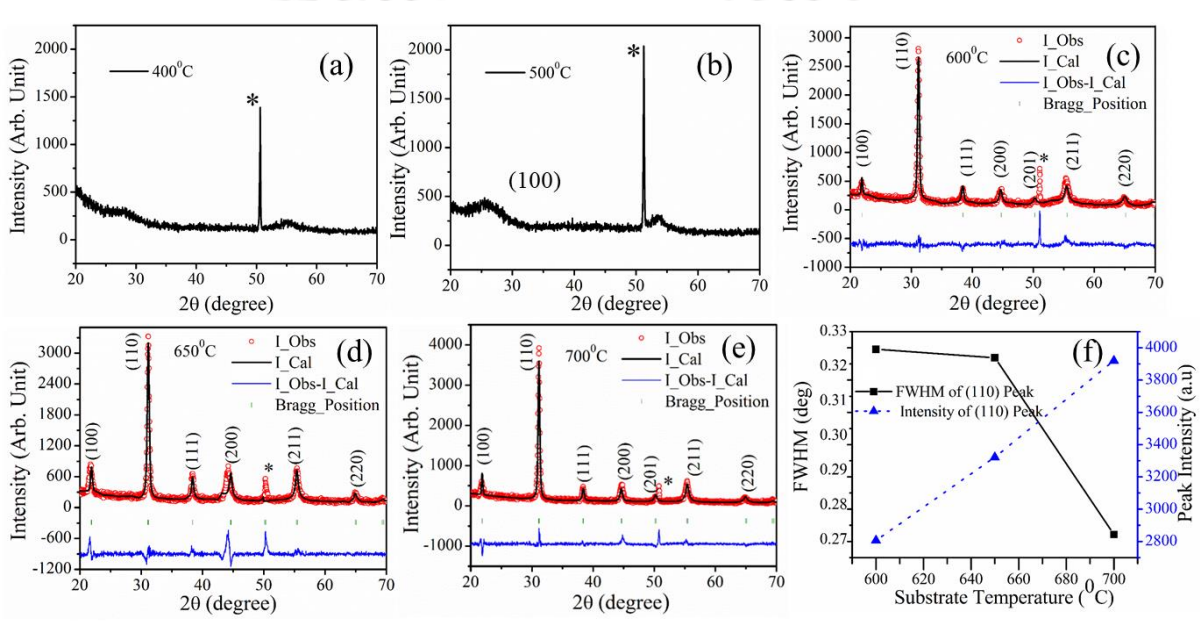

Figure 3-7 *BTO thin films deposited on crystalline Si substrate at T_s (a) 400 and (b) 500 ºC, Rietveld refined XRD spectra (c) 600, (d) 650, (e) 700 ºC at fixed 0.1 mbar oxygen pressure, and (f) variation in FWHM and peak intensity of (110) plane as a function substrate temperature.*

These three films displayed a strong peak of BTO corresponding to the (110) plane confirming the preferential cubic symmetry belonging to the $P_{m\text{-}3m}$ space group [162]. There were also appearances of other relatively weak peaks corresponding to (100), (111), (200), (201), (211), and (220) planes [163]. Figure 3-7 (f) exhibits the plot of FWHM and peak intensity for XRD spectra corresponding to (110) plane as a function of T_s, indicating the increase in crystallinity of the films with increasing T_s. The crystallite size of BTO thin films was found using equation

(3.1). The values of crystallite size, lattice parameters, cell volume, and cell density of the thin films were extracted from the refinement for all the planes and are listed in Table 3-2.

The strain (ε) developed in BTO thin films was estimated from the equation [164],

$$\varepsilon = \frac{(a_f - a_0)}{a_0} \tag{3.3}$$

where a_f is the a-axis lattice parameter of the film and a_0 (= 4.03 Å) is that of bulk BTO crystal, (obtained from the database of PDF card no.: 01-084-9618, ICSD collection code: 252562). The value of strain was calculated and is listed in Table 3-2. The stress (σ) developed in the BTO films is calculated using the following formula[164],

$$\sigma = (C_{11} + C_{12} - \frac{2C_{13}^2}{C_{33}})\varepsilon \tag{3.4}$$

where C_{11},C_{12},C_{13} and C_{33} are elastic constants for cubic BTO single crystal [165]. However, among these four elastic constants, C_{11} and C_{12}only exist for cubic BTO crystal. The values of C_{11} and C_{12} of BTO cubic crystal are 173, and 82, respectively [166] and the values of stress in the BTO thin films are listed in Table 3-2.

Table 3-2 *a, b, c, D, V, cell density, strain and stress of the BTO thin films as a function of* T_s.

Substrate temp. (T_s) (°C)	**Phase**	***a* = *b* = *c* (Å)**	**Crystallite size (*D*) (nm)**	**Cell volume (*V*)(Å^3)**	**Cell density (gm/cm^3)**	**Strain (ε) x10^{-3}**	**Stress (σ) (GPa)**
600	Cubic	4.06	13	67.04	5.76	7.44	1.79
650	Cubic	4.06	15	66.78	5.77	7.44	1.79
700	Cubic	4.05	18	66.13	5.79	4.96	1.28

From Table 3-2 , it is clear that there was only a marginal change in lattice parameters of these thin films with the increase in substrate temperature T_s. The crystallite size and cell density of the films are increasing with the increase in T_s. In addition to this, the decrease in strain and stress is due to the enhancement in crystallite size and compactness at higher substrate temperature from 600 to 700 °C and was also confirmed by FESEM images, Figure 3-4. Similar features of BTO films were reported for the film prepared by rf magnetron sputtering [105].

The XRD spectrum of BTO film deposited on quartz substrate at 700 ºC, and at an oxygen pressure of 0.1 mbar along with Reitveld refinement is shown in Figure 3-8, and all the extracted parameters from this are listed in Table 3-3.

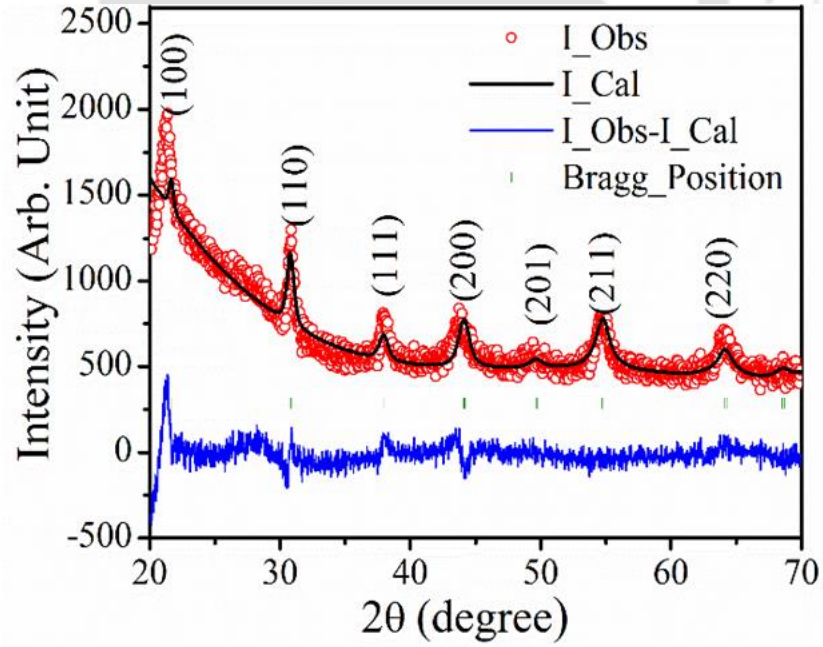

Figure 3-8 *Reitveld refined XRD spectrum of BTO thin film deposited on quartz substrate at T_s 700 °C and 0.1 mbar oxygen pressure.*

Table 3-3 *Phase, a, b, c, D, V, cell density, stress and strain of BTO thin film deposited on the quartz substrate.*

Substrate temp. (°C)	**Phase**	***a* = *b* = *c* (Å)**	**Crystallite Size (*D*) (nm)**	**Cell Volume *V* (Å)^3**	**Cell density (gm/cm^3)**	**Strain (ε) x10^{-3}**	**Stress (σ) (GPa)**
700	Cubic	4.08	14	68.10	5.68	12.41	3.16

The observed broadband features ranging from 20° to 25°, Figure 3-8, observed in thin films is due to the amorphous nature of the quartz substrate. This film also displayed similar planes corresponding to cubic crystal structure as that of the film deposited on the silicon substrate, Figure 3-7. The intensity of the (110) plane was more than that of the other planes, but due to the amorphous substrate, it was not dominating in contrast to that of the Si substrate. The value of strain and stress of BTO thin film deposited on a quartz substrate was increased compared to that of deposited on a silicon substrate due to the more mismatch in the thermal expansion coefficients of the BTO thin film on the quartz substrate as compared to that of Si.

3.3.3 Raman spectra of PLD BTO thin films deposited at various substrate temperatures

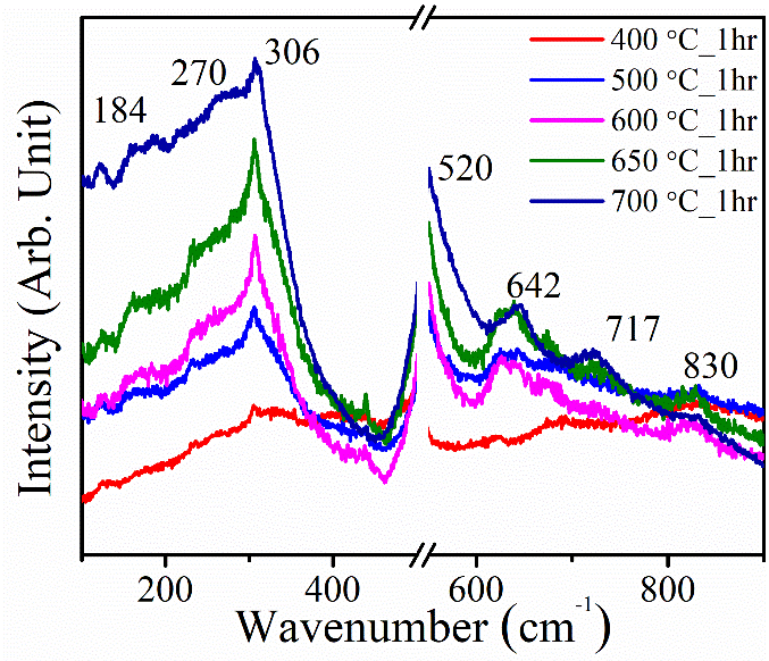

Figure 3-9 *Raman spectra of the BTO thin films deposited on Si substrate prepared at different T_s.*

Room temperature Raman spectra in the spectral range of 100 to 900 cm^{-1} of BTO films deposited on Si substrate are depicted in Figure 3-9. The Raman bands of BTO films were observed at 184, 270, 306, 520, 642, 717 and 830 cm^{-1} for different substrate temperatures [167].The 184 cm^{-1} band corresponds to E (TO) / E (LO) / A_1 (LO) mode. A broad A_1 (TO_2) mode was at 272 cm^{-1}. The E (TO+ LO) mode is associated with both tetragonal and cubic phases at 306 cm^{-1}. Lu et al. reported that the peak near 306 cm^{-1} is reduced in its sharpness and becomes indistinguishable when the cubic phase of BTO is dominant [168]. The third asymmetric A_1 (TO_3) mode was observed around 520 cm^{-1} corresponds to Raman peak of the silicon substrate. The 642 cm^{-1} peak corresponds to A_1 (LO) and E (LO) modes, which arises due to internal stress in the deposited films. The mixture of A_1 (LO_3) and E (LO_3) modes was spotted at 717 cm^{-1}. The higher Raman shift at 830 cm^{-1} was attributed to the impurity phases

at film-substrate interfaces [3]. The absence of any peak in the film deposited at 400 ºC indicated the amorphous nature in agreement with that of XRD results, in Figure 3-7. All these observations lead to the conclusion that the BTO thin films were in the pseudocubic phase. A similar feature was also reported in the literature [169].

3.3.4 UV-Visible-NIR spectra of PLD BTO thin films fabricated at various substrate temperatures

The UV-Visible NIR transmission spectra of the films deposited at an oxygen pressure of 0.1 mbar on quartz substrate at all five T_s are shown in Figure 3-10 (a). The distinct appearance of interference fringes indicated the excellent surface quality of these films. The transmittance of these BTO thin films lies within the range of 75 - 85% in the visible spectrum. The absorption edge of these films lied in the wavelength range of 200 - 400 nm. The Swanepoel envelop method was employed to estimate the refractive index and thickness of the films, as discussed in Section 2.4.7, Chapter 2 [143].

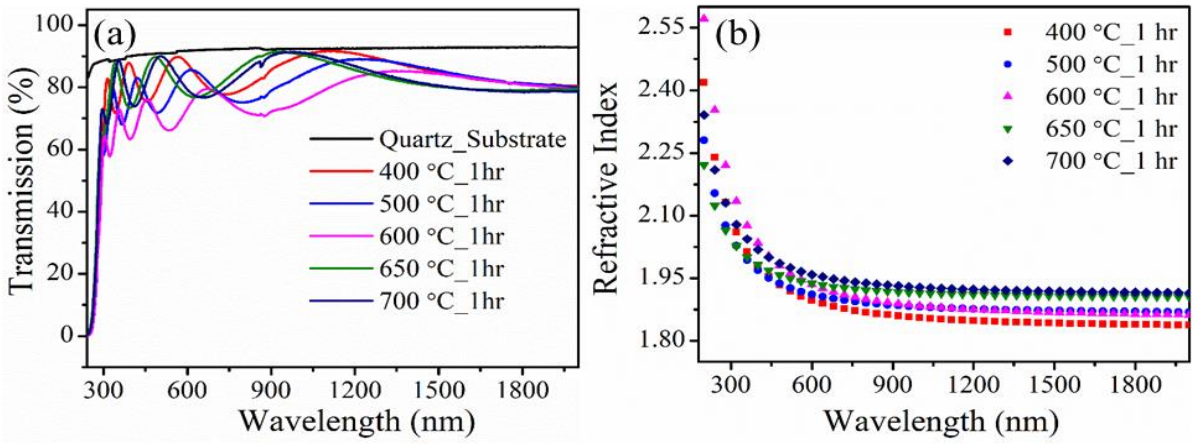

Figure 3-10 *(a) UV-Visible-NIR transmission spectra of PLD deposited BTO thin films at different T_s and (b) refractive index variation as a function of wavelength at different T_s.*

The refractive indices (n) for all films as a function of wavelength (λ) were calculated using the expression given by equation (2.3). The refractive index values were in the range of

1.93 - 1.99 at a wavelength of 488 nm for the films deposited at various substrate temperatures. The refractive index, *n*, of the film deposited at 400 °C was found to be 1.93, while that for films fabricated at elevated T_s of 500 and 600 °C are 1.94 and 1.96, respectively. After that, it rises to 1.97 for 650 °C films and then increases to 1.99 for the film deposited at 700 °C. The increase in the refractive index was observed with an increase in substrate temperature accounted for dense and improved crystallization of films at a higher substrate temperature, which was in agreement with XRD results. Further, similar characteristics were reported in the literature for BTO thin films deposited by other techniques [105, 170, 171]. The thickness of these films was calculated using the equation (2.4). The thickness for all these films deposited at different T_s of 400, 500, 600, 650, and 700 °C was found to be 310, 327, 336, 259, and 256 nm, respectively. It was observed that with an increase in T_s from 400 to 600 °C, the film thickness was gradually increased from 310 to 336 nm, and then it started decreasing finally to 256 nm for the film at T_s 700 °C. At higher substrate temperature, the adatoms are settled down properly on the surface in densely packed form, attaining higher crystallinity. The film thickness is also dependent on the physical parameters; sticking coefficient re-evaporation rate and surface diffusion coefficient of adatoms. The sticking coefficient beyond certain temperature reduces whereas re-evaporation rate increases with the temperature. Surface diffusion also increases with the temperature. Thus, due to all these, the thickness of the thin film is reduced at higher substrate temperature. The absorption coefficients for all the samples at 488 nm were calculated using equation (2.6) and listed in Table 3-4.

3.3.5 Nonlinear optical properties via Z-scan for the PLD thin films of BTO as a function of deposition substrate temperature

The third-order nonlinear optical property of BTO thin films deposited on quartz substrate was determined from the modified *Z*-scan technique [129].

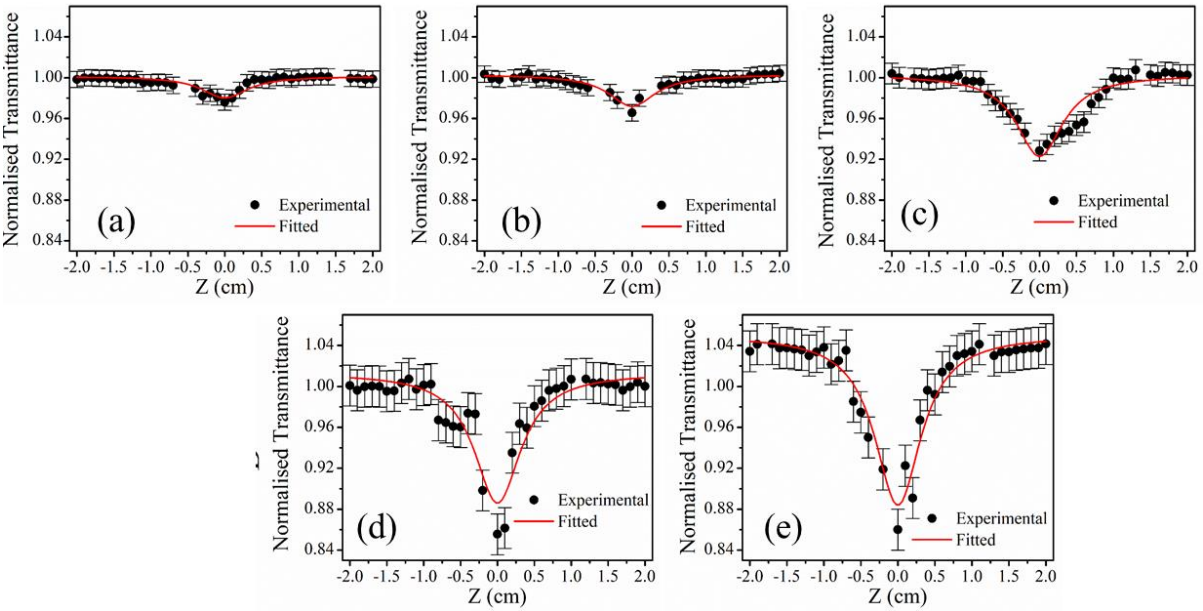

Figure 3-11 *OA Z-scan traces of PLD deposited BTO films (a) 400 ,(b) 500 ,(c) 600,(d) 650, and (e)700 °C. The solid lines depict the theoretical fit.*

The OA *Z*-scan spectra shown in from Figure 3-11, at the focal plane, $z = 0$, the intensity is minimum suggesting the RSA behavior. The error bars in the data points are the standard deviations calculated over 10 consecutive measurements for each and every location of *z*. Nonlinear absorption in the thin films could be due to MPA, FCA, ESA, nonlinear scattering, etc. [135]. In present case, as the excitation photon energy exceeds half of the bandgap energy of the film, the absorptive nonlinearity is expected to be due to the MPA (mainly two photon absorption) [129]. The OA Z-scan data fitted to equation (2.8) are also shown in Figure 3-11 (a) - (e).

The values of β, obtained from equation (2.8), are listed for all the films deposited on quartz substrate in Table 3-4.

Table 3-4 *Values of α and β for the BTO thin films deposited at various T_s.*

Substrate temp. (T_s) (°C)	***L* (nm)**	**L_{eff} (nm)**	**α (λ = 488 nm) (cm^{-1}) x 10^{-4}**	**β (cm/W)**
400	310	267	9.67	9.28 ± 0.04
500	327	277	10.40	24.82 ± 0.04
600	336	317	3.46	48.50 ± 0.06
650	259	245	4.49	55.24 ± 0.03
700	256	236	5.22	57.54 ± 0.06

The value of β for the BTO films was observed to be increasing from 9.28 to 48.5 cm/W with the increase in T_s from 400 to 600°C. Further, it increased to 55.24 cm/W for 650 °C thin films, and finally attained a maximum value of 57.54 cm/W for 700 °C thin films. The increase in the value of β with the increase in substrate temperature was due to the improved crystallinity of thin film. In addition to this, a rough surface leads to more scattering losses which directly affects the nonlinear optical properties. The films having low RMS surface possess higher nonlinear absorption coefficient. In this present manuscript, the RMS surface roughness is declined from 11.4 to 2.9 nm for the substrate temperature from 400 to 700 °C and β value is enhanced from 9.28 to 57.54 cm/W for the substrate temperature from 400 to 700 °C respectively. This is also supported by the literatures [172, 173]. Significantly large values for nonlinear absorption coefficient were obtained for BTO films compared to those reported in the literature using the *Z*-scan technique [9, 36, 174].

3.4 Effect of oxygen pressure PLD deposited thin films

In the previous section, it was observed that the films deposited at 700 °C possessed minimum RMS surface roughness, best crystallinity, and maximum NLA coefficient. In order to acquire the optimum deposition pressure background gas, second set of films was deposited at 700°C at several background oxygen pressure in the range of 0.005 to 1 mbar.

3.4.1 FESEM and EDX spectra of BTO thin films deposited at various oxygen pressure

The FESEM images of BTO thin films prepared at various oxygen pressure; 0.005, 0.05, 0.1, 0.5, and 1 mbar on the quartz substrate are shown in Figure 3-12 (a) - (e).

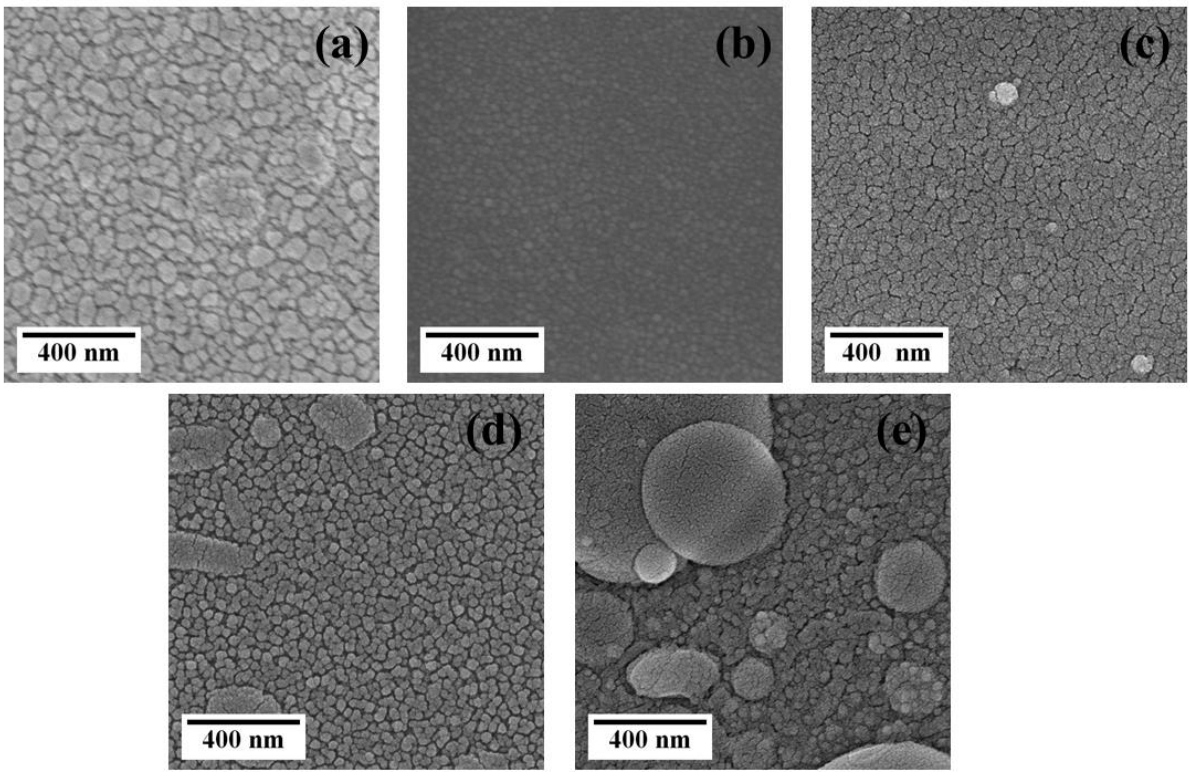

Figure 3-12 *FESEM images of PLD deposited BTO thin films on quartz substrate (a) 0.005, (b) 0.05, (c) 0.1,(d) 0.5,(e) 1 mbar.*

It was observed that the films deposited at lower oxygen pressure develop cracks on the surface. Subsequently, cracks disappeared with the increase in oxygen pressure, and uniformly distributed grains were observed up to 0.1 mbar. Apart from this, at a pressure of 0.5 and 1 mbar, there is a uniform distribution of grains and the formation of the droplets on the film's surface. Similar features were also documented in the literature for other perovskites thin film deposited via PLD [175].

Figure 3-13 (a) – (e) shows the EDX spectra of BTO thin films deposited on Si substrate, as a function of oxygen pressures (O_2) of 0.005, 0.05, 0.1, 0.5 and 1mbar, respectively.

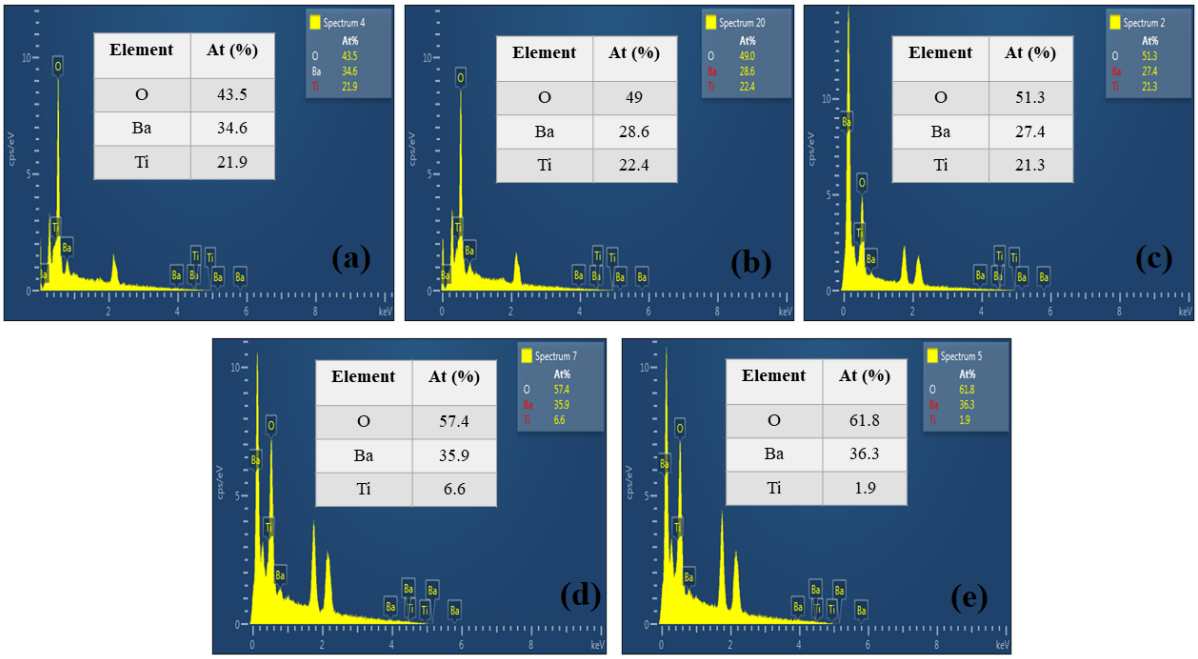

Figure 3-13 *EDX spectra of PLD deposited BTO thin films on Si substrate (a) 0.005, (b) 0.05, (c) 0.1, (d) 0.5, and (e) 1 mbar and inset table shows the atomic percentages of barium, titanium and oxygen elements for all the thin films.*

The presence of barium, titanium, and oxygen elements was also confirmed in all these thin films deposited at various oxygen pressures. The stoichiometry of the film deviates w.r.t to the target at low and higher pressure of background gas oxygen. It is more close to that of the target at 0.1mbar. This behaviour with the oxygen pressure can be explained in the following manner. In PLD scheme, with the focusing of high power laser onto the target, its constituent molecule completely dissociates in its atomic and corresponding ionic specie along with liberated electrons, thus furnishing the formation of Laser induced plasma (LIP) plume. This plasma plume travels forward and reacts with the constituent species to form the molecules back and impinges on the substrate resulting in the formation of the thin film. The expansion of LIP is nearly hemispherical and the deposition takes place at a distance of 4 cm from the target. Therefore, under the low pressure of back ground gas the lightest atom, oxygen (atomic mass no.16) in the present case will be moving faster (also scattered more) compared to that of other atomic species and changing the stoichiometry of the plume and thus the film deposited at low pressure will be oxygen deficient and deviating from the stoichiometry of the target. Oxygen deficiency can be easily compensated by depositing the film at higher background pressure. But if the pressure is too large then Ti atoms being lighter as compared to that of Ba will be scattered more due to the collisions with the various species present in the LIP plume as well as with background gas molecule and so these films will be highly deficient in Ti. Thus, only at certain optimum pressure of background gas, oxygen, the plume will retain its stoichiometry close to that of the target and giving rise to nearly stoichiometric film. In the present case, it is observed that at a pressure of around 0.1 mbar the stoichiometry of the BTO film is more close to that of target as compared to that of low pressure where the film is oxygen deficient and at higher pressure Ti deficient film is formed.

3.4.2 RMS surface roughness via AFM

AFM 2D images, over a scan area of 2 µm x 2 µm, of thin films deposited at various oxygen pressures from 0.005 to 1 mbar are shown in Figure 3-14 (a) - (e).

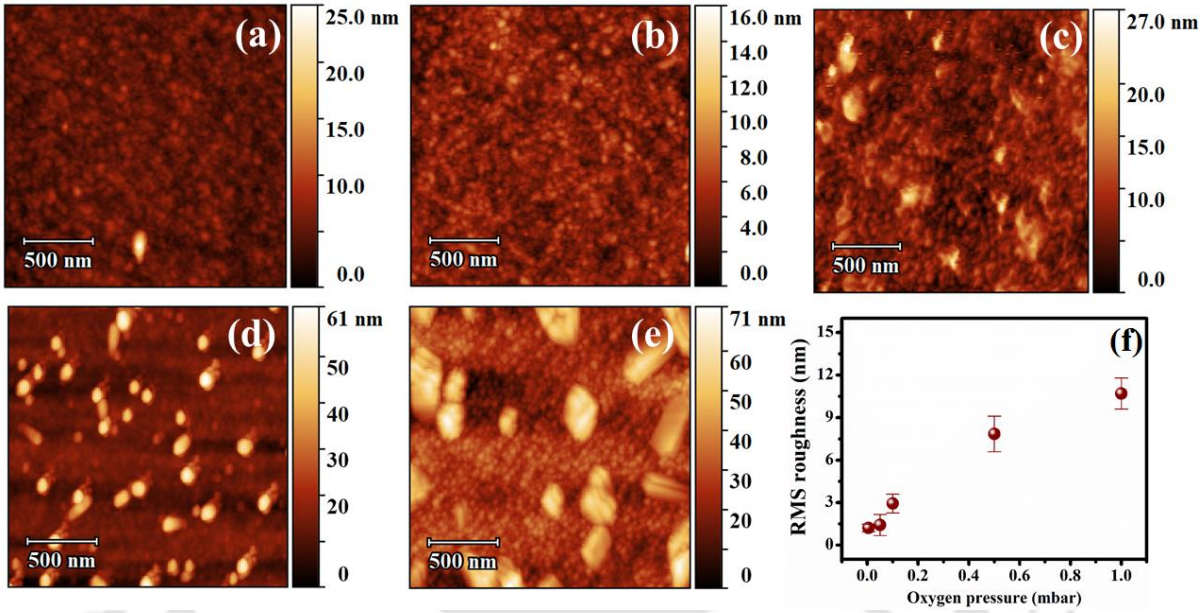

Figure 3-14 *Two dimensional AFM images of BTO thin films deposited at different oxygen pressures on Si substrate (a) 0.005,(b) 0.05,(c) 0.1, (d) 0.5, (e) 1 mbar, and (f) average RMS roughness of the BTO thin films as a function of oxygen pressure.*

The RMS surface roughness was obtained from these AFM images by moving it at three-four different places on each and every film and average of each is plotted as a function of oxygen pressure in Figure 3-14 (f). The RMS roughness was found to be (1.21 ± 0.17) nm (0.005 mbar film), (1.41 ± 0.74) nm (0.05 mbar film), (2.93 ± 0.66) nm (0.1 mbar film), (7.85 ± 2.29) nm (0.5 mbar film), and (10.71 ± 3.09) nm (1 mbar film). Due to the confinement of the laser-induced plasma at higher pressure, the particle flux arriving at the substrate is highly non-uniform, which increases surface roughness [176]. In the literature, similar features have been reported [177-179].

3.4.3 XRD analysis of BTO thin films as a function of deposition pressure

Figure 3-15 (a) – (e) illustrates the XRD pattern of BTO thin films on Si (100) substrate fabricated at different oxygen pressure, from 0.005 to 1 mbar, along with Reitveld refinement Bragg's reflections, and difference of experimental and calculated pattern. The XRD spectra of the thin films depicted (100), (110), (111), (200), (210), (211), and (220) planes which are signature peaks of cubic BTO with $P_{m\text{-}3m}$ space group similar to that of films deposited at different substrate temperatures. The peak marked (♣) in Figure 3-15 (d) and (e), deposited at 0.5 and 1 mbar, is assigned to BTO secondary phase formation. The presence of the secondary phase was attributed to the coexistence of both cubic and tetragonal phases [180].

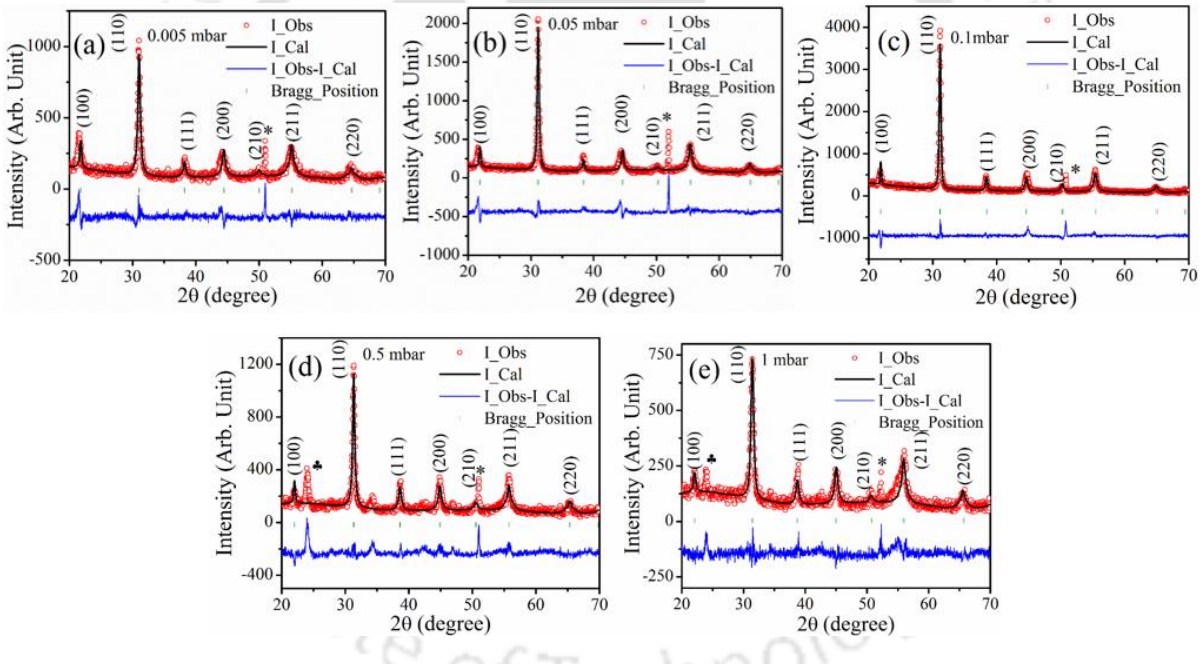

Figure 3-15 *Rietveld refined XRD pattern of BTO thin films deposited at various oxygen pressure on Si substrate (a) 0.005, (b) 0.05, (c) 0.1, (d) 0.5, and (e) 1 mbar.*

There are hardly any significant changes in the observed lattice parameters of the thin films as a function of deposited oxygen pressure. The obtained crystallite size for the thin films was in the range of 11–18 nm. The film deposited at 0.005 mbar having a smaller crystalline size of 11 nm was increased with the increase in oxygen pressure at 0.1 mbar and was found

to be 18 nm. Then the crystallite size dropped to 13 nm for 1 mbar thin film. A significant improvement in the peak intensity of the (110) plane was also observed with the rise in O_2 pressure up to 0.1 mbar, and then it started falling with the further increase of oxygen pressure. The crystallite size, lattice parameter, unit cell volume, cell density, strain and stress of thin films extracted from refinement analysis are listed in Table 3-5.

Table 3-5 *Phase, a, b, c, D, V ,cell density, strain and stress of BTO thin film deposited at a different oxygen pressure.*

Oxygen pressure (mbar)	**Phase**	***a = b = c* (Å)**	**Crystallite size (*D*) (nm)**	**Cell volume V (Å^3)**	**Cell density (gm/cm^3)**	**Strain (ε) x10^{-3}**	**Stress (σ) (GPa)**
0.005	Cubic	4.07	11	67.91	5.27	9.92	2.53
0.05	Cubic	4.06	14	66.62	5.63	7.44	1.79
0.1	Cubic	4.05	18	66.13	5.79	4.96	1.28
0.5	Cubic	4.06	15	66.75	5.72	7.44	1.79
1	Cubic	4.06	13	66.82	5.69	7.44	1.79

Background oxygen pressure is an important controlling parameter for the dynamics of plasma plume and hence the growth of thin films deposited by the PLD technique, and thus, it should be optimized for the given film for a specific crystal structure. At lower pressure, plasma expansion is relatively a sort of free expansion and thus, the particle density in the plume is low as it approaches the substrate, and impinges at high kinetic energy. The excess kinetic energy is transferred to the substrate due to the local heating, as BTO particles fuse on the substrate inhibiting the mobility of the molecules. Also, the sputtering of the impinging particles at higher kinetic energy cannot be ruled out; as a result, the film crystallinity is of

poor quality along with the low thickness. With increasing background oxygen pressure, the plasma plume is confined; thus, particle flux in it increases, and simultaneously due to excessive collisions, it lowers its kinetic energy and so the BTO particles on arrival on the surface can diffuse easily onto the substrate surface acquiring the thermodynamically stable locations of lower energy sites and form the low energy structure, which leads to enhancement of the film crystallinity and also the thickness of the film. With the further increase in the pressure to 1 mbar, the plasma is over confined in a small region and due to increasing collision between plasma particles and oxygen atoms; there is a large reduction in the kinetic energy before falling on the substrate; as a result, the film characteristics deteriorates along with the lowering of the thickness. This was exactly observed in the present case; the film quality improved with the increasing pressure up to 0.1 mbar and decreased afterward. A similar trend was observed in the thickness (Table 3-6). Therefore, it can be concluded that in the present case, the optimum background pressure of oxygen is 0.1 mbar. Similar features in the literature were documented for many other varieties of films via PLD [179]. At optimum pressure (0.1 mbar), stress and strain both are minimum (Table 3-5).

3.4.4 Raman spectra of BTO thin films deposited at various oxygen pressure

Room temperature micro-Raman spectra of the BTO films deposited on Si (100) substrate at various oxygen pressure are shown in Figure 3-16.

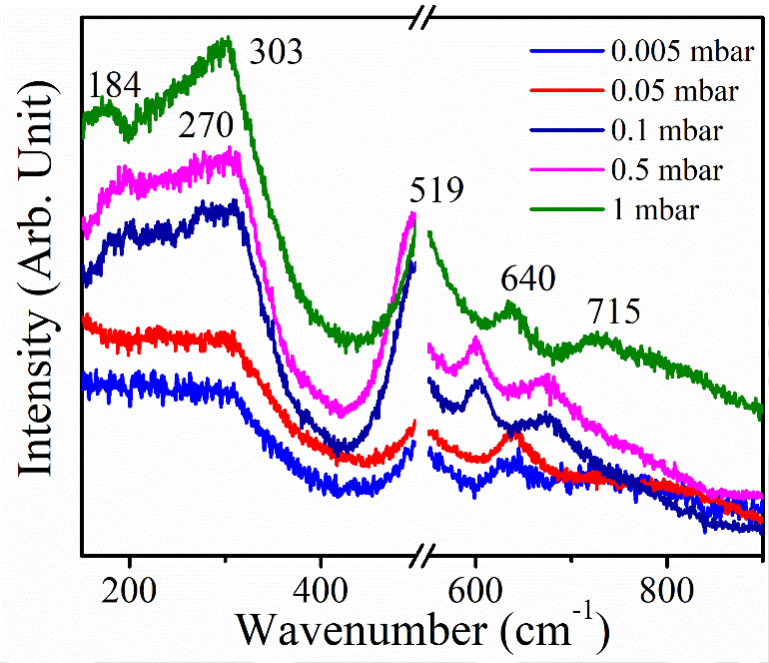

Figure 3-16 *Raman spectra of the BTO thin films fabricated at different oxygen pressures on Si substrate.*

The six significant peaks, similar to those mentioned in previous sections, were observed at 184, 270, 303, 519, 640, and 715 cm^{-1} corresponding to A_1 (LO), $A_1(TO_2)$, E (TO+ LO), $E(TO_3)$, $A_1(LO)$, and $A_1(LO_3)$+E (LO_3) Raman modes for all the pressures [181]. These modes of BTO thin films deposited at lower oxygen pressure were at slightly higher frequencies (blue-shift) than Raman peaks of BTO single crystal and film prepared at optimum oxygen pressure [160]. Raman peaks become broader and more asymmetric, which could be influenced by oxygen vacancies at low pressure. At optimum pressure of oxygen, the BTO film is more stoichiometric than lower or higher pressures [182]. Moreover, increasing the oxygen pressure from 0.005 to 1 mbar, the distinct appearance of the 303 cm^{-1} peaks is

improving, indicating the reduction in oxygen vacancies of BTO thin films at higher deposition pressures [181] as is also indicated by EDX, Figure 3-13.

3.4.5 Refractive index and thickness of the PLD BTO films via UV-Vis-NIR spectra

The UV-Visible-NIR transmission spectra of this set of BTO thin films are shown in Figure 3-17 (a), and the corresponding refractive indices calculated using equation (2.3) are shown in Figure 3-17 (b).

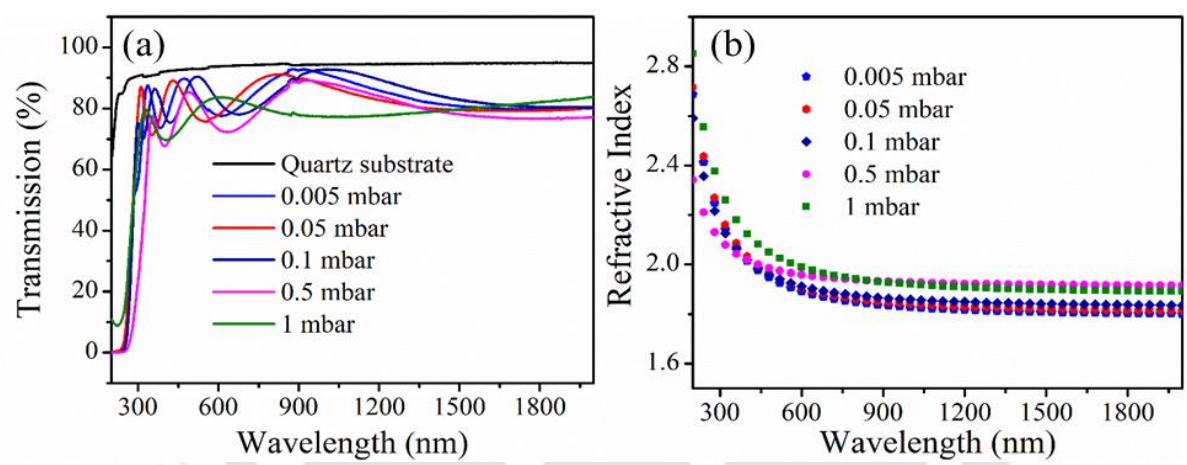

Figure 3-17 *UV-Visible-NIR transmission spectra of BTO thin films as a function of wavelength at various oxygen pressure and (b) refractive index variation as a function of wavelength.*

The film thickness estimated by the envelope method was found to be 231, 240, 256, 212, and 162 nm for O_2 pressure of 0.005, 0.05, 0.1, 0.5, and 1 mbar, respectively. This has already been explained based on the confinement of the plasma plume and hence, fall in the thickness with the increased pressure. The refractive indices were also obtained from the Swanpole envelope method for all thin films deposited at different oxygen pressures. The refractive indices of the films were found to be in the range from 1.95 - 2.04 at 488 nm wavelength with a rise in O_2 pressure. This slight increase in refractive index with increasing oxygen pressure was attributed to the densification and improvement in crystallinity of the

films, and it also correlated with XRD results too. A similar trend was documented in the literature[176].

3.4.6 OA *Z*-scan spectra of PLD BTO thin films

The OA *Z*-scan spectra of all the films are shown in Figure 3-18 (a) - (e). All these films showed RSA [129].

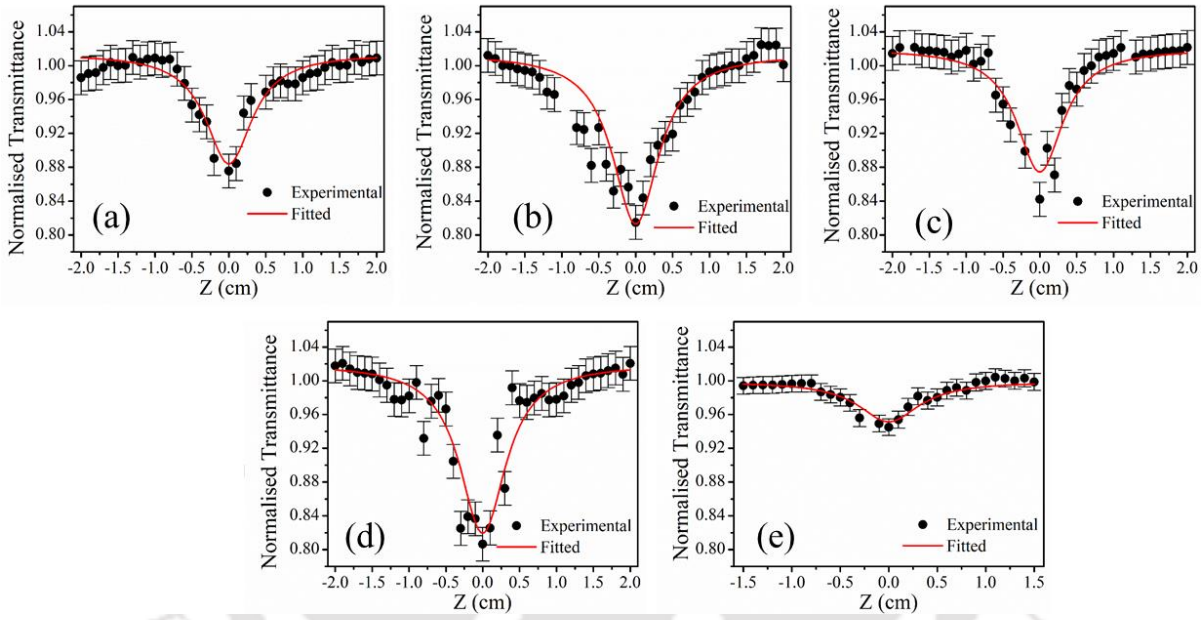

Figure 3-18 *OA Z-scan traces of the BTO thin films different oxygen pressures (a) 0.005, (b) 0.05, (c) 0.1, (d) 0.5, and (e) 1 mbar. The solid line depicts the theoretical fit.*

Table 3-6 *Values of α and β for the BTO thin films deposited at a different oxygen pressures.*

Oxygen pressure (mbar)	L (nm)	L_{eff} (nm)	α (cm^{-1}) x 10^{-4} (λ = 488 nm)	β (cm/W)
0.005	231	214	6.31	52.93 ± 0.02
0.05	240	216	8.74	56.63 ± 0.04
0.1	256	236	5.22	57.54 ± 0.05
0.5	212	197	6.94	56.48 ± 0.03
1	162	149	10.4	46.52 ± 0.05

The linear and nonlinear absorption coefficients of all the films are listed in Table 3-6. The nonlinear absorption coefficient strongly depends on the crystalline quality of the film [179]. In the present work, it is demonstrated that the best crystalline quality and low RMS surface roughness were observed at an optimum O_2 pressure of 0.1 mbar and nonlinear absorption coefficient (β) is maximum at this optimum pressure (Figure 3-18). The present β value of the BTO thin films is much higher than that reported earlier in the literature via pulsed laser [36, 174, 183].

3.5 Conclusions

In this present chapter, attempt is made to obtain the optimum temperature and background gas pressure for the thin films of BTO via PLD for the enhanced NLO properties. The Rietveld refinement XRD and Raman spectroscopy revealed that the target has tetragonal crystal symmetry with the P_{4mm} space group. The substrate temperature and oxygen pressure dependence on microstructural, morphological, and optical properties of BTO thin films deposited by PLD on a quartz substrate and the silicon substrate was studied. FESEM images

and EDX analysis showed that morphological changes were consistent with structural analysis. The deposited films fabricated at T_s 400 and 500 °C were amorphous, while those fabricated at 600, 650, and 700 °C were polycrystalline with pseudocubic phase (according to structural properties). Films deposited at different oxygen pressure also possessed polycrystalline structures with dominating (110) orientation and pseudocubic phase. From Raman analysis, also verified the pseudocubic phase. UV-Visible-NIR transmission spectroscopy results indicated that all films have 75 - 85% optical transparency in the Visible to NIR region. The β values of BTO thin films deposited at different T_s and oxygen pressure (O_2) were estimated from the modified *Z*- scan technique using the cw Ar-Ion laser source ($\lambda = 488$ nm). The value of β was found to be increased with an increase in substrate temperature and it increased with an increase in oxygen pressure till 0.1 mbar and fell down for higher oxygen pressure. These observations concluded that the optimum substrate temperature was 700 °C and 0.1 mbar oxygen pressure for BTO films fabricated via PLD for the maximum optical nonlinear response.

Chapter 4 : Influence of Cu nano-layer on linear, nonlinear, and photoluminescence properties of $BaTiO_3$ thin films fabricated via PLD

In the previous Chapter 3, through a systematic variation of experimental parameters, the optimum growth conditions (substrate temperature 700 °C and background pressure 0.1 mbar) were identified for PLD deposited BTO thin film. At optimum condition, BTO film exhibited a smooth surface having value of RMS roughness of less than 5 nm, the maximum crystallite size (D =18 nm), and nonlinear absorption coefficient, β, (57.54 cm/W). The NLO properties can be further enhanced by embedding with metallic nanoparticles. Therefore, to enhance structural and the β value, Cu nano-layer was embedded on BTO thin films at the same optimized condition. This present chapter aimed to explore the impact of Cu nano-layer on structural, linear, nonlinear optical properties and PL properties of PLD deposited BTO thin film.

4.1 Experimental details

The PLD technique was adopted in the present case to deposit three different configurations, BTO1, BTO2, and BTO3 as shown in Figure 2-6. In the first configuration, BTO1, BTO film was directly deposited on the substrates. For the second configuration, BTO2, a thin nano-layer of Cu, was deposited first directly on the substrates, followed by a BTO thin film on top of it. In the third configuration, BTO3, first BTO thin film was deposited on the substrates similar to BTO1 and then nanostructured Cu thin film was deposited on top of BTO as shown in Figure 2-6, Chapter 2. The details of deposition parameters for BTO and nanostructured Cu thin layer infused BTO thin films are listed in Table 2-3, Chapter 2. All the

three film were subjected to XRD, Raman, FESEM and AFM characterization. The second configuration, BTO2, exhibited nearly threefold enhancement in β and therefore this configuration was further tested with the infused in BTO film thickness for further improvement in the NLO property. The absorption spectra were recorded for detecting the SPR peak. The linear absorption coefficient and the bandgap of the films were determined by UV-Visible-NIR spectroscopy. The modified *Z*-scan experiment was performed for the measurement of NLO absorption coefficients. PL measurement was performed to understand the defects and role of Cu nano-layer on BTO thin films.

4.2 Effect of Cu nanolayer on BTO thin films deposited for 15 minutes

4.2.1 XRD analysis

The XRD spectra of BTO1, BTO2, and BTO3 thin films are shown in Figure 4-1(a) - (c), respectively. All these confirm the presence of all the planes similar to that of the BTO pellet, Figure 3-2, but the absence of the (002) plane indicates that films are in the cubic phase (PDF card No.: 01-084-9618), having a $P_{m\text{-}3m}$ space group.

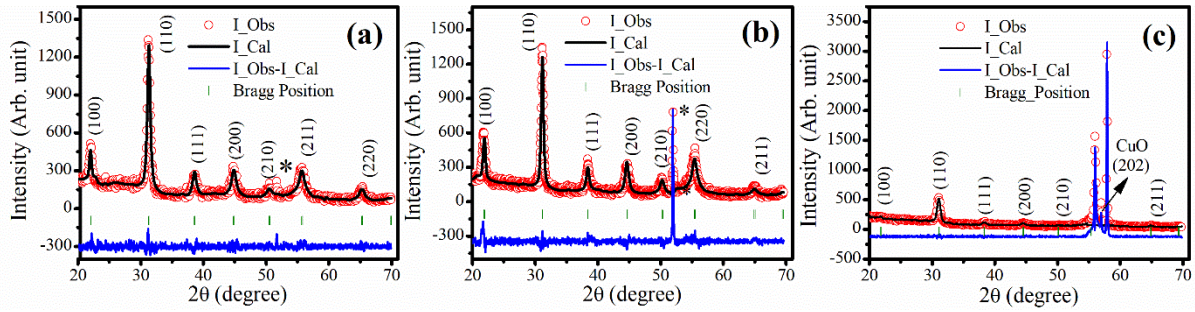

Figure 4-1 *Rietveld refined XRD spectra of (a) BTO1, (b) BTO2, and (c) BTO3 thin films. The peak marked (*) corresponds to crystalline silicon substrate (100).*

The tetragonal splitting of the planes is not resolved within detectability limits due to the overlapping of the peaks in the thin films. Moreover, it is also reported that if the crystallite size of BTO thin films is less than 20 nm, then the tetragonal phase could not be identified via

XRD [154]. The peak corresponding to the (110) plane was dominating one, indicating a preferred (110) plane having a cubic phase. The presence of Cu peak was not detectable in the BTO2 thin film as it was covered by BTO on top of it. In the BTO3, there was a weak appearance at 57.2º of the CuO (202) peak, Figure 4-1(c) [184]. The average crystallite size (D) of the films was determined from the FWHM of the peaks using the Scherrer formula in equation (3.1) and is listed in Table 4-1. The strain (ε) developed in the thin films was calculated from equation (3.3). The strain was calculated for all the thin films and listed in Table 4-1.

Table 4-1 *Values of a, b, c, D, unit cell volume, cell density and strain of films deposited on Si substrate.*

Thin Film	**BTO1**	**BTO2**	**BTO3**
Phase	Cubic	Cubic	Cubic
$a = b = c$ (Å)	4.04	4.06	4.07
Crystallite Size (D) (nm)	17	13	11
Cell volume (V) (Å)^3	66.02	66.82	67.47
Cell density (gm/cm^3)	5.87	5.78	5.74
$\varepsilon \times 10^{-3}$	2.48	7.44	9.92

From Table 4-1, it was observed that the lattice parameters of thin films were larger than that of the BTO pellet, which corresponds to the tensile strain. The positive values further confirm that the crystallites were in the state of tensile strain. The lattice parameter for Si

substrate (a_s) is 5.43 Å. Thus, the thin film experiences tensile strain due to positive lattice mismatch in between thin film and Si substrate. The lattice mismatch, *f*, is described by: $f = \frac{a_s - a_f}{a_s}$ where a_s is lattice parameter of the substrate [46]. A positive *f* value is an indication of tensile strain, and that of negative value corresponds to compression. In addition, for BTO2 and BTO3 thin films, the slightly increased lattice parameter (as compared to BTO1) was accounted due to the substitution of Cu. The substituent ion replaces A-site, or B-site ion is determined by the charge (q) and ionic radius (r) of the substituent ion. The ionic radius of Cu^{2+} is, r_{Cu} = 0.73 Å and is much smaller than the ionic radius of Ba^{2+} ions with r_{Ba}= 1.35 Å, but is comparable to that of Ti^{4+} ions (r_{Ti} = 0.60 Å). As a consequence, in an equilibrium state, Cu^{2+} ions will preferentially substitute Ti^{4+} sites, which results in a tensile strain in these thin films [185].

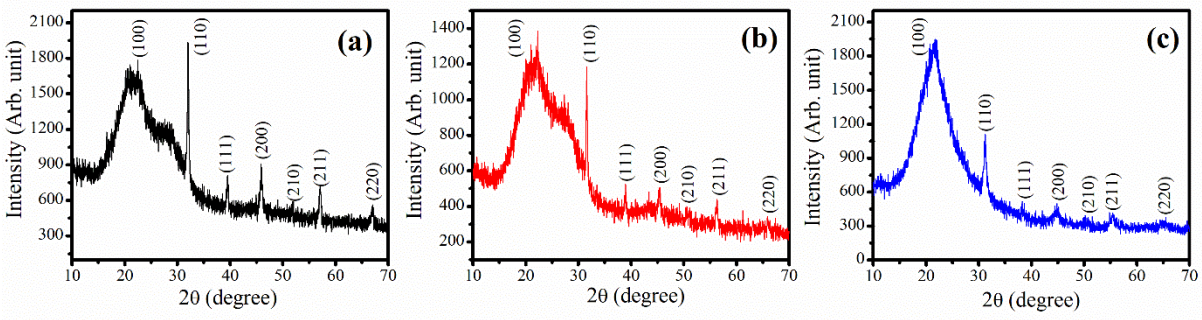

Figure 4-2 *XRD spectra of (a) BTO1, (b) BTO2, and (c) BTO3 thin films deposited on a quartz substrate.*

The XRD spectra of films deposited on a quartz substrate are shown in Figure 4-2 (a)-(c). These results indicate that the XRD spectra are noisy compared to that of thin films deposited on Si (100) substrate because of the amorphous nature of quartz substrate. There is a broad peak in the range of 10 º to 35 º due to the quartz substrate. The preferred orientation in these thin films is (110) plane too. The crystallite size was calculated using the Scherrer

formula, equation (3.1). The crystallite size was measured to be 16, 12, and 10 nm for BTO1, BTO2, and BTO3 thin films, respectively. The value of *D* decreases with the addition of Cu nano-layer in BTO2 and BTO3 thin films because of the substitute of Cu^{2+} in place of Ti^{4+} in these films. This creates defects and disturbs the local ordering of the crystal structure, and as a result, it distorts the crystallinity of thin films [186].

4.2.2 Surface morphology via FESEM analysis

Figure 4-3 (a) - (c) and (d) – (f) display the FESEM and corresponding cross sectional FESEM images of BTO1, BTO2, and BTO3 thin films deposited on a quartz substrate, respectively.

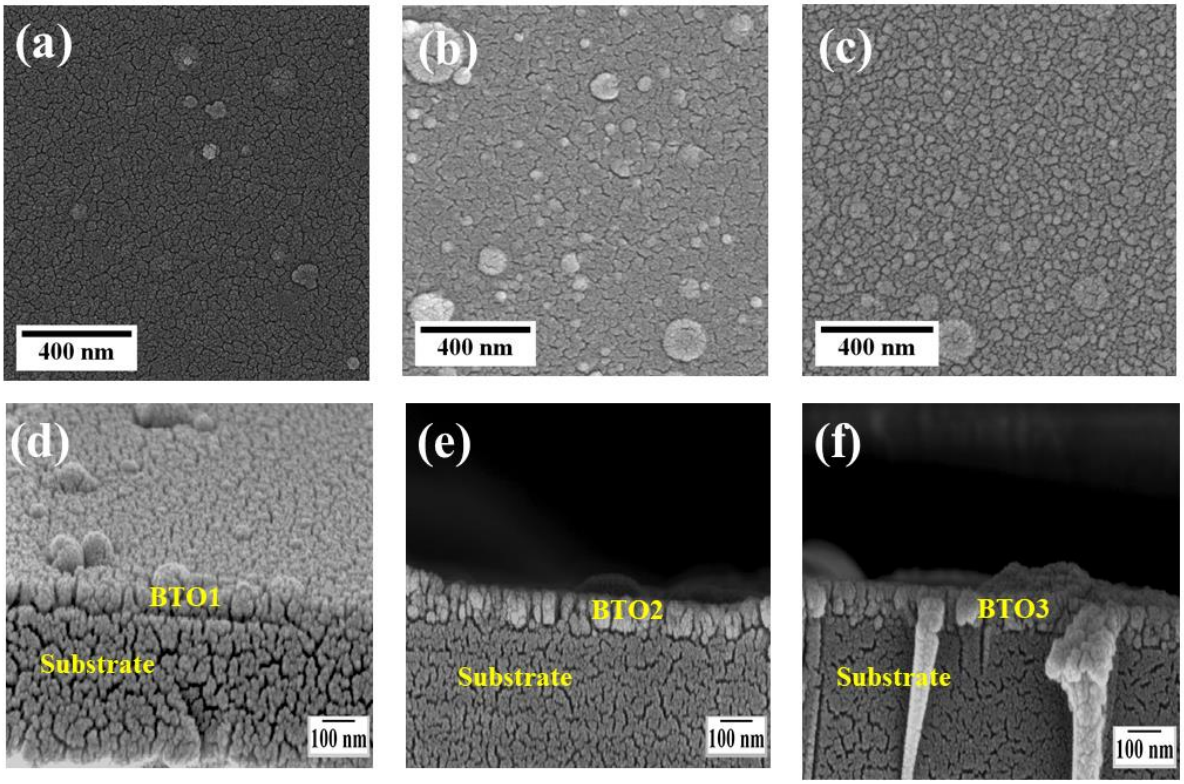

Figure 4-3 *FESEM images of (a) BTO1 (b) BTO2, (c) BTO3 thin films and cross-sectional FESEM images of (d)BTO1, (e) BTO2, and (f) BTO3 deposited on the quartz substrate.*

These images confirm a compact surface. From the cross-section view of FESEM, the overall thickness of the BTO1 thin film was found to be 63 ± 3 nm and that of for BTO2 and BTO3 was 72 ± 2 and 78 ± 4 nm, respectively. The thickness of the Cu layer was 5 ± 3 nm for the last two samples. The overall thicknesses were further confirmed via Profilometer measurement and listed in Table 4-2, indicating good agreement with each other.

Table 4-2 *Comparison of thickness of thin films from cross-sectional FESEM images and Profilometer measurement.*

Thin Film	Thickness (nm) (FESEM)	Thickness (nm) (Profilometer)
BTO1	63± 3	56± 6
BTO2	72± 2	70±5
BTO3	78± 4	73±5

4.2.3 RMS roughness via AFM analysis

Two - dimensional (2D) AFM images of all the samples with the scan area of 2 µm × 2 µm are shown in Figure 4-4 (a) – (c).

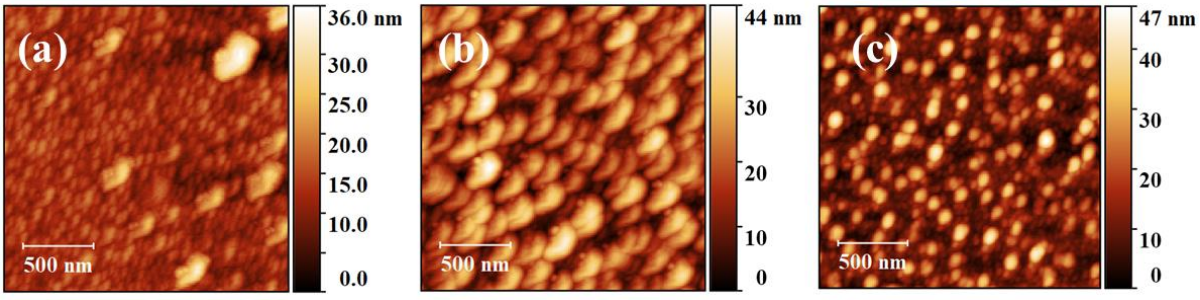

Figure 4-4 *AFM images for (a) BTO1, (b) BTO2, and (c) BTO3 thin films deposited on the quartz substrate.*

AFM images depict the similar morphological behavior for three different configurations, as observed from FESEM images (Figure 4-3).

The RMS surface roughness was found to be 3.98 ± 1.75 nm in the BTO1 sample, whereas it was 7.49 ± 0.91 and 7.74 ± 1.15 nm in BTO2 and BTO3 samples, respectively. Metal-nano layers at such small thickness are prone to form the local island, and hence, for the BTO3 sample being Cu on top results in the relatively large value of RMS surface roughness [187]. Similarly, a higher surface roughness value observed in BTO3 thin film is due to the growth of BTO thin film on top of the island Cu buffer layer. Similar behavior of metal-dielectric combination is reported in the literature [188].

4.2.4 Raman analysis of BTO1, BTO2, and BTO3 thin films

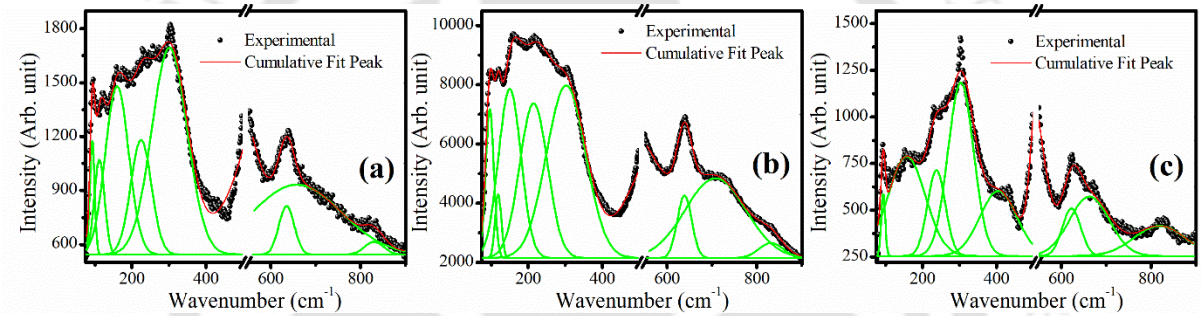

Figure 4-5 *Raman spectrum of (a) BTO1, (b) BTO2 and (c) BTO3 thin films grown on silicon substrate.*

Micro-Raman spectra recorded in the range of 75 to 900 cm^{-1} for the thin films deposited on Si (100) substrate are shown in Figure 4-5 (a) – (c). The Raman active vibrational modes of BTO identified in Figure 4-5 were observed to be around 160, 262, 303, 515, 635, 710, and 824 cm^{-1}. The 160 cm^{-1} bands correspond to the E (TO) / E (LO) / A_1 (LO) mode, while broadband at 262 cm^{-1} coincides with the A_1 (TO_2) mode. The [B1, E(TO+ LO)] mode at 303 cm^{-1} indicates tetragonal phase [60]. The third asymmetric A_1 (TO_3) mode at 515 cm^{-1} is likely to be overlapped with the Raman peak of the Si substrate at 521 cm^{-1}. The peak at 635 cm^{-1} is attributed to a surface optical mode of BTO. The mixture of A_1 (LO_3) and E (LO_3) mode at 710 cm^{-1} corresponds to a characteristic tetragonal peak of the BTO. One peak at 824 cm^{-1}

originates due to the presence of stress at the film-substrate interface [189]. The three modes at 262, 303, and 710 cm^{-1} were broad in BTO2 and BTO3 thin films. These are often attributed to second-order effects and are correlated with the disorder of Ti displacements in the octahedral. There was a red shift of Raman modes for BTO1 thin film compared to BTO bulk [156], and also a red shift of Raman spectra was observed in BTO2 and BTO3 thin films compared to BTO1 thin film. According to Gruneisen law: the change in Raman shift Δw is associated with the change in lattice constant Δa [190].

$$\Delta w = -3\gamma w_0 \frac{\Delta a}{a} \tag{4.1}$$

where w_0 and a are the Raman shift and the lattice constant of BTO, respectively, and γ is the Gruneisen parameter. Thus, the Raman shift of BTO2 and BTO3 films w.r.t BTO1 decreases, confirming tensile strain in these thin films which in agreement with XRD analysis, Figure 4-1. All these results indicate that all thin films were in the pseudocubic phase, which was in good agreement with XRD results. Figure 4-5 (b) further shows the five-fold enhancement of the Raman peak at 302 cm^{-1} in BTO2 thin film. This result is directly related to the SPR of the metal/dielectric interface [191].

4.2.5 Bandgap via UV-Vis-NIR spectra

The transmission spectra of all the samples deposited on quartz substrate are shown in Figure 4-6 (a) in the wavelength range of 200 - 2000 nm.

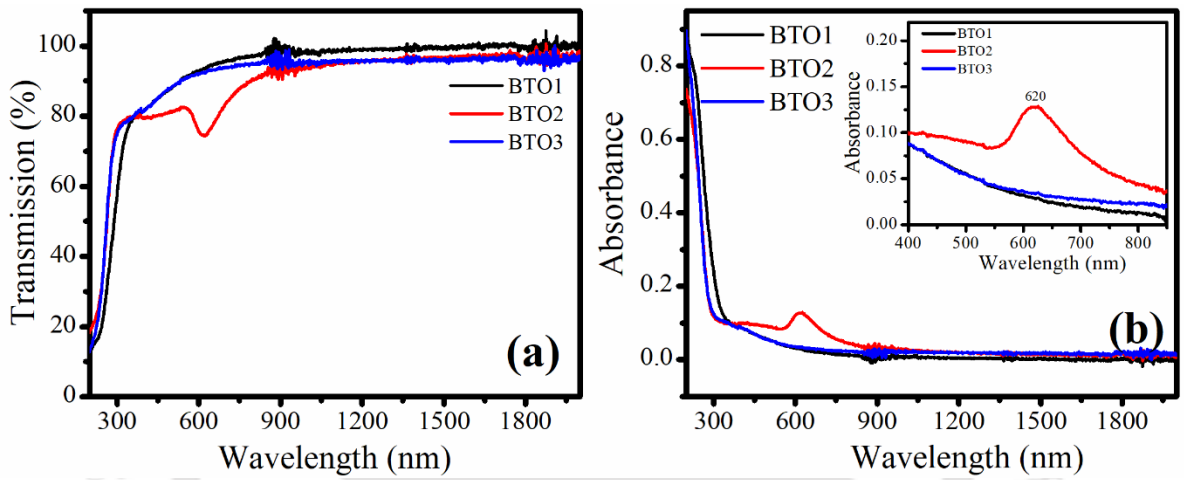

Figure 4-6 *(a) Transmission spectra (b) absorption spectra of BTO1, BTO2, and BTO3 thin films and the inset shows an expanded view of 620 nm SPR peak in the BTO2 thin film.*

All the thin films are highly transparent in the wavelength range of 800 - 2000 nm. The corresponding absorbance is shown in Figure 4-6 (b). The optical bandgap (E_g) and the absorption coefficient (α) are related to equation (2.7) [192]. The linear region of the $(\alpha h\nu)^{0.5}$ versus $h\nu$ curve (Tauc plot) is fitted to a straight line, and the intercept of this straight line gives E_g of the material of the thin. The Tauc plot is shown in Figure 4-7 for all the samples. The value of E_g was found to be (3.75 ± 0.11) eV for BTO1, (3.91 ± 0.05) eV for BTO2, and (3.93 ± 0.04) eV for BTO3 thin films indicating that the absorption edge shifted slightly towards the higher energy values with the infusion of Cu layer. The blue shift in the bandgap was attributed to the formation of tensile strain in BTO2 and BTO3 thin films, which results in bandgap broadening [193], which was in line with the XRD and Raman results. These bandgap values obtained are reasonbly close to those reported in the literature [46].

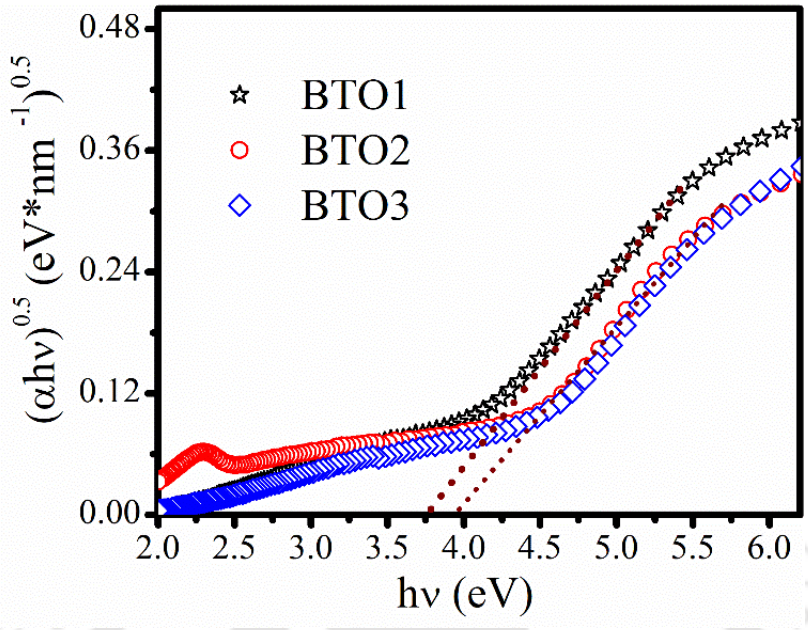

Figure 4-7 *Tauc plot for determining optical band gap (E_g) of all thin films deposited at T_s of 700°C.*

In the BTO2 film, a well-defined absorption peak around 620 nm, inset of Figure 4-6 corresponding to SPR due to the presence of Cu nanoparticles embedded directly into quartz substrate. On the contrary, no signature of SPR peak in the absorption spectra has been observed in BTO3 sample where Cu nano- layer was deposited on top of the BTO thin film. The resonant excitation of surface plasmons (SPs), can generally be achieved when electromagnetic modes are generated at interfaces between materials with the opposite sign of their dielectric permittivities (between a metal and a dielectric) [191]. Therefore, the SPR peak is present in the BTO2 film instead of the BTO3 film. A similar trend was observed in the literature for ZnO and Ag composite thin films [194].

4.2.6 Nonlinear optical study via modified Z-scan technique

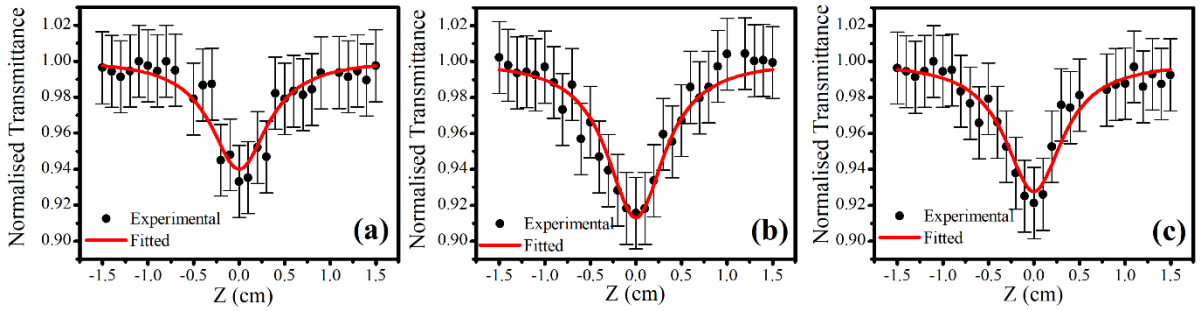

Figure 4-8 *OA Z-scan graphs of thin films (a) BTO1, (b) BTO2, and (c) BTO3 deposited on the quartz substrate.*

Figure 4-8 (a) – (c) shows the OA *Z*-scan spectra for all three samples, along with error bars. All the films exhibited RSA response [36]. The optical nonlinearity is due to two photon induced absorption as described in Chapter 3.

The two-photon absorption coefficient, β, estimated from equation (2.8) were found to be (2.24 ±0.51) cm/W for BTO1, (7.53±0.32) cm/W for BTO2, and (4.37±0.63) cm/W for BTO3 thin films. The observed nonlinear absorption in the latter two films was influenced by the intraband transition of conduction electrons in the presence of Cu nanoparticles. This transition occurs due to the collective dipole oscillations of the free electrons at metal-dielectric interfaces [13]. In this present work, when the cw laser beam is incident on the thin film containing Cu nanoparticles, part of the total thermal energy produced by the laser-induced heating is absorbed in the metallic nanoparticles. Some part of this absorbs energy promotes d-electrons in the vicinity of the X point of the first Brillouin zone to the conduction band, and the rest of the thermal energy is absorbed by the conduction electrons. Due to this thermal heating, there is a modification of the dielectric constant in the BTO matrix [195]. As a consequence, there is an enhancement in the values of the nonlinear absorption coefficient in BTO2 and BTO3 thin films. The larger enhancement of the optical nonlinearity of BTO2 thin

film compared to that of BTO3 was also accounted for by the local field factor near the SPR of Cu nanolayer [196]. This result was also corroborated with the absorption spectra of BTO2 thin film in Figure 4-6 (b).

4.2.7 Photoluminescence studies

Figure 4-9 shows the PL spectra of all the three configurations of BTO deposited on Si (100) at a substrate temperature of 700ºC, using the excitation wavelength of 355 nm (3.5 eV).

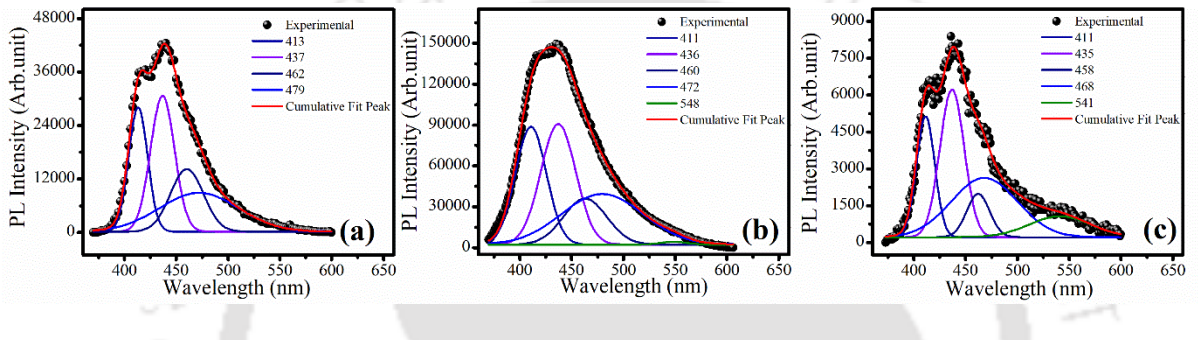

Figure 4-9 *Photoluminescence spectra of (a) BTO1, (b) BTO2, and (c) BTO3 thin films deposited on Si (100) substrate.*

The photoluminescent properties of thin films are believed to be attributed to the order/disorder in the crystal structure and by the electronic states within the bandgap due to atomic vacancies, defects, or impurities [60, 61]. In this present study, all the thin films have disorders in the crystal system and possess tensile strain. The direct combination of localized electron-hole pairs (self-trapped excitons) and defect states (impurities and O_2 vacancies) are two main reasons for PL emission in BTO thin films in visible spectra range [197]. The multiple peaks are visible in all three films. The deconvulated PL scheme is also shown in Figure 4-9. The thin film of BTO1 exhibits four peaks, whereas BTO2 and BTO3 show five peaks.

The film exhibited a strong violet emission centered at 413 nm (3.00 eV) in BTO1, 411 nm (3.02 eV) in BTO2, and BTO3, which are usually related to defect levels associated with

oxygen vacancies [198]. The excited electrons recombine with holes via defect levels and result in radiative transitions in the luminescence process. In the appearance of Cu nano-layer in BTO2 and BTO3 configuration, the 413 nm peak in BTO1 is blue-shifted to 411 nm. This blue shift of UV-PL in BTO2 and BTO3 is due to the size effect on the energy level of the confined excitons because of the presence of the Cu nanoparticles. It is a well-known fact that the crystallite size in perovskite thin films strongly influences the peak position due to the effect of quantum confinement on the energy bandgap [199]. With the addition of Cu nano-layer in BTO thin films, crystallite size decreases, Table 4-1, as a result, the PL peak is blue-shifted [200]. The violet emission peaks present at 437 nm (2.83 eV) in BTO1, 436 nm (2.84 eV) in BTO2, and 435 nm (2.85 eV) in BTO3 thin films. In addition, another blue emission peak at 462 nm (2.68 eV) and 460 nm (2.69 eV), 458 nm (2.70 eV) in all these three configurations is due to delocalized electronic levels nearer to the valence band and conduction band [198].

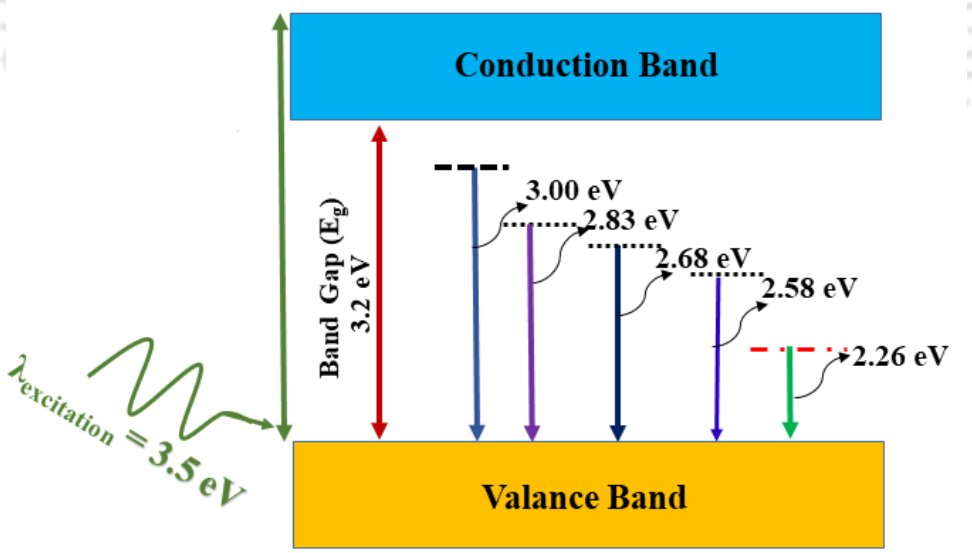

Figure 4-10 *Schematic energy level diagram of PL emission of BTO1, BTO2, and BTO3 thin films.*

The energy level diagram depicting the possible mechanism of the photoluminescence for bare BTO and in the presence of the Cu NP layer is illustrated in Figure 4-10.

The green emission PL peak centered at 548 nm (2.26 eV) was observed for BTO2, whereas it is blue-shifted to 541 nm (2.29 eV) in BTO3 film associated with band to band emission for Cu_2O or CuO [201].PL intensity is enhanced four-fold in the presence of the Cu nano-layer compared to that of pure BTO thin film due to local field enhancement in the BTO2 configuration. However, the PL intensity of BTO3 thin film is reduced compared to that of pristine BTO thin film. It is due to the presence of Cu, Cu_2O and CuO on the top of BTO [61]. These results are in good agreement with the previously reported results [202].

4.3 Effect of Cu nano-layer on BTO thin film deposited for 60 minutes

In Section 4.2, it was observed that β and the PL emission is enhanced more than three times in BTO2 configuration as compared to that of bare BTO film. Therefore, for further improvement BTO2 configuration, BTO2_1 thin film was deposited for 60 minutes duration by keeping all the deposition parameters the same as BTO2 thin film and for comparison a bare BTO thin film was also deposited for 60 minutes. The deposition parameters of these two films have already been listed in Table 2-3.

4.3.1 FESEM analysis of Cu nano-layer on BTO thin film deposited for 60 minutes (BTO2_1)

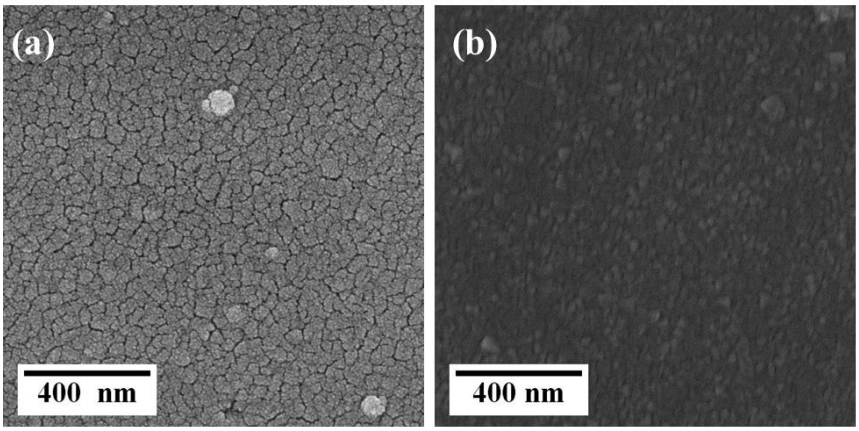

Figure 4-11 *FESEM micrographs of (a) BTO (b) BTO2_1 thin films deposited on the quartz substrate.*

Figure 4-11 (a) - (b) shows the FESEM micrographs for BTO and BTO2_1 thin films deposited on the quartz substrate for 60 minutes, respectively. It was evident from Figure 4-11(a), the thin film was compact, and grains were uniformly distributed having arbitrary shape. With the addition of Cu nano-layer on the BTO host matrix, the thin film exhibited different morphology than BTO thin film. The grains are approximately spherical in shape. The thickness of these two thin films was determined from cross-sectional FESEM images and the Profilometer and tabulated in Table 4-3.

Table 4-3 *Thickness measurement of thin films from cross-sectional FESEM images and Profilometer.*

Thin Film	***L* (nm) (FESEM)**	***L* (nm) (Profilometer)**
BTO	256 ± 4	250 ± 6
BTO2_1	270 ± 3	270 ± 7

4.3.2 XRD Analysis

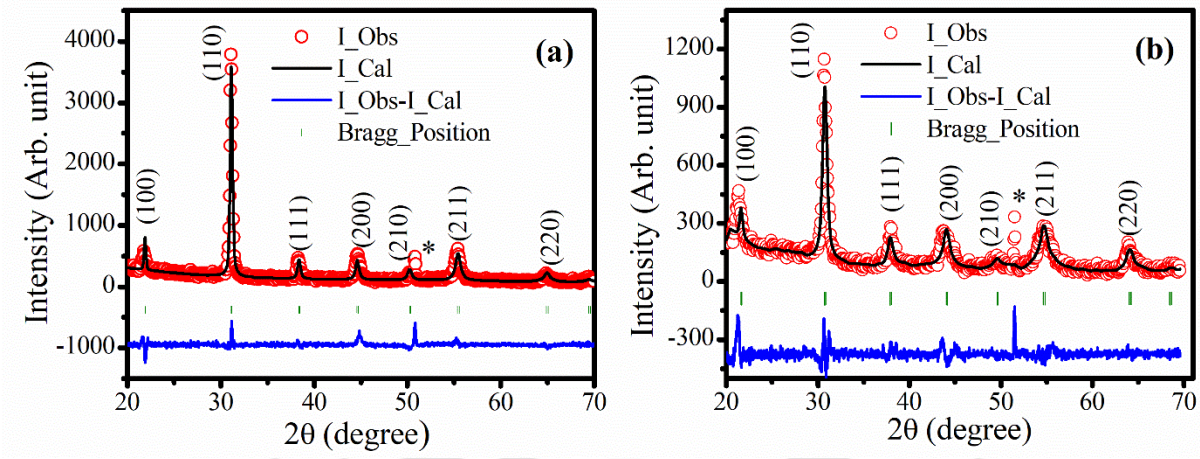

Figure 4-12 *Reitveld refined XRD spectra of (a) BTO (b) BTO2_1 thin films deposited on Si substrate. The peak marked (*) is due to the crystalline silicon substrate.*

Figure 4-12 (a) - (b) illustrates Reitveld refined XRD patterns of BTO and BTO2_1 thin films deposited on the silicon substrate. The diffraction pattern in the range of 2θ from 40º to 50º is usually characteristic of the presence of either cubic or tetragonal BTO structure. In this present case, all the diffraction peaks were present, similar to those of BTO1, BTO2, and BTO3 thin films. In this case also splitting of (200) plane into tetragonal (200) and (002) splitting at about 45º not were observed, confirming the presence of pseudocubic phase in both the thin films. The extracted parameters from refinements are listed in Table 4-4.

The lattice parameter of BTO2_1 film was increased with the addition of Cu nano-layer, whereas the density of the thin film decreased. The crystallite size of the thin film was calculated using the Scherrer formula in equation (3.1) and found to be reduced from 18 to 16 nm. The shift in diffraction peak (110) position towards the lower Bragg angle was attributed to the lattice expansion. The same analogy can be considered to explain the increased lattice parameter values in the BTO2_1 thin film, discussed in Section 4.2.1. The value of ε of BTO

and BTO2_1 films is tabulated in Table 4-4 and found to be higher than BTO1 and BTO2 thin films due to increase in thickness of thin films.

Table 4-4 *Determination of phase, a, b, c, D, V, cell density, and strain (ε) of thin films.*

Thin Film	BTO	BTO2_1
Phase	Cubic	Cubic
$a = b = c$ (Å)	4.05	4.08
Crystallite size (D) (nm)	18	16
Cell volume (V) $(Å)^3$	66.13	68.94
Cell density (gm/cm^3)	5.79	5.62
$\varepsilon \times 10^{-3}$	4.96	12.41

4.3.3 Raman analysis of BTO2_1 thin film

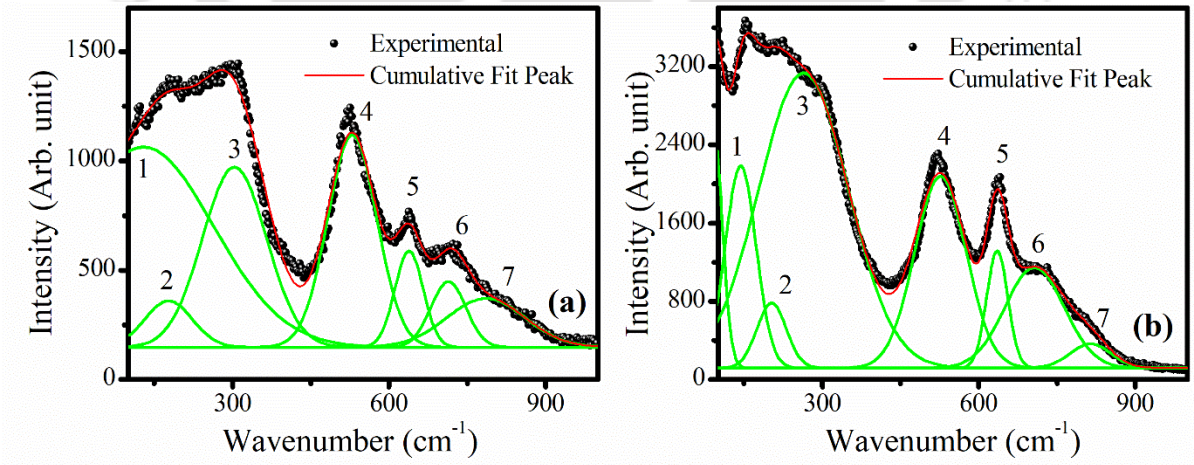

Figure 4-13 *De-convoluted Raman spectra of (a) BTO and (b) BTO2_1 thin films deposited on the quartz substrate.*

Figure 4-13 shows the RT Raman spectra of BTO and Cu nano-layer embedded BTO thin film (BTO2_1) recorded in the wavenumber range of 100 – 1000 cm^{-1} along with reflection de-convolution, which were fitted to the Gaussian function. Seven Raman active modes were observed, similar to those mentioned in previous Section 4.2.4 for BTO1 and BTO2 thin films. The sharpness of 304 cm^{-1} peaks was reduced and appeared as shoulder in these thin films indicating that the tetragonal phase was not also dominant here and suggested the pseudocubic phase, which agrees with XRD results, Figure 4-12. The all the Raman modes of thin films are listed in Table 4-5. The Raman modes were blue-shifted in comparison to BTO1 thin film on account of presence of tensile strain in BTO and BTO2_1 thin films.

Table 4-5 *Mode assignment and Raman shifts of BTO and BTO2_1 thin films.*

Modes	Mode assign	BTO	BTO2_1
		Raman shift (cm^{-1})	**Raman shift (cm^{-1})**
1	E(TO)/E(LO)/A_1(LO)	129	111
2	$A_1(TO_2)$	185	175
3	[B_1+E(TO+LO)]	304	300
4	$A_1(TO_2)$	529	526
5	A_1(LO)/E(LO)	638	635
6	$A_1(LO_3)$, $E(LO_3)$	714	706
7	-	815	785

4.3.4 UV-Vis-NIR transmission spectra of BTO and BTO2_1 thin films

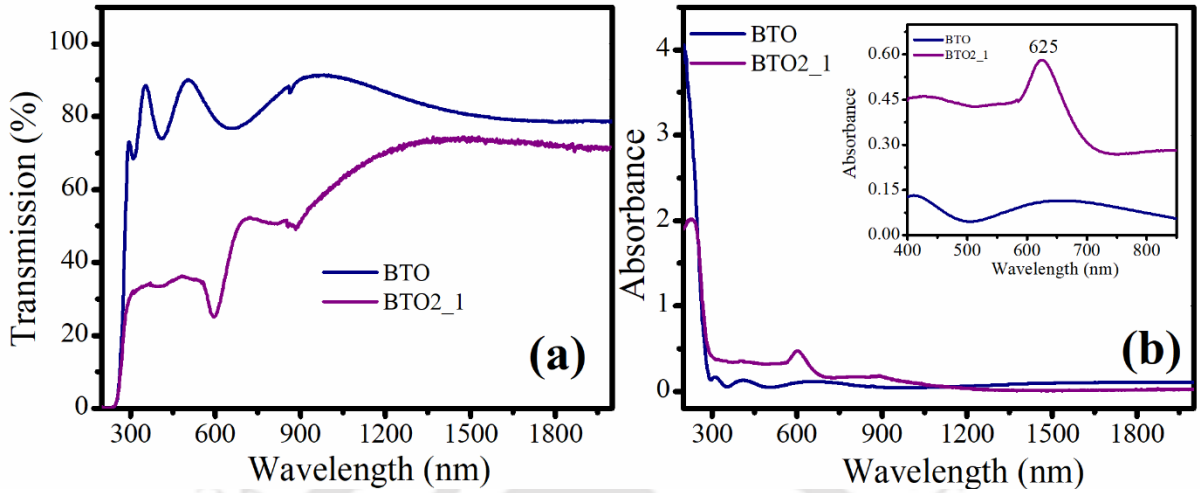

Figure 4-14 *(a) UV-Visible NIR transmission spectra (b) absorption spectra and the inset shows the SPR peak of BTO2_1 thin film around 625 nm.*

Figure 4-14 (a) shows the UV-Vis-NIR transmission spectra of BTO and BTO2_1 films deposited on a quartz substrate in the 200 – 2000 nm wavelength range. The BTO thin film deposited for 60 minutes was transparent and exhibited optical transmittance of more than 70 %. The SPR peak was noticed at around 625 nm in the BTO2_1 film. The transmittance of the film got declined to 40-60 % by adding Cu nano-layer on BTO thin film in the visible region due to the absorption of light in the form of SPR in BTO2_1 thin film. The SPR peak intensity increased with increase in the thickness of BTO thin film, which can be explained through the well-known Mie theory[203].

$$\alpha = \frac{18\pi}{\lambda} n_d^3 V_m \frac{\varepsilon_{m2}}{(\varepsilon_{m1} + 2n_d^2)^2 + \varepsilon_{m2}^2} \qquad (4.2)$$

where α is optical absorption coefficient, V_m, n_d, λ, ε_{m1} and ε_{m2} are volume fraction of metal, the refractive index of the dielectric, wavelength as well as real and imaginary part for the dielectric constant of the metal, respectively. As SPR depends on all these parameters, the primary two factors affect the intensity and broadening of SPR peak. Firstly, the refractive

index of the BTO dielectric matrix which affects the SPR peak intensity. Secondly, when BTO matrix thickness increases, as a result, the inter-particle separations reduce. At smaller inter-particle separations, coupling of charge oscillations between the particles becomes significant, giving rise to broadening and red shift of SPR absorption peak [194]. The increase in the dipolar coupling between Cu nanoparticles with decreasing particle spacing, which would likely provide an additional absorption on the long-wavelength side of the spectrum and broaden the optical response [204, 205]. The SPR peak redshifted from 620 to 625 nm with the increasing average dielectric constant of the surroundings due to the higher average dielectric constant of BTO and quartz substrate. Figure 4-15 represents the Tauc plot for BTO and BTO2_1 thin films.

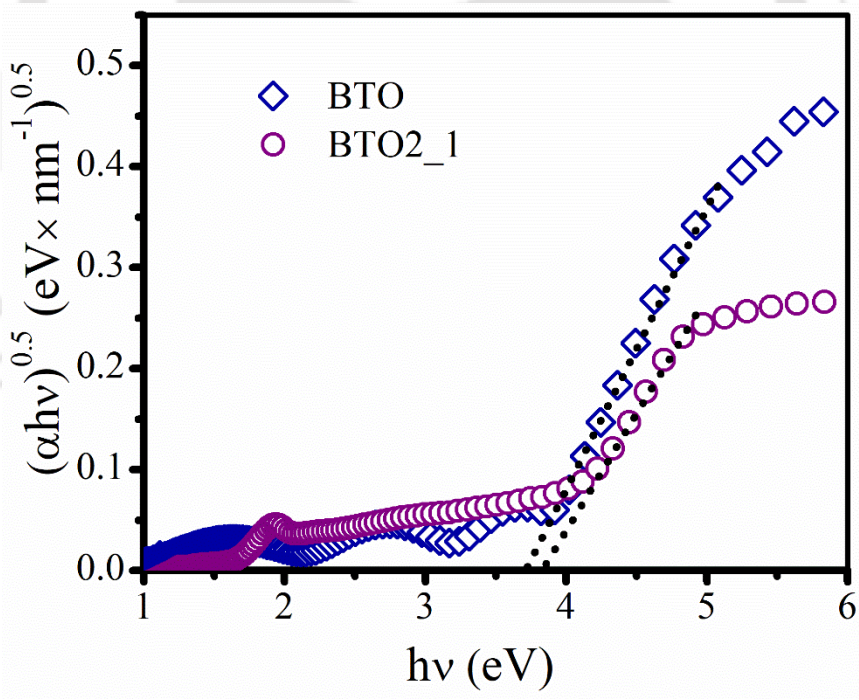

Figure 4-15 *Tauc plot for BTO and BTO2_1 thin films deposited at 700°C on quartz substrate.*

The value E_g was found to be (3.70 ± 0.05), and (3.82 ± 0.03) eV for BTO and BTO2_1 thin films. The absorption edge of BTO2_1 shifted towards the higher energy values due to the

infusion of Cu nano-layer. The formation of tensile strain in the BTO2_1 thin film results in bandgap broadening, therefore, there is a blue shift in the bandgap as compared to bare BTO thin film. The obtained values were in good agreement with the reported optical indirect band gap values [46, 51].

4.3.5 OA Z-scan of BTO2_1 sample

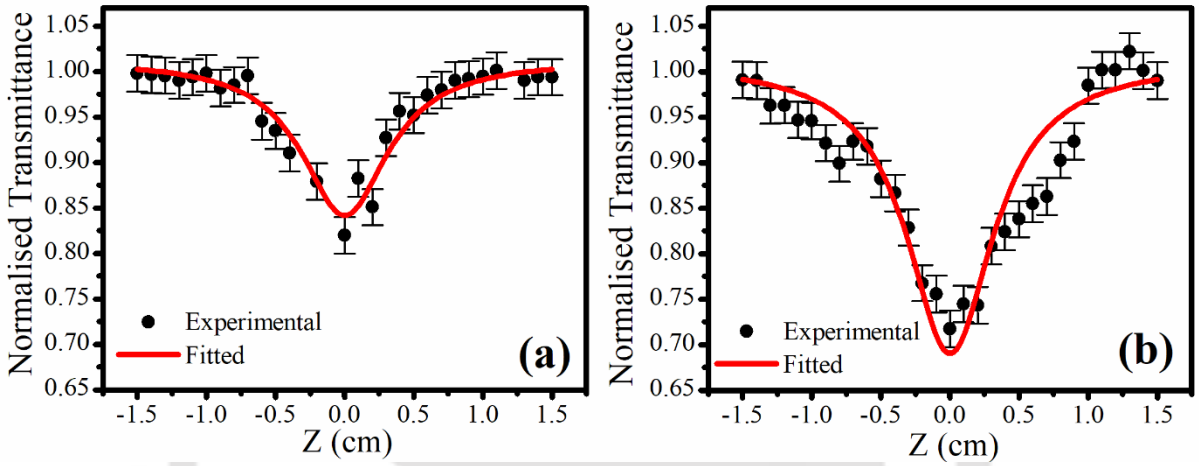

Figure 4-16 *OA Z-scan normalized transmittance curve of PLD deposited (a) BTO and (b) BTO2_1 thin films grown on the quartz substrate.*

Figure 4-16 (a) - (b) depicts the normalized transmittance plot for OA Z-scan as a function of the sample position (z) for BTO and BTO2_1 thin films, respectively deposited for 60 minutes. The two films exhibited transmittance minima at the focus, indicating RSA. In the present case, nonlinearity was caused by TPA. The OA Z-scan spectra were fitted using equation (2.8), Chapter 2. Horowitz et al. and Zhang et al. found that TPA can occur in BTO thin films due to the existence of intermediate energy levels inside the forbidden gap (because of impurities) [36, 206]. The β value was calculated using equation (2.8) and found to be (57.54 ± 0.05) and (155.04 ± 5.39) cm/W, respectively. The three-fold enhanced β value could be attributed due to two reasons. Firstly, collective dipole oscillations increased near metal/dielectric interfaces due to SPR as discussed in Section 4.3.4. Secondly, the laser light

absorbed more when the beam propagates through the film, giving more local heating in the BTO2_1 thin film having larger thickness compared to that of BTO2 thin film and accounted for thermally induced nonlinearity.

4.3.6 Photoluminescence studies

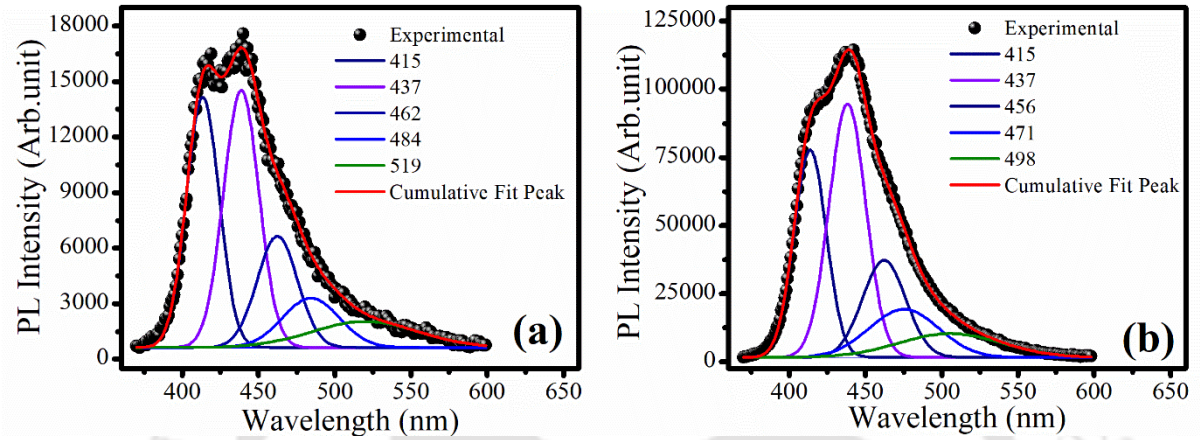

Figure 4-17 *PL spectra of (a) BTO and (b) BTO2_1 thin films on Si substrate.*

Figure 4-17 (a) - (b) shows the de-convoluted PL spectra of BTO and BTO2_1 thin films deposited on Si (100) substrate. Both the thin films displayed broadband in the visible spectrum, with maximum emission at ~ 437 nm (2.84 eV). De-convolution of PL spectrum resulted in broad violet luminescence at ~ 415 nm (2.98 eV) and ~ 437 nm (2.84 eV) for both films. Another two blue bands were observed at ~ 462 nm (2.68 eV) and ~ 484 nm (2.56 eV) in BTO thin film. The peak positions of blue band showed a slight blue shift towards higher energy by ~ 0.04 eV and ~ 0.07 eV with the infusion of Cu nano-layer to BTO dielectric matrix. Furthermore, weak shoulders can be seen around the green band having peak around ~ 519 nm (2.38 eV) in BTO and ~ 498 nm (2.48 eV) in BTO2_1 thin film. This slight blue shift was due to the increased thickness and decreased crystallite size in BTO film, similar to that of BTO2 thin film discussed in Section 4.2.7. The green luminescence was associated with the recombination of self-trapped excitons that formed localized states in the forbidden gap, as

shown in Figure 4-17. The enhancement of PL intensity in BTO2_1 as compared to that of BTO accounted for localized fields due to plasmon excitation. According to Mie theory, localized electric fields mainly lie in the vicinity of the metallic surface because of the plasmonic skin depth effect; therefore, the surface layer of metal and the surrounding medium is crucial for PL enhancement.

4.4 Conclusions

The PLD technique was used to fabricate polycrystalline thin films in three configurations: bare BTO, sandwiched Cu nano-layer between substrate and BTO, and finally Cu nano-layer on top of BTO, BTO1, BTO2, and BTO3 samples, respectively. Structural properties confirm that the deposited films are in the pseudocubic phase. Raman intensity of BTO2 film is five times higher than that of the bare BTO film. The SPR peak was observed at 620 nm in BTO2 thin film and that of 625 nm in BTO2_1 thin film. The β value was (7.53± 0.32) cm/W in BTO2 thin film, which was higher than the other two configurations. With the increase in thickness to 256 nm for the BTO2_1 thin film, the β value increased drastically to (155.04 ± 5.39) cm/W. The enhancement of the PL intensity was observed for BTO2 and BTO2_1 thin films compared to pristine BTO1 and BTO thin films, respectively.

Chapter 5 : Influence of Cu nano-layer on linear and nonlinear optical properties of $SrTiO_3$ thin films

Strontium titanate ($SrTiO_3$, STO) is another member of the oxide perovskite family similar to BTO and good candidate for nonlinear optical properties. In this present chapter, effect of infusion of Cu nano-layer on the linear and nonlinear optical properties of PLD deposited STO thin films is reported.

The enhancement in Raman and PL intensity as well as the β value were observed to be enhanced due to addition of Cu nano-layer as reported in the previous Chapter 4. Therefore, to study the SPR and nonlinear optical properties of Cu nano-layer embedded STO films, the experiment described in Chapter 4 was repeated by replacing BTO with STO. In this chapter, the structural, linear, and nonlinear optical properties of pure and metal nanocomposites of STO thin films fabricated via PLD on the quartz substrate were investigated. Further, its structural and morphological properties were correlated with the linear and nonlinear optical properties of the films.

5.1 Experimental details

Preparation of STO targets and fabrication process of STO thin films via PLD have been already discussed in Section 2.1 and Section 2.3, Chapter 2. The deposition parameters for fabrication of pure STO and Cu nano-layer sandwiched STO thin films have also already been listed in Table 2-4, Chapter 2 and same as that of for BTO thin films of Chapter 4. In this present chapter, three geometrical configurations viz; pure STO, Cu-STO (STO2_1), and STO-Cu (STO3_1) thin films were grown onto quartz substrate via PLD technique. The morphology

and topography of the thin films were unveiled using FESEM and AFM analysis. The determination of crystallite size and phase were studied by an XRD spectrometer. Raman spectroscopy was used to determine the phase and vibrational modes of STO and its nanocomposite thin films. The linear absorption coefficient and refractive index were measured over the wavelength range of 200 - 2000 nm by recording UV- Visible-NIR spectra. The third-order nonlinear optical properties of the films were determined by an in-house assembled single-beam *Z*-scan technique using a cw Ar-Ion laser at a wavelength of 488 nm as detailed in Section 2.4.8, Chapter 2.

5.2 Effect of Cu nanolayer on STO thin films via PLD

5.2.1 Surface morphology of STO thin films

Figure 5-1 (a) - (c) presents 2D AFM micrographs of pure STO and Cu infused thin films deposited on quartz substrate along with the height profile of the corresponding AFM images. The scan area of each micrograph is 2 × 2 μm^2.

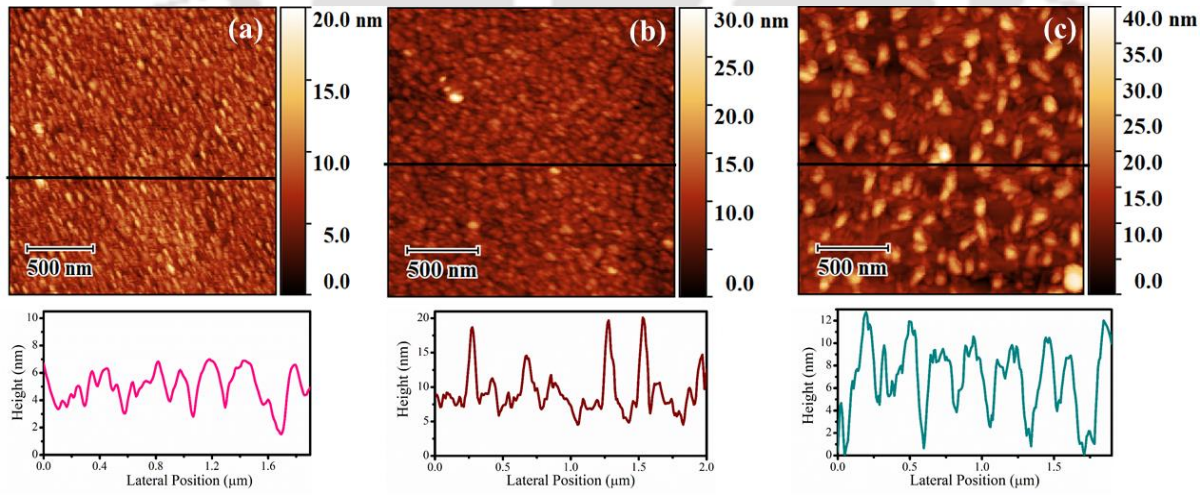

Figure 5-1 *AFM images (2 × 2 μm^2) of (a) STO, (b) STO2_1, and (c) STO3_1 thin films grown on the quartz substrates. The bottom of each figure shows the height profile of the line drawn across the corresponding AFM images.*

The RMS surface roughness of all samples was determined from the AFM images. It was found to be 1.94 ± 1.71 nm for pure STO thin film. The RMS roughness increased to 4.57 ± 1.05 nm for STO2_1, and that of for STO3_1 thin film, 5.08 ± 1.35 nm. The RMS roughness of STO thin films was lower than that of BTO films described in Section 3.3.1. This result was similar to that of reported in literature [187, 207].

Figure 5-2 (a) – (c) displays the FESEM images of STO, STO2_1, and STO3_1 thin films grown on quartz substrate at a substrate temperature of 700 ºC. A uniform and continuous growth of islands of irregular shape can be seen in all the three samples.

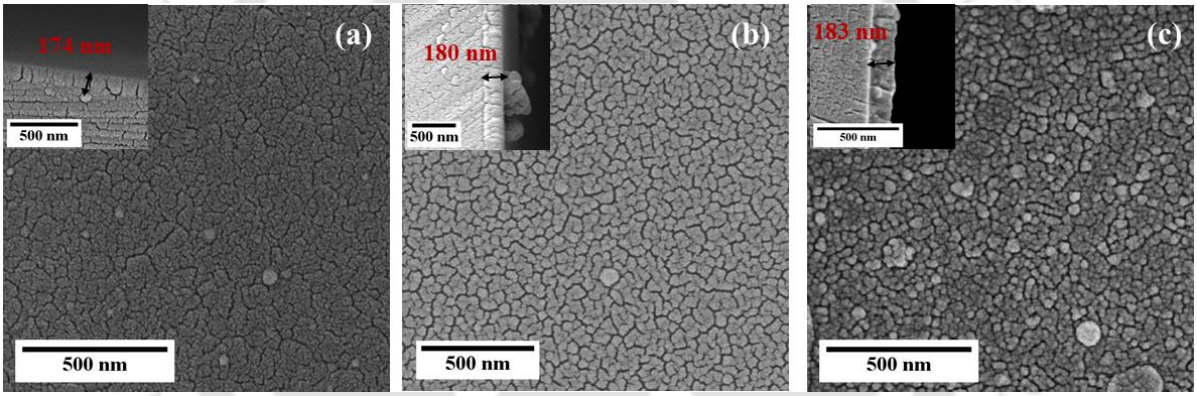

Figure 5-2 *FESEM images of (a) STO, (b) STO2_1, and (c) STO3_1 thin films grown on the quartz substrates and the inset shows the cross-sectional images of respective thin films.*

The cross-sectional images of all three thin films are shown in their respective FESEM images of Figure 5-2 to assess the overall thickness of thin films. The thickness was also measured via Profilometer measurement and both the observations are listed in Table 5-1. The thickness obtained from the two measurements was in good agreement with each other. The thickness of pure STO and Cu thin layer composite thin films have less thickness compared to that of BTO thin films. This is probably laser ablation more rapid in BTO target than that of STO under the same deposition conditions.

Table 5-1 *Thickness assessment of all samples from cross-sectional FESEM images and Profilometer.*

Sample	Thickness (nm) (FESEM)	Thickness (nm) (Profilometer)
STO	174 ± 3	170 ± 4
STO2_1	180 ± 4	182 ± 3
STO3_1	183 ± 5	184 ± 4

5.2.2 XRD and Raman spectra of STO, STO2_1 and STO3_1 thin films

The structural studies of all the three samples of STO were investigated via XRD with Cu: $K_{\alpha 1}$ radiation having a wavelength of 1.5406 Å and in the 2θ range of 10° to 70° and are shown in Figure 5-3.

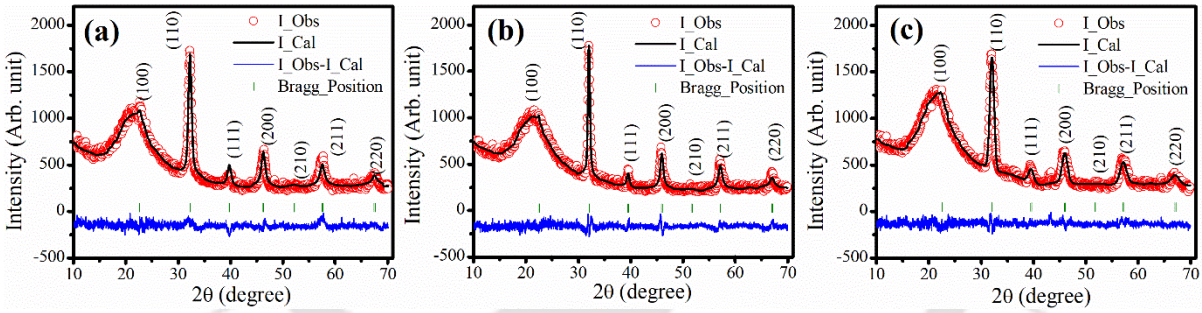

Figure 5-3 *XRD Reitveld refined spectra (a) STO, (b) STO2_1, and (c) STO3_1 thin films deposited on the quartz substrate.*

From Reitveld analysis, it was found that all the three samples are of cubic structures. The XRD peaks corresponding to (100), (110), (111), (200), (210), (211), and (220) crystal planes belong to the cubic phase of STO (ICSD collection code: 56092). The broader peak from 10º to 30º is from the quartz substrate [67]. It was found that all the samples were polycrystalline, comprising a strong reflection along the (110) plane. The average crystallite size (D) was calculated from the Debye Scherer formula, equation (3.1) and are listed in Table 5-2.

Table 5-2 *Determined Phase, lattice parameters, crystallite size, cell volume, cell density, strain of all thin films from Reitveld analysis.*

Sample	Phase	$a = b = c$ (Å)	Crystallite size (D) (nm)	Cell volume (V) (Å)^3	Cell density (gm/cm^3)	Strain (ε) x 10^{-3}
STO	Cubic	3.92	13	60.43	5.04	2.55
STO2_1	Cubic	3.95	11	61.65	4.96	7.67
STO3_1	Cubic	3.95	10	61.68	4.94	7.67

The lattice parameters, crystallite size, cell volume, cell density were determined from Reitveld analysis and the strain developed in the thin films was calculated using equation (3.3) and are listed in Table 5-2. It was observed that the lattice parameters of the thin films increased slightly in the presence of Cu nano-layer in STO thin films (Table 5-2). The similar observations were reported in the literature [208]. The strain in STO2_1 and STO3_1 thin films has increased nearly threefold in the presence of Cu layer. The substitution of Cu^{2+} ions in place of Ti^{4+} in these films, create defects and disturbs the local ordering of the crystal structure, and as a result, it distorts the crystallinity of thin films and increases the strain [186].

Figure 5-4 shows RT Raman spectra in the range of 100 – 900 cm^{-1} for all the three samples of STO. The Raman spectra consists of multiple peaks; hence it is de-convoluted. XRD analysis revealed that present STO thin films were in cubic symmetry with $P_{m\text{-}3m}$ space group and corresponding phonons are represented by $3F_{1u} + F_{2u}$ [209]. According to cubic crystal symmetry, the optical phonons of STO are Raman inactive. But, these phonons can appear in Raman measurements if the thin films deviate from cubic symmetry due to possible strain or oxygen vacancies [210, 211].

From the deconvolution spectra assigned in Figure 5-4, the optical phonon modes were identified and are listed in Table 5-3 for all the three configurations; STO, STO2_1, and STO3_1.

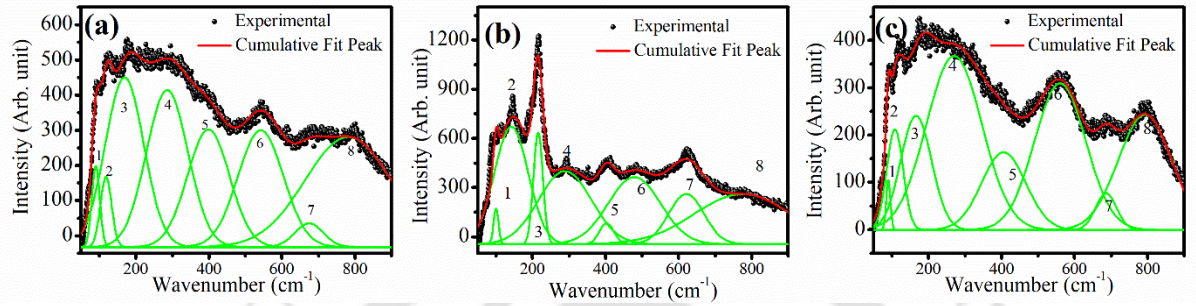

Figure 5-4 *Raman spectrum of (a) STO, (b) STO2_1, and (c) STO3_1 thin films grown on the quartz substrate.*

The Raman spectra of the STO thin films, second-order peaks identified at 89,118,174, 275,420, 541, and 795 cm^{-1} are associated with TO_1, A_1 (TO_2), (LO_1+ TO_2), TO_3, LO_3, TO_4 and LO_4 phonon modes, respectively [212]. These modes correspond to the bands at 174 cm^{-1} (O–Sr–O) stretching mode, 275 cm^{-1} (O–Sr–O) bending mode, 541 cm^{-1} (Ti–O–Ti) bending mode, and the 795 cm^{-1} to Ti–O stretching mode [213]. Additionally, 674 cm^{-1} Raman mode arises due to surface optical mode of STO. The STO2_1 thin film exhibits only five modes; 87, 418, 532, 621 and 792 cm^{-1} and additionally two intense Raman peaks present at 142 and 217 cm^{-1}, later of these two were owed to Raman modes of Cu_2O. The small third peak appears at 289 cm^{-1} is attributed to A_g mode indicates the appearance of CuO [214]. The STO3_1 sample has similar Raman peaks as that of pure STO thin film as shown in Figure 5-4 (c). In addition, there was a red shift in the Raman peaks in STO2_1 and STO3_1 films due to tensile strain present in presence of Cu metal nano-layer.

Table 5-3 *Optical phonon modes and their symmetry assignments in thin films.*

Modes	Modes assign	STO	STO2_1	STO3_1
		Raman shift (cm^{-1})	Raman shift (cm^{-1})	Raman shift (cm^{-1})
1	TO_1	89	87	87
2	$A_1(TO_2)$	118	-	108
3	(LO_1+TO_2)	174	-	166
4	TO_3	275	-	265
5	LO_3	420	418	418
6	TO_4	541	532	532
7	-	674	621	621
8	LO_4	795	792	792

5.2.3 UV-Visible-NIR transmission spectra of STO, STO2_1, and STO3_1 thin films

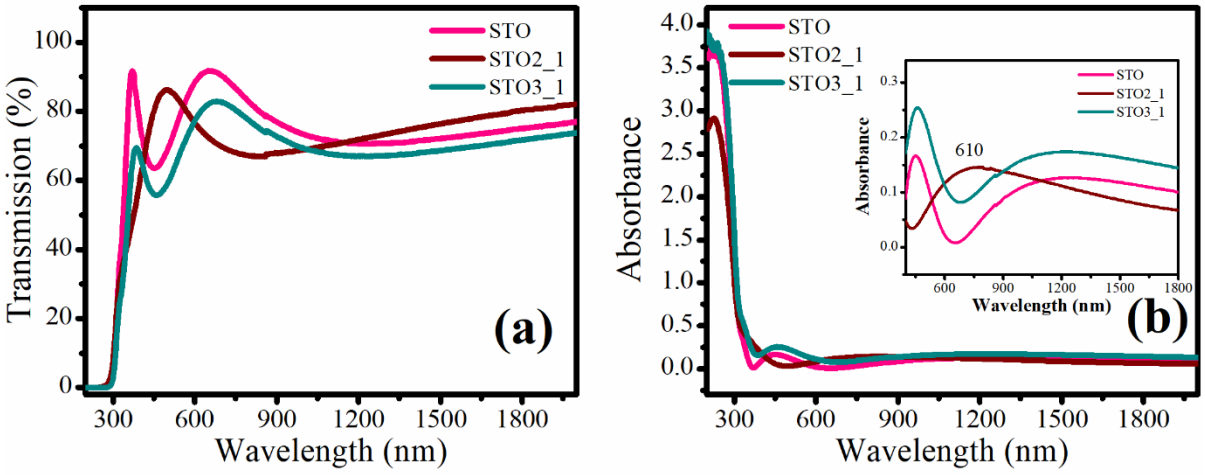

Figure 5-5 *(a) Transmission spectra (b) absorption spectra of STO, STO2_1 , and STO3_1 thin films and the inset shows an expanded view of 610 nm SPR peak in the STO2_1 thin film.*

The optical transmittance spectra in the wavelength range of 200 - 2000 nm for all the three samples deposited on quartz substrate are shown in Figure 5-5 (a) and the corresponding

absorbance spectra is depicted in Figure 5-5 (b). All the films exhibited optical transmittance (T) > 70% in the visible region. The appearance of interference fringes in the transmittance is indicative of good optical quality of the surface of the film. The transmittance of all the films decreased sharply around 300 nm due to the fundamental absorption of light beyond the bandgap ($h\nu > E_g$) and the occurrence of interband transitions. The fundamental absorption corresponding to electron excitation from valence band to conduction band is used to determine the nature and value of the optical band gap (E_g). The optical bandgap and absorption coefficients are related to the equation (2.7) and (2.6), respectively. The optical bandgap was calculated considering STO being an indirect bandgap material [51]. The refractive index of STO thin films were determined from Swanpoel envelope method by equations (2.1), (2.2) and (2.3) and are listed in Table 5-4.

Figure 5-6 shows the plot of $(\alpha h\nu)^{0.5}$ as a function of $h\nu$ (Tauc plot) for all three thin films.

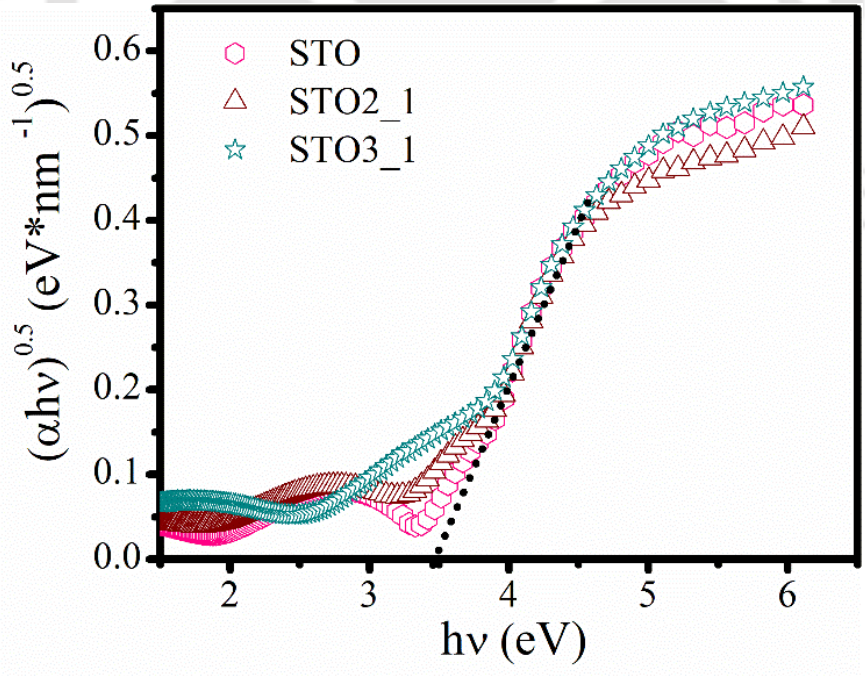

Figure 5-6 *Tauc plot for determining optical band gap (E_g) of all thin films deposited at T_s of 700 °C.*

From the equation (2.7), the values of E_g for STO, STO2_1, and STO3_1 thin films were found to be 3.51± 0.11, 3.53± 0.05, and 3.53 ± 0.04 eV, respectively, demonstrating that there was a marginal change in the absorption edge of thin films with the infusion of the Cu nano-layer. The slight blue shift in the bandgap was attributed to tensile strain formation in STO2_1 and STO3_1 thin films leading a bandgap broadening [193].

The absorption peak due to the SPR of Cu nanoparticles was observed around 610 nm in the STO2_1 thin film. In the Section 4.3.4, the SPR peak observed for BTO2_1 sample was around 625 nm. As it is well known that as the refraction index of the host media increases, SPR peak is always red-shifted. The refractive index of BTO thin film deposited for 60 minutes was lower compared to that of STO thin film deposited under the similar conditions.

5.2.4 Nonlinear optical properties study via modified *Z*-scan measurement

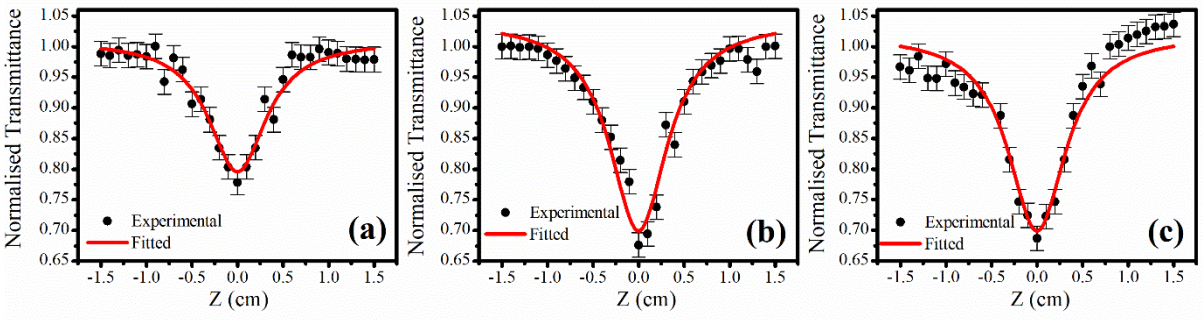

Figure 5-7 *Normalized OA Z-scan transmittance of (a) STO (b) STO2_1, and (c) STO3_1 thin films. Dots denote the experimental data and the solid line is the theoretical fit.*

The nonlinear optical response of all the three samples were investigated using the single-beam modified *Z*-scan technique as described in Section 2.4.8, Chapter 2. The OA *Z*-scan spectra of these samples along with fitted curve to equation (2.8) are shown in Figure 5-7. All the films exhibited RSA similar to that of BTO samples, Section 4.2.6, Chapter 4. The nonlinear optical absorption in STO thin film stems mainly from two-photon absorption (TPA).

Moreover, the TPA satisfies a relation $E_g < 2hv < 2E_g$, where E_g and hv are the band gap and photon energy, respectively [215]. This situation was in consistent with that of BTO film (E_g = 3.7 eV). Since, the value of E_g of STO thin film, 3.51 eV, was larger than the excitation energy of Ar-Ion laser (2.54 eV), TPA is not attributed to a direct transition process but to indirect transition process via the intermediate energy levels (defect states) inside the forbidden band gap. The values of β were estimated by fitting the OA *Z*-scan data point using equation (2.8) and are listed for all the films deposited on a quartz substrate in Table 5-4.

Table 5-4 *Values of α and β of STO, STO2_1, STO3_ 1 thin films.*

Sample	**Thickness (*L*) nm**	**Effective thickness (L_{eff}) nm**	**Refractive index (*n*) (at λ = 488 nm)**	**Linear absorption coefficient (α) × 10^{-4} cm^{-1}**	**Nonlinear absorption coefficient (β) cm/W**
STO	174	167	1.93	4.32	63.51 ± 0.13
STO2_1	180	175	-	3.45	182.34 ± 7.23
STO3_1	183	178	1.92	3.02	175.17± 5.89

The values of β were found to be 63.51, 182.34, and 175.17 cm/W for STO, STO2_1, and STO3_1 thin films, respectively. The observed enhanced nonlinear absorption coefficients in the latter two films were due to the collective oscillations of free electrons at the metal – dielectric interfaces as described in the Section 4.2.6, Chapter 4. It was also noticed that the β values were higher in comparison to that of BTO and its nanocomposite thin films. Moreover,

the low RMS surface roughness values of STO thin films give the enhancement in the β values compared to that of BTO thin films. As already discussed in Section 3.3.5, a rough surface leads to more scattering losses which directly affects the NLO properties. These results were also in good agreement with the previous reported results [216].

5.3 Conclusions

The PLD technique was implemented to fabricate polycrystalline thin films in three different configurations: pristine STO, Cu nano-layer sandwiched between substrate and STO, and Cu nano-layer on top of STO; STO, STO2_1, and STO3_1 thin films, respectively. Structural, linear and nonlinear optical properties of these thin films were studied. The XRD and Raman analysis confirmed that the films were in cubic phase. Raman intensity of STO2_1 film was three times higher than that of the first configuration due to the SERS effect. The SPR peak in STO2_1 thin film was observed around 610 nm, from UV-Visible-NIR spectrometer. The β values were estimated from the modified *Z*-scan technique and found to be 182.34 ± 7.23 cm/W for STO2_1 sample, which was higher than that of the other two thin films. These finding of plasmonic STO nanocomposite thin films will be useful for designing and fabrication of small, compact, and efficient devices for optoelectronics and photonic applications.

Chapter 6 : Compositional dependence on structural, linear and nonlinear optical properties of PLD deposited $Ba_{1-x}Sr_xTiO_3$ ($0 \leq x \leq 1$) thin films

Lead-free $Ba_{1-x}Sr_xTiO_3$ ($0 \leq x \leq 1$) (BST) thin films are essentially a perovskite-based solid solution of BTO and STO. The first constituent compound, BTO, is ferroelectric at room temperature, and it transforms to paraelectric phase with a sharp transition at the Curie temperature of 403 K [217]. On the other hand, STO is the paraelectric phase at absolute zero [218]. By replacing barium (Ba) with strontium (Sr) atoms, a linear decrease in Curie temperature with diffuse phase transition in the solid solutions of BST has been reported in the literature [218]. BST thin films have high transparency in the visible and infrared wavelength range with a relatively large refractive index as well as large electro-optical coefficient and low optical losses. Thus, BST simultaneously has the merits of the high dielectric constant of BTO and structural stability of STO, which makes BST material a novel one suitable in diverse applications. Further, properties of BST can be tailored for particular applications by changing the ratio of barium and strontium. For specific composition and temperature, BST can exhibit both paraelectric and ferroelectric behavior. It has received much attention due to its superior dielectric properties, electric field dependent permittivity, and high breakdown electrical field [219]. The BST thin films have been used in gas sensors, humidity sensors, tunable microwave devices, dynamic random access memory, and many other applications [220, 221].

The correlation between structural, linear, and nonlinear optical properties was not systematically documented in the earlier reports as a function of composition of BST

particularly via PLD technique. Therefore, the present chapter deals with the fabrication and characterization techniques of $Ba_{1-x}Sr_xTiO_3$ ($0 \leq x \leq 1$) (BST) thin films as a function of its composition, *x*, via the PLD technique. In addition, at an optimum composition, the effect of embedded Cu nano-layer on BST thin film and its nonlinear characterization was also carried out.

6.1 Experimental details

The samples of $Ba_{1-x}Sr_xTiO_3$ ($0 \leq x \leq 1$) having composition x = 0, 0.3, 0.4, 0.5, 0.7 and 1 are designated as BTO, BST-0.3, BST-0.4, BST-0.5, BST-0.7, and STO, respectively. The preparation of these targets have already been detailed in Chapter 2. The BST thin films were deposited onto quartz and Si (100) substrates via PLD technique. All the deposition parameters for BST films were kept same as those of the optimized BTO thin films are listed in Table 2-5, Chapter 2. Two more samples BST-0.5_1 and BST-0.5_2 thin films, listed in Table 2-6, Chapter 2 were fabricated to study the influence of Cu on BST film. The thickness of thin films was measured by Profilometer and also verified using the cross-sectional FESEM and Swanepoel envelope method. The stoichiometry and compositional analysis of the thin films were assessed by EDX spectra. The structural properties of BST thin films were studied via XRD and Raman analysis. The thin films were also subjected to AFM and FESEM for surface morphology and particle size distribution. Optical band gap energy and linear refractive index as a function of x were estimated using UV-Visible-NIR spectrum. Modified *Z*-scan measurement was performed to measure the value of β and n_2 as a function of x (Sr composition), using 488 nm of a cw Ar-Ion laser of wavelength as detailed in Section 2.4.8, Chapter 2.

6.2 Effect of Sr concentration in BST thin films

6.2.1 EDX spectra of BST thin films

Figure 6-1 shows EDX spectra of pulsed laser deposited $Ba_{1-x}Sr_xTiO_3$ ($0 \leq x \leq 1$) thin films.

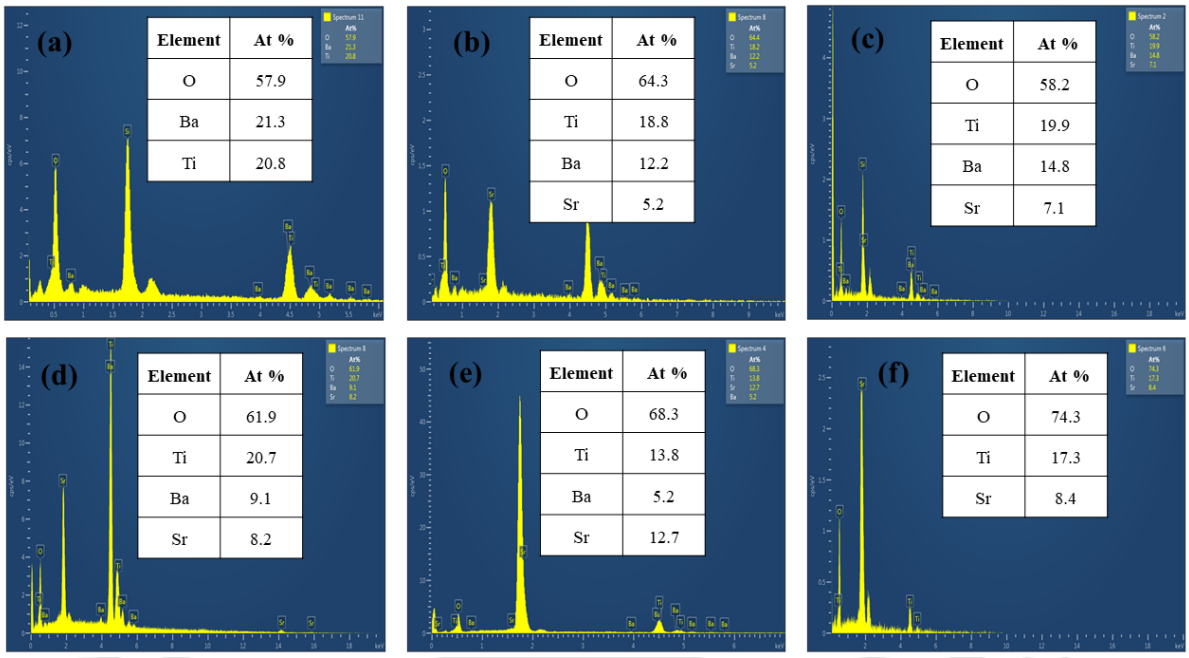

Figure 6-1 *EDX spectra of $Ba_{1-x}Sr_xTiO_3$ ($0 \leq x \leq 1$) thin films (a) x=0, (b) x=0.3, (c) x=0.4, (d) x=0.5, (e) x=0.7, and (f) x=1 deposited on Si substrate and inset indicates atomic percentage.*

Figure 6-2 depicts the atomic percentage from EDX measurement in the BST thin films along with those of corresponding BST powder (bulk) form for PLD target.

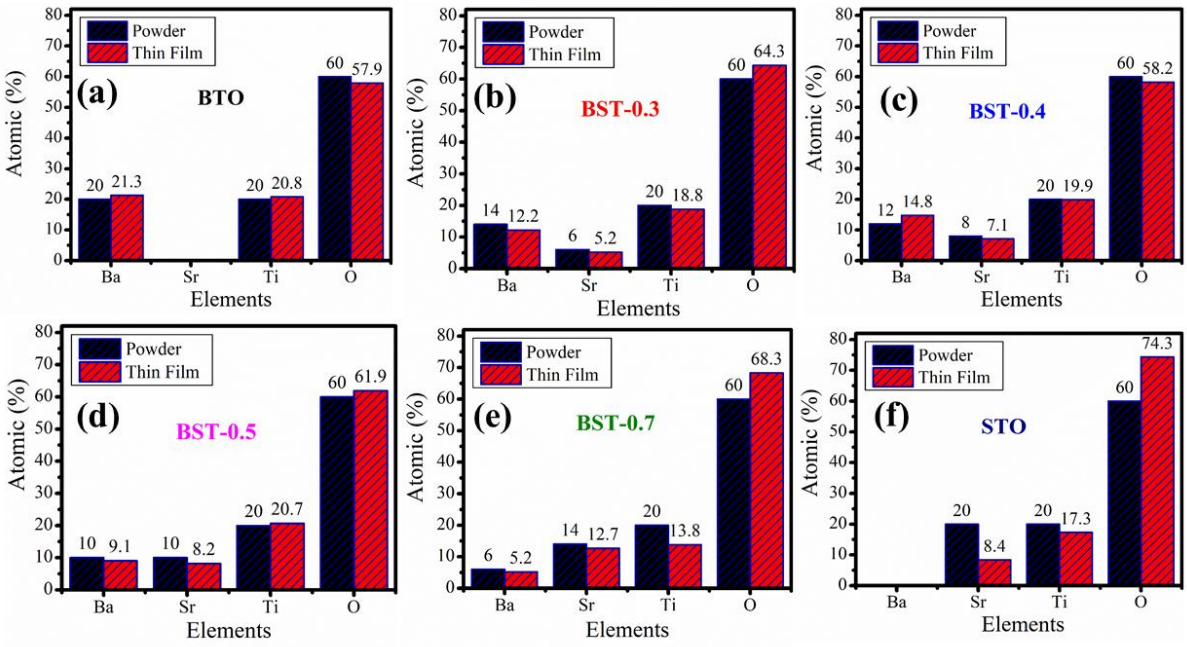

Figure 6-2 *Comparison of atomic percentage present in BST thin film and corresponding powder for the target.*

The obtained elemental compositions of all the films (but for pure STO) are almost equal to the powder volume fraction indicating nearly stoichiometric.

6.2.2 FESEM analysis of BST thin films

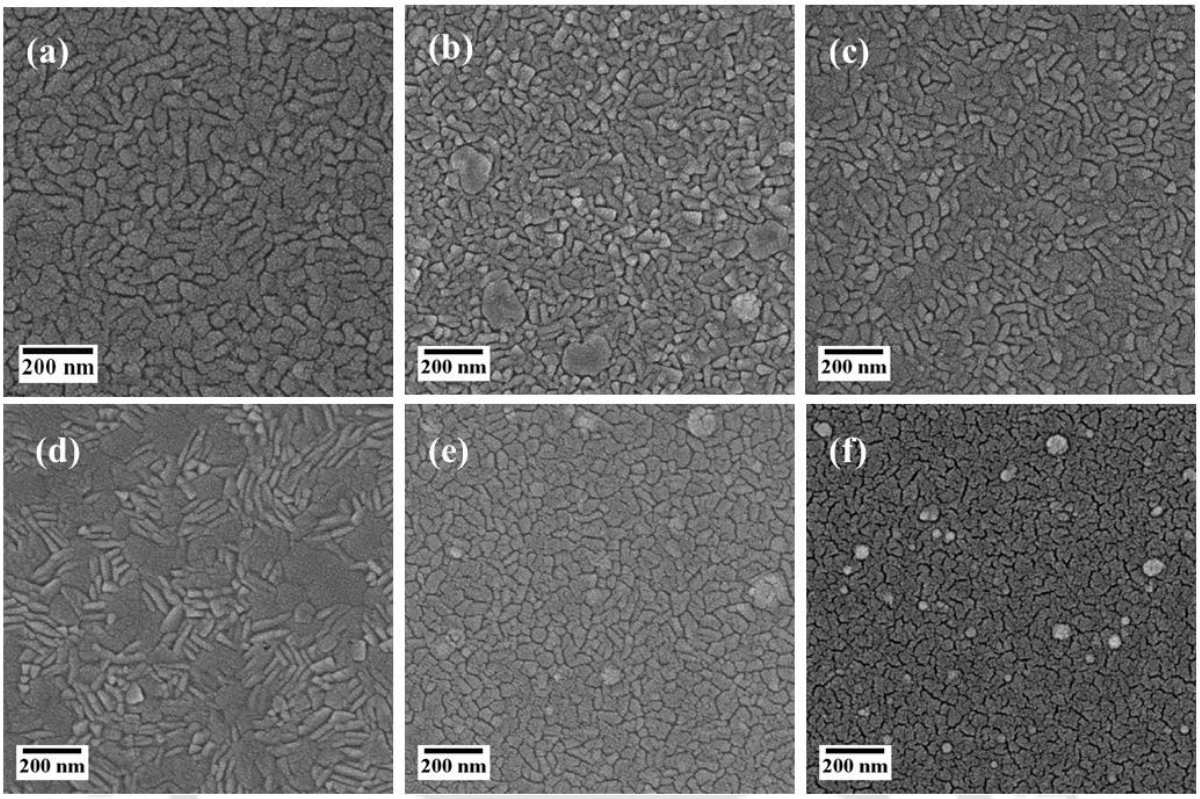

Figure 6-3 *FESEM images of $Ba_{1-x}Sr_xTiO_3$ ($0 \leq x \leq 1$) thin films (a) x=0, (b) x=0.3, (c) x=0.4, (d) x=0.5, (e) x=0.7, and (f) x=1 deposited on Si substrate.*

Figure 6-3 shows the FESEM micrographs of $Ba_{1-x}Sr_xTiO_3$ ($0 \leq x \leq 1$) thin films. For each and every film, FESEM images were captured at various location and it was observed that surface morphology was uniform irrespective of the imaged region in all the samples. All the films display nearly uniform distribution of grains over the surface. The grain size distribution in BST thin films via FESEM is displayed in Figure 6-4 (a) – (f). It is observed that the distribution of the nanostructured particles is of Gaussian nature for all BST films. The average particle size of BTO, BST-0.3, BST-0.4, BST-0.5, BST-0.7, and STO thin films was estimated to be ~ 54, 52, 49, 45, 42, and 41 nm, respectively. This is probably STO being of higher melting point likely to condensate fast on the substrate avoids any agglomeration and thus, the particle size is slightly reduced than that of pure BTO.

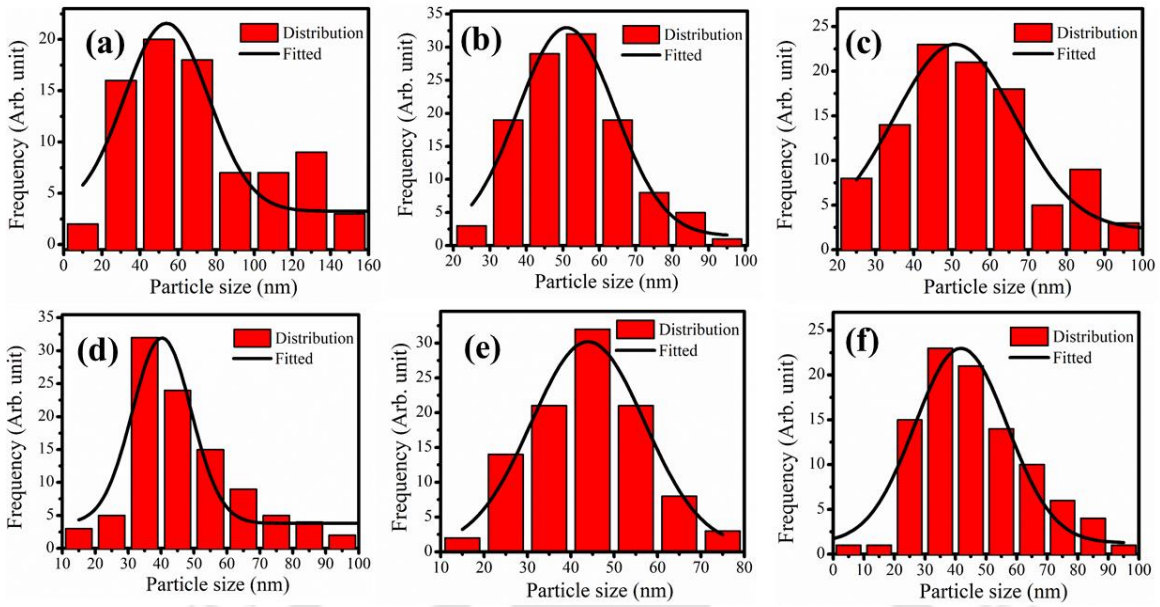

Figure 6-4 *Histogram depicting particle size distribution estimated from FESEM images of $Ba_{1-x}Sr_xTiO_3$ ($0 \leq x \leq 1$) thin films (a) x=0, (b) x=0.3, (c) x=0.4, (d) x=0.5, (e) x=0.7, and (f) x=1 deposited on Si substrate.*

The cross-sectional FESEM images of these films are shown in Figure 6-5 (a) – (f) and the thickness was found to be 360 nm for all the samples.

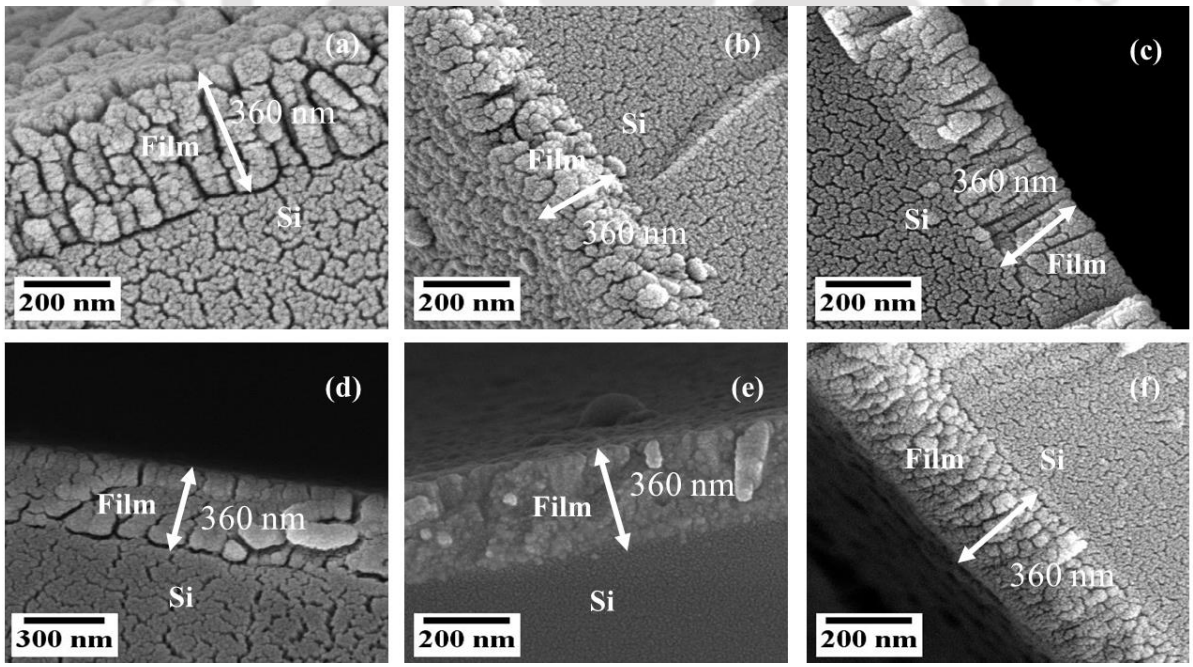

Figure 6-5 *Cross-sectional images of $Ba_{1-x}Sr_xTiO_3$ ($0 \leq x \leq 1$) thin films (a) x=0, (b) x=0.3, (c) x=0.4, (d) x=0.5, (e) x=0.7, and (f) x=1 deposited on Si substrate.*

6.2.3 XRD spectra of BST thin films

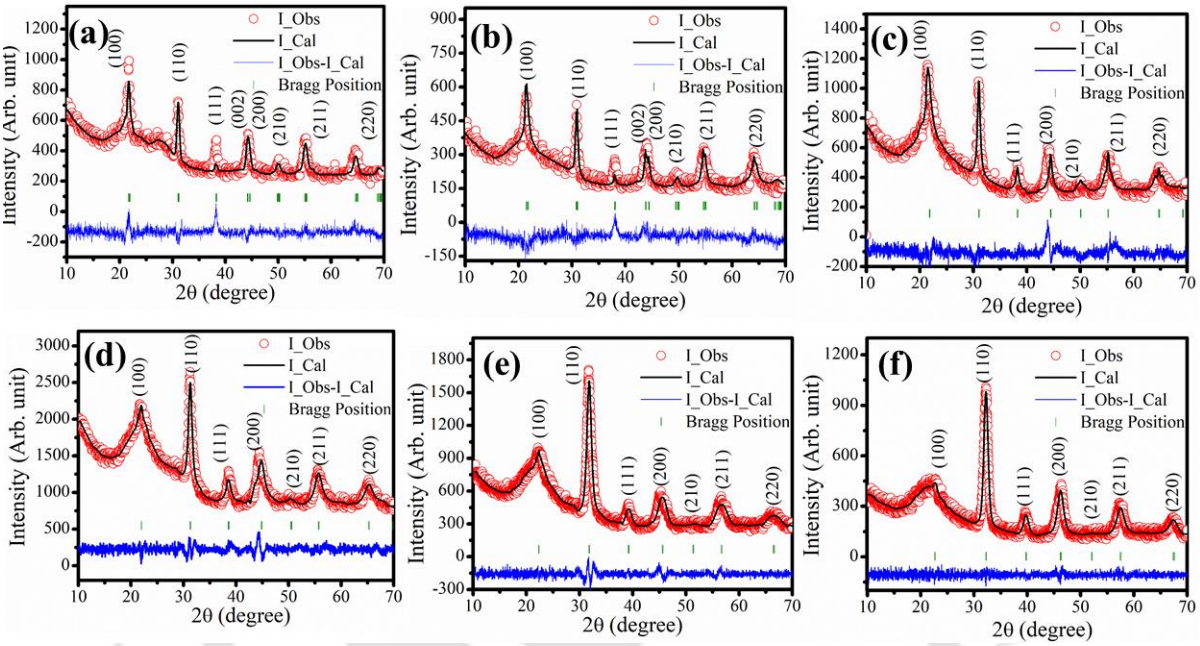

Figure 6-6 *Rietveld Refined plots of XRD spectra for $Ba_{1-x}Sr_xTiO_3$ ($0 \leq x \leq 1$) thin films (a) x=0, (b) x=0.3, (c) x=0.4, (d) x=0.5, (e) x=0.7, and (f) x=1 deposited on the quartz substrate.*

Figure 6-6 (a) – (f) illustrates the XRD pattern of BST thin films on quartz substrate fabricated at a substrate temperature 700°C along with Rietveld refinement. From the refinement analysis, it was found that all the samples exhibited a single phase with cubic crystal symmetry and belonged to $P_{m\text{-}3m}$ space group for $Ba_{1-x}Sr_xTiO_3$ (x = 0.4, 0.5, 0.7, 1) thin films and tetragonal phase with P_{4mm} space group for $Ba_{1-x}Sr_xTiO_3$ (x = 0, 0.3) thin films. The XRD spectra demonstrate different diffraction peaks (100), (110), (111), (200), (210), (211), and (220) planes which are the signature peaks of $Ba_{1-x}Sr_xTiO_3$ (x = 0.4, 0.5, 0.7, 1). The XRD peak at 2θ = 45º shows splitting for $Ba_{1-x}Sr_xTiO_3$ (x = 0, 0.3), which indicates a tetragonal structure. Furthermore, the peaks corresponding to pure STO and BTO phase are not detected for $Ba_{1-x}Sr_xTiO_3$ (x = 0.3, 0.4, 0.5, 0.7) thin films. This confirms a good dissolution of Sr in the BTO or vice versa. The high intensity of (110) peak of pure BTO was observed at 31.01° (as per PDF Card No.: 01-084-9618, ICSD collection code: 252562). This peak started shifting

towards higher diffraction angle with increasing Sr concentration. The increased in 2θ value indicates that interplanar spacing (d_s) decreases with increasing Sr concentration and hence, the BST films acquired compressive strain. The variation in lattice parameter and cell density & cell volume and crystallite size as a function of x are shown in Figure 6-7 & Figure 6-8, respectively. It is evident that the lattice parameters and density of the thin films were found to be decreased with x (increasing Sr concentration). It demonstrated that Sr^{2+} ions were incorporated at the A site (Ba^{2+}) instead of the B site (Ti^{4+}) of BST thin film due to smaller ionic radii of Ti^{4+} (0.61 Å) ion. It is worth mentioning in this context that the decreased value of lattice parameter with increasing Sr concentration in BST thin films is due to the smaller ionic radii of Sr^{2+} (~ 1.13 Å) than that of Ba^{2+} (~1.35 Å) [185]. A similar trend was reported for BST thin films fabricated via PLD in literature [222]. The cell density of the BST thin films decreases with increase in Sr concentration due the difference in atomic masses (Ba = 137.33 u, Sr = 87.62 u, Ti = 47.867 u, O_2 = 15.999 u).

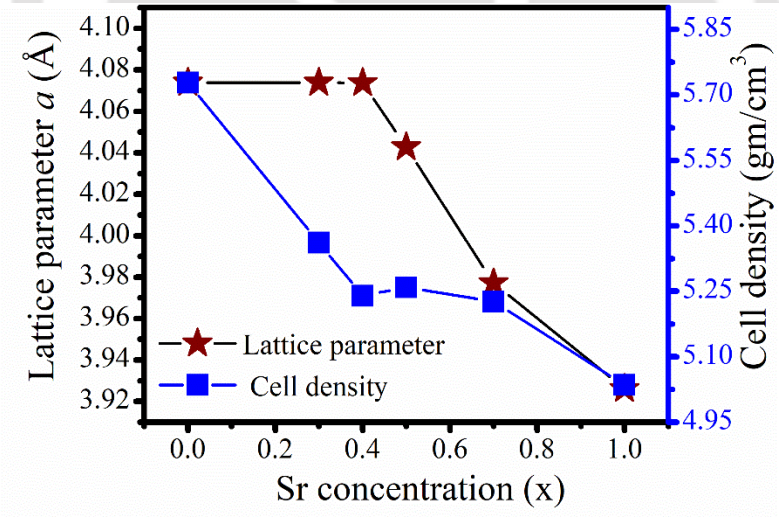

Figure 6-7 *Variation of lattice parameter and cell density of BST thin films as a function Sr concentration, x in BST thin films deposited on the quartz substrate.*

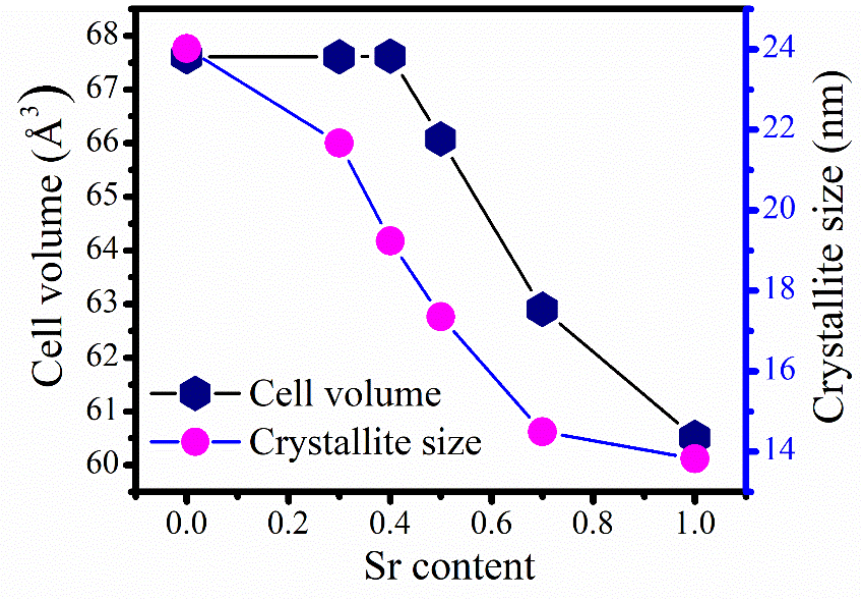

Figure 6-8 *Cell volume and crystallite size variation with Sr concentration in BST thin films deposited on the quartz substrate.*

The crystallite size (*D*) of each film was determined from the FWHM of the preferred orientation of the (110) plane, using the Scherer formula, equation (3.1) and is shown in Figure 6-8. For $Ba_{1-x}Sr_xTiO_3$ (x = 0, 0.3, 0.4, 0.5, 0.7 and 1) thin films deposited on quartz substrate, the calculated *D* values were found to be 24, 22, 20, 18, 15, and 14 nm, respectively. The structural parameters of BST thin films obtained from Reitveld analysis are listed in Table 6-1.

Table 6-1 *Structural parameters of BST thin films obtained from Reitveld analysis*

Thin film	Crystal system	Lattice parameter		Cell volume (V) (Å^3)	Cell density (gm/ cm^3)	Crystallite size (D) (nm)
		$a = b$ (Å)	c (Å)			
BTO	Tetragonal	4.084	4.118	68.684	5.728	24
BST-0.3	Tetragonal	4.073	4.097	67.966	5.362	22
BST-0.4	Cubic	4.063		67.072	5.259	20
BST-0.5	Cubic	4.043		66.085	5.239	18
BST-0.7	Cubic	3.977		62.907	5.226	15
STO	Cubic	3.926		60.516	5.035	14

Furthermore, the cell volume was decreased with increasing Sr concentration in BST thin film. These results ascribed the same analogy as explained for the lattice parameter. As lattice parameter was found to be decreased with the increased value of Sr concentration; as a result, lattice cell volume tends to decrease, as shown in Figure 6-8.

6.2.4 Raman spectra of BST thin films

RT micro-Raman spectra in the range of 50 to 1000 cm^{-1} of BST thin films of different compositions deposited on quartz substrate at T_s 700 °C are shown in Figure 6-9 (a) - (f).

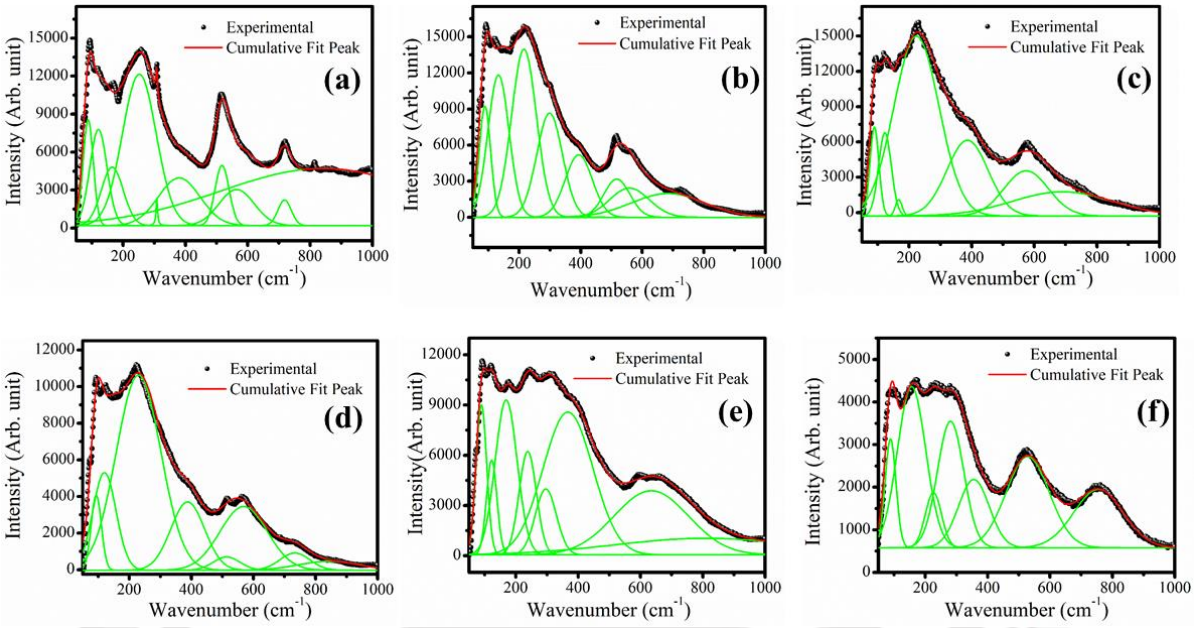

Figure 6-9 *De-convoluted Raman spectra for $Ba_{1-x}Sr_xTiO_3$ ($0 \leq x \leq 1$) thin films (a) x=0, (b) x=0.3, (c) x=0.4, (d) x=0.5, (e) x=0.7, and (f) x=1deposited on quartz substrate.*

The Raman bands were observed at 122, 188, 272, 306, 517, 642, 717, and 824 cm^{-1} for pure BTO thin films, as shown in Figure 6-9 (a) [169]. All these modes, corresponding to Raman bands of BTO have already been detailed in Section 3.2, Chapter 3. The band around 306 cm^{-1} and 717 cm^{-1} are characteristic of the tetragonal BTO phase. The Raman spectra of thin films for $Ba_{1-x}Sr_xTiO_3$ ($0 < x < 1$) contain the bands of hard phonon modes (88, 123,174, 238, 559, 635, and 739 cm^{-1}), and these are attributed to TO_1, $A_1(TO_2)$, (LO_1+TO_2), TO_3, TO_4, TO_2+LO_1, TO_3+LO_2, and TO_4 phonon modes, respectively [223]. The BST-0.3 thin film has tetragonal crystal symmetry. In contrast, BST -0.4, BST-0.5, BST-0.7 and STO thin films have cubic crystal symmetry confirmed from Raman analysis, and all these results are corroborated with XRD analysis. STO is a cubic crystal having 12 optical phonon modes. All optical modes arise

in STO thin films due to strain or oxygen vacancies as discussed in Section 5.2.2, Chapter 5. The Raman spectra of STO thin films observed at 85–120 cm^{-1} (TO_1: the soft mode), and the hard modes TO_2+LO_1 (these two modes have very close frequencies) at 180 cm^{-1}, TO_3, LO_3, TO_4, and LO_4 at 281, 395, 528, and 755 cm^{-1}, respectively. All the Raman modes of BST thin films were redshifted compared to BST thin films reposted in literatures [45, 219]. All the thin films having tensile strain compared to bulk materials, therefore the Raman modes of the thin films were redshifted.

6.2.5 UV-Visible-NIR spectra of BST thin films

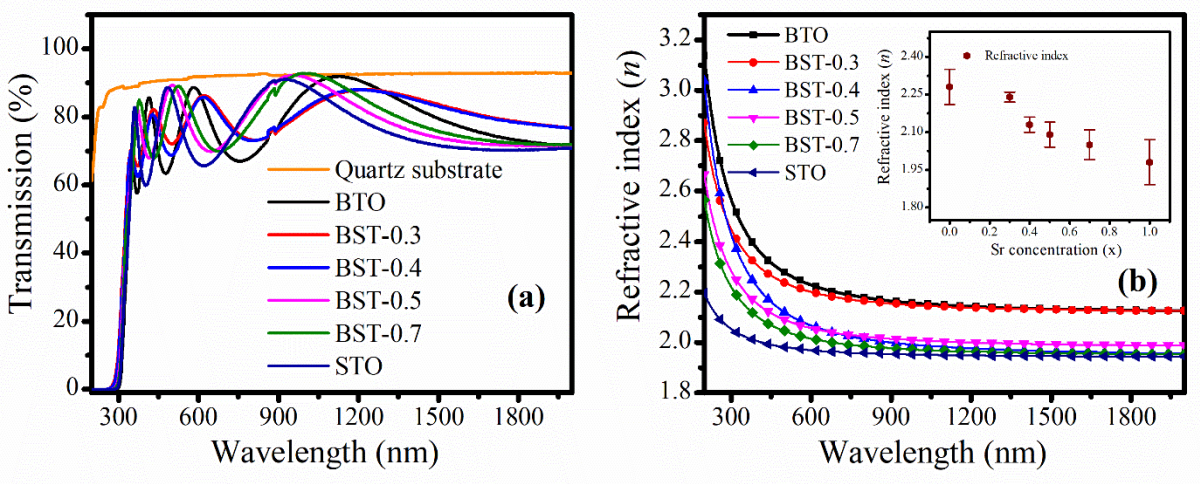

Figure 6-10 *(a)UV-Visible -NIR transmission spectra as a function of wavelength of PLD* $Ba_{1-x}Sr_xTiO_3$ *(0 ≤ x ≤ 1) thin films along with the transmission of bare quartz substrate for reference and (b) variation of refractive index as a function of wavelength and the inset shows the dependence of Sr concentration of BST thin films at* λ *=488 nm.*

The UV-Visible NIR transmission spectra of the films deposited on quartz substrate are shown in Figure 6-10 (a), clearly exhibiting the interference fringes indicating good quality and uniform thickness of the films. All the thin films exhibit similar transmission spectra with peak transmission of ~ 85 % and it falls down to ~ 75 % in the NIR region. The linear refractive indices (*n*) were estimated in these thin films via Swanepoel envelop method using the equation (2.1) - (2.3), Chapter 2. The variation of *n* with the wavelength in spectral range of 200-2000

nm is shown in Figure 6-10 (b), and dependence of Sr content at λ = 488 nm is displayed in the inset. The estimated linear refractive index decreases with the increase in wavelength, which signifies the normal dispersion. BTO thin film has higher *n* value compared to STO thin film due to better crystallinity and compactness of BTO. The refractive index of bulk STO (n = 2.30 – 2.65) whereas for bulk BTO (n ~ 2.3). Furthermore, the value of *n* for well crystallised STO thin films varies from 2.15 to 2.35 and BTO thin films (n = 2.15 – 2.55) [51]. But, the value of *n* of STO and BTO thin films in present scenario was lower than that of literature. This suggests that these BST thin films having relatively low density compared to that of reported in literature. The thickness of all these films was obtained from equation (2.4) using the Swanepoel envelope approximation. The thickness of BST thin films was also measured via Profilometer measurement and FESEM and all these observations are listed in Table 6-2 in good agreement with each other.

Table 6-2 *Thickness assessment of all BST samples from cross-sectional FESEM images and Profilometer and Swanepoel approximation.*

Thin films	Thickness (FESEM)	Thickness (Profilometer)	Thickness (Swanepoel)
BTO	359 ± 10	360 ± 10	366
BST-0.3	354 ± 10	358 ± 10	361
BST-0.4	355 ± 10	354 ± 10	363
BST-0.5	356 ± 10	360 ± 10	365
BST-0.7	355 ± 10	355 ± 10	364
STO	357 ± 10	357 ± 10	357

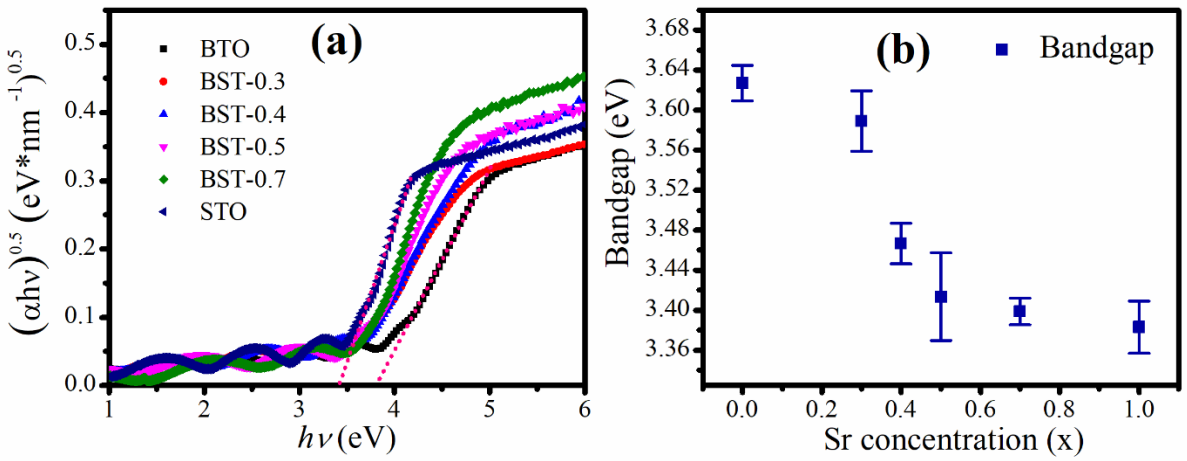

Figure 6-11 *(a) Plot of $(\alpha hv)^{0.5}$ versus hν (Tauc plot) and (b) Sr concentration dependence of the bandgap energy for BST thin films deposited at substrate temperature 700 ºC.*

The bandgap E_g of BST thin films was calculated through the Tauc plot as depicted in Figure 6-11. The linear absorption coefficient (α) is related to photon energy ($h\nu$), given by the equation (2.7), Chapter 2. The values of α were found to be 3.48×10^{-4}, 5.79×10^{-4}, 5.88×10^{-4}, 10.21×10^{-4}, 9.96×10^{-4}, 8.34×10^{-4} for BTO, BST-0.3, BST-0.4, BST-0.5, BST-0.7 and STO thin films, respectively. The values of E_g of BST thin films were estimated by assuming an indirect transition between conduction and valence bands. Via Tauc plot, the E_g values were found to be 3.62 ± 0.02, 3.58 ± 0.03, 3.46 ± 0.02, 3.41 ± 0.04, 3.39 ± 0.01 and 3.38 ± 0.03 eV for BTO, BST-0.3, BST-0.4, BST-0.5, BST-0.7 and STO thin films, respectively. The absorption edge of STO thin film is lower than that of the BTO thin film as shown in Figure 6-11 (b). Similar trend was observed in the the literature [224]. In nanocrystalline materials, the surface-to-volume ratio is higher, and band bending can be expected at the grain boundaries. In crystallites with smaller sizes, the band bending effect will be more compared to that of bigger crystallites. Therefore, BTO thin film having higher crystalline size possess higher bandgap than that of STO thin film having smaller size.

6.2.6 Nonlinear optical properties of BST thin films

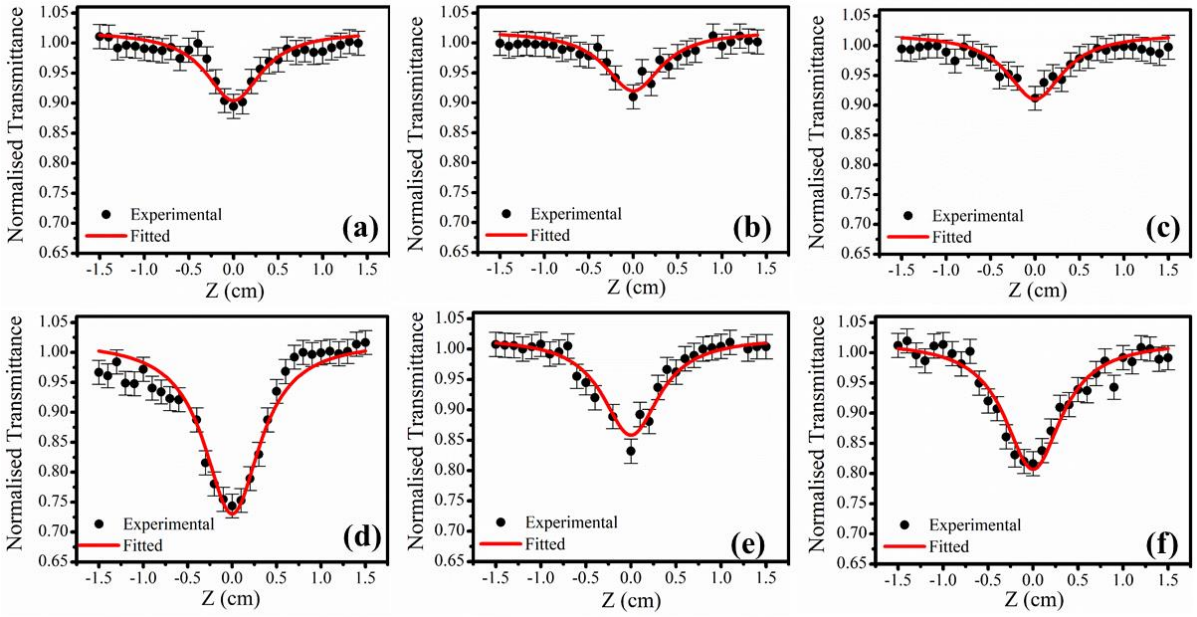

Figure 6-12 *OA Z-scan curves for $Ba_{1-x}Sr_xTiO_3$ ($0 \leq x \leq 1$) thin films (a) x=0, (b) x=0.3, (c) x=0.4, (d) x=0.5, (e) x=0.7, and (f) x=1 deposited on quartz substrate.*

Nonlinear absorption coefficient and nonlinear refractive index coefficient were assessed from OA and CA *Z*-scan spectra, Section 2.4.8, Chapter 2. Figure 6-12 (a) - (f) shows the normalized OA *Z*-scan plot for $Ba_{1-x}Sr_xTiO_3$ ($0 \leq x \leq 1$) thin films along with the data fitted to equation (2.8), Chapter 2. All the films exhibit a transmittance minimum at $z = 0$ in the spectra, suggesting RSA behavior. In the present *Z*-scan measurement, the dominant process for the nonlinear absorption is due to the TPA process as the pump photon energy (hv = 2.54 eV, λ = 488 nm) is more than half of the bandgap energy of BST thin films.

Figure 6-13 shows the CA Z-scan plots of BST thin films along with the data fitted to equation (2.10), Chapter 2. Pre-focal transmittance maxima followed by a post focal minima in the CA data indicate the negative nonlinear (Δz_{p-v}) refraction (self – defocusing) in all these thin films. Additionally, the peak and valley separation in the thin films turns out to be in the range of $1.7z_0$, which satisfies the condition for the third-order NLO process.

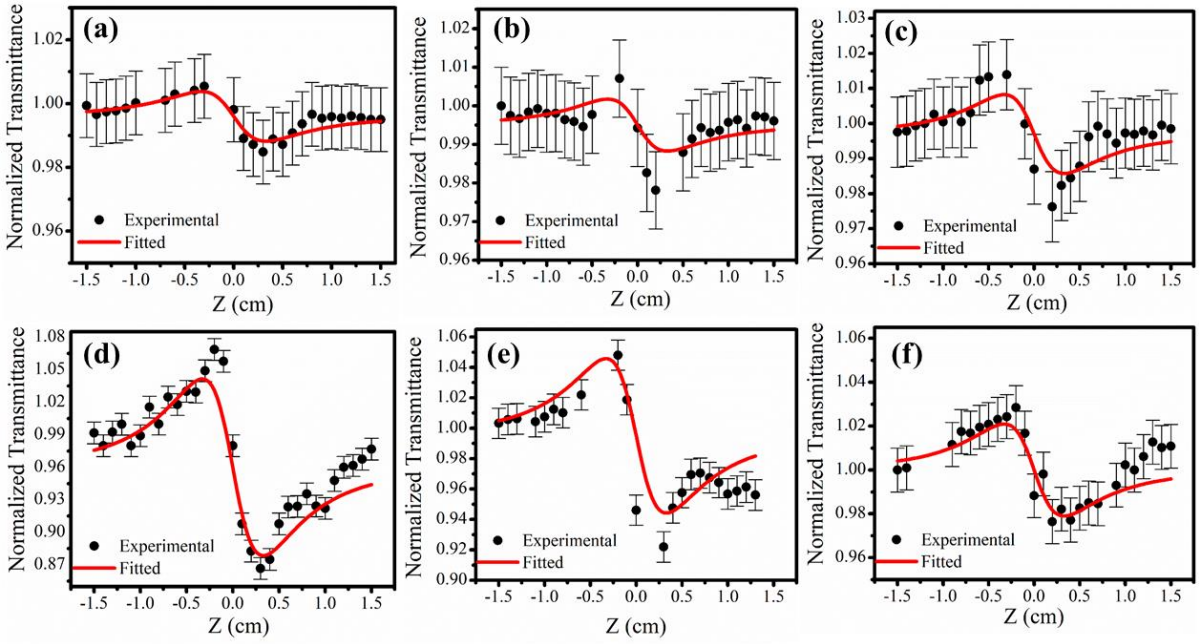

Figure 6-13 *CA Z-scan curves for $Ba_{1-x}Sr_xTiO_3$ ($0 \leq x \leq 1$) thin films (a) x=0, (b) x=0.3, (c) x=0.4, (d) x=0.5, (e) x=0.7, and (f) x=1 deposited on quartz substrate.*

The nonlinear absorption coefficient (β) and nonlinear refractive index coefficient (n_2) of the PLD $Ba_{1-x}Sr_xTiO_3$ ($0 \leq x \leq 1$) thin films were estimated from their respective OA and CA *Z*-scan plot. The variation of β and n_2 as a function of Sr concentration is shown in Figure 6-14 and is also listed in Table 6-3.

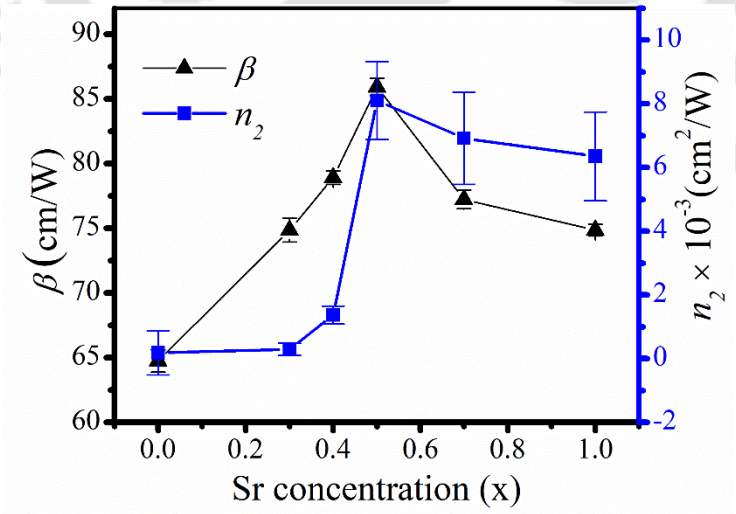

Figure 6-14 *Variation of β and n_2 with Sr concentration.*

Both NLO coefficients were observed to increase with the Sr content in the films till x = 0.5 and after that these were observed to decrease. The increase in nonlinear optical coefficients of BST-0.5 thin film can be explained on the basis of the uniform grain size (having rice shaped grain structure). Similar behavior was reported for BST thin films in the literature [73, 225]. The NLO coefficients are inversely proportional to the bandgap of the material [226]. Thus, pure STO thin film has (E_g = 3.38 eV) possess higher nonlinearity, as compared to that of pure BTO thin film (E_g = 3.62 eV). The real, as well as imaginary parts of the third order NLO susceptibilities ($\chi^{(3)\prime}$ and $\chi^{(3)\prime\prime}$), were estimated by using the equations (2.15) and (2.16), respectively, Chapter 2 and are listed in Table 6-3.

Table 6-3 *NLO coefficients (β, n_2, $\chi^{(3)\prime}$, $\chi^{(3)\prime\prime}$ and $\chi^{(3)}$) of BST thin films*

Thin films	**β (cm/W)**	**n_2 (cm^2/W) × 10^{-3}**	**$\chi^{(3)\prime}$ (esu) × 10^{-4}**	**$\chi^{(3)\prime\prime}$ (esu) × 10^{-4}**	**$\chi^{(3)}$ (esu) × 10^{-4}**
BTO	64.74 ±0.85	0.18 ± 0.69	12.37± 0.52	1.23± 0.22	12.43 ± 0.53
BST-0.3	74.85 ± 0.45	0.29± 0.19	23.68± 1.61	1.27 ± 0.34	23.71 ± 1.61
BST-0.4	78.91 ± 0.67	1.37±0.28	35.75± 4.25	1.95± 0.41	35.80 ± 4.23
BST-0.5	85.91 ± 0.67	8.10±1.22	65.33± 5.60	3.35± 0.24	67.39 ± 5.60
BST-0.7	77.22 ± 0.72	6.92±1.45	51.10± 6.37	3.09± 0.45	51.16 ± 6.38
STO	74.85 ± 0.45	6.35±1.39	63.05± 6.72	2.88 ± 0.19	63.11 ± 6.71

From Table 6-3, it is obvious that the magnitude of NLO coefficients (β and n_2) along with the nonlinear optical susceptibilities ($\chi^{(3)\prime}$, $\chi^{(3)\prime\prime}$ and $\chi^{(3)}$) are large as compared to that of observed under short-pulsed laser illumination [36, 225]. This is due to the thermal origin of the

nonlinearity in the films illuminated via a cw laser. Under cw laser e.g. Ar-Ion Laser in the present case, the thermally induced optical nonlinearity plays a vital role due to its thermally induced refractive index change [226].

The effective thermal-induced nonlinear refractive index coefficient (n_2^{th}), which is expressed as [226],

$$n_2^{th} = \left(\frac{dn}{dT}\right)\frac{\alpha R^2}{k_T} \tag{6.1}$$

where dn/dT is the variation of linear refractive index with temperature, α is linear absorption coefficient, R is the radius of the incident laser beam and $k_T = D_T \rho C_p$ is coefficient of thermal conductivity, D_T is thermal diffusivity, ρ is density and C_p is specific heat of the material of the thin films. For small changes of linear refractive index of the thin films w.r.t temperature (dn/dT), the nonlinear refractive index coefficient solely depends on the ratio of α/D_T. In the present work, a gradual increase in n_2 till $x = 0.5$ (i.e. BST-0.5), then it starts falling down with increase in Sr concentration in BST thin films. The value of linear absorption coefficient of BST-0.5 thin film was higher compared to that of thin films. Therefore, BST-0.5 thin film has greater $\chi^{(3)}$ than the rest of the samples. The obtained large third-order nonlinearity, strong absorption coefficient, and greater $\chi^{(3)}$ in the present films are promising for the applications in optical and photonic devices.

6.3 Effect of Cu nano-layer on BST-0.5 thin film

In Chapter 4 and Chapter 5, it was shown that the presence of nanostructured Cu layer in between substrate and BTO and STO, respectively enhances the NLO properties. Therefore, in this Section, BST (x = 0.5) composition having maximum NLO response was tested for the influence of Cu nano-layer. Two thin films were fabricated via PLD as listed in Table 2-6. The AFM images, linear, and nonlinear optical properties of these two films are described in following subsection.

6.3.1 AFM images of BST-0.5_1 and BST-0.5_2 thin films

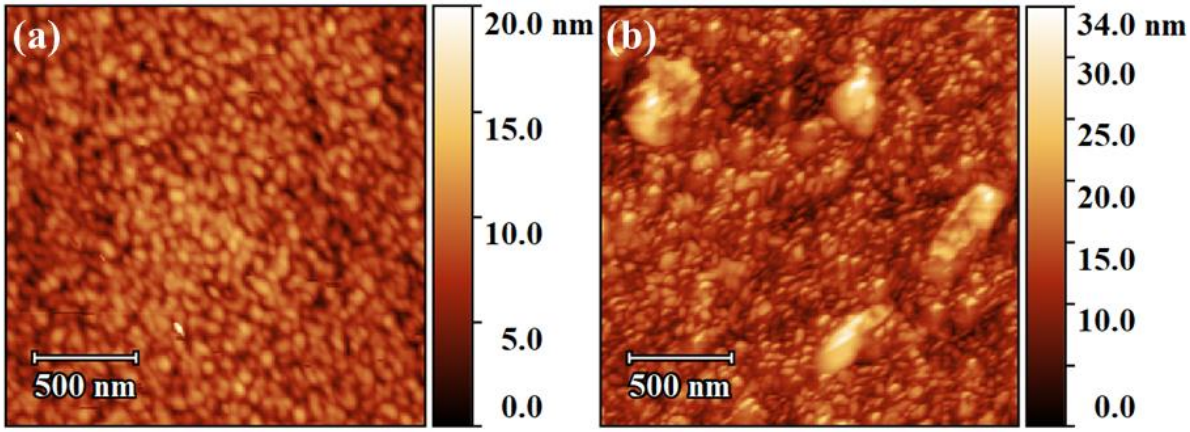

Figure 6-15 *2D AFM images (2 × 2 μm^2) of BST-0.5_1, and BST-0.5_2 thin films deposited on the quartz substrate.*

Figure 6-15 depicts AFM images of BST-0.5_1 and BST-0.5_2 thin films deposited on quartz substrate for 60 minutes. The RMS roughness of films obtained from these images and found to be (1.51 ± 0.21), and (3.95 ± 1.09) nm for BST-0.5_1 and BST-0.5_2 thin films, respectively.

6.3.2 Linear optical properties of Cu nano-layer sandwiched BST (x = 0.5) film

The UV-Vis-NIR transmission spectra of BST-0.5_1 and BST-0.5_2 thin films fabricated via PLD technique on quartz substrate are shown in Figure 6-16 (a) in the 200-2000 nm spectral range, inset shows the SPR peak of BST-0.5_2 thin film around 615 nm. The transmittance of BST-0.5_2 thin film decreases, and the interference fringes reduces with the addition of Cu nano-layer due to overlapping of SPR peak. The low optical transmittance in the second thin film is due to the reflection from the Cu nano-layer. The SPR peak in the absorption spectra indicates the presence of the Cu nanoparticles in the second thin film.

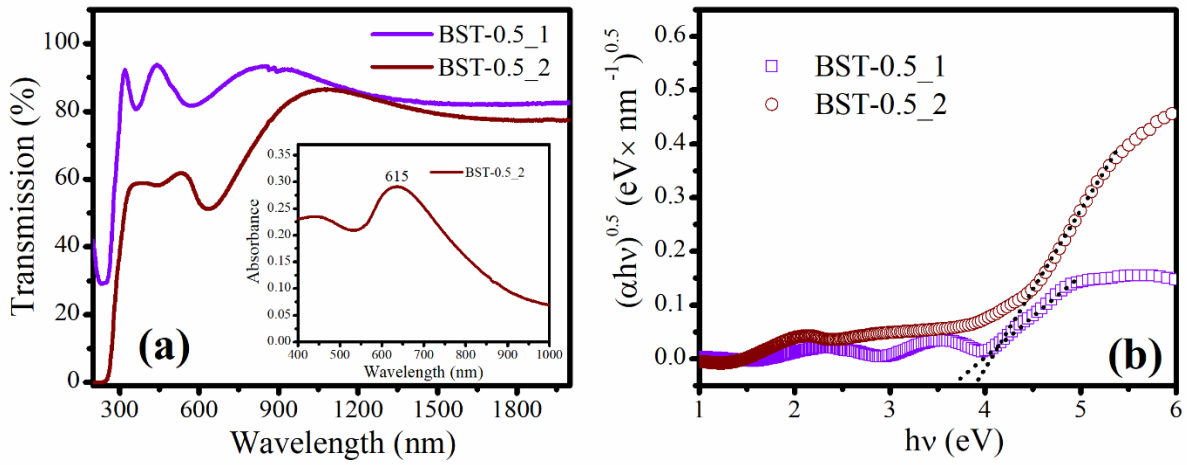

Figure 6-16 *The UV-Visible-Transmission spectra of BST-0.5_1 and BST-0.5_2 thin films deposited on quartz substrate. Inset shows the SPR peak of BST-0.5_2 thin film at 615 nm and (b) Tauc plot of BST-0.5_1 and BST-0.5_2 thin films.*

The optical bandgap of these two films was calculated by Tauc plot and found to be (3.64 ± 0.04) and (3.86 ± 0.05) eV for BST-0.5_1 and BST-0.5_2 thin films, respectively. There was a blue shift in the bandgap due to the addition of Cu nano-layer on BST-0.5 thin film. This was similar to that for BTO2_1 and STO2_1 thin films, and the reason has already been discussed in Section 4.3.4 and Section 5.2.3, respectively.

6.3.3 Nonlinear optical properties

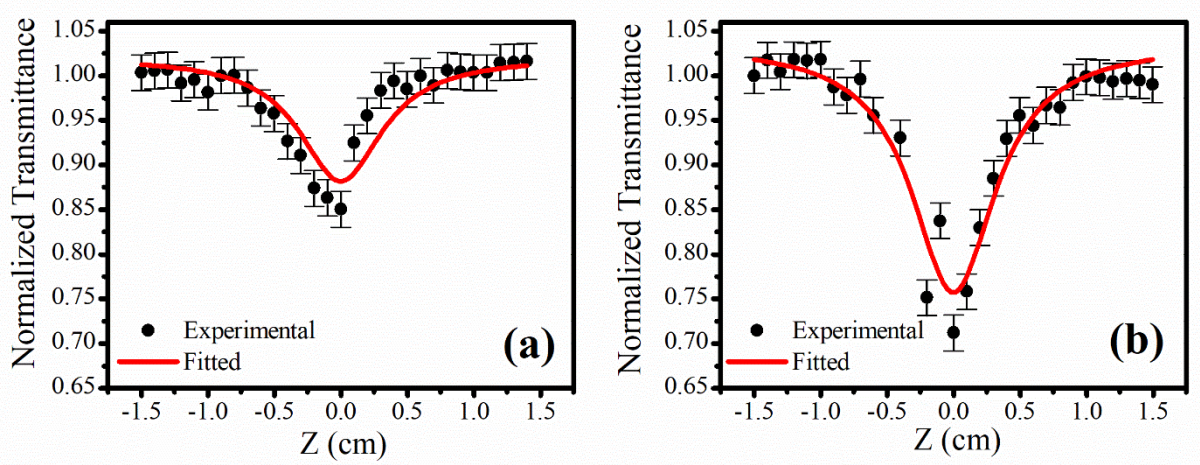

Figure 6-17 *OA Z-scan curves (a) BST-0.5_1 (b) BST-0.5_2 thin films deposited for 60 minutes on the quartz substrate.*

Figure 6-17 (a) – (b) shows the normalized OA *Z*-scan plot for BST-0.5_1 and BST-0.5_2 thin films along with the fitted data to equation (2.8), Chapter 2. These two films have minima at the $z = 0$ exhibiting RSA behavior. In this case too, the NLO process is due to multiphoton absorption (basically two photon absorption) as it satisfies the condition for TPA. The β value was calculated using the equation (2.8) for the two thin films, and the values were found to be 73.24 ± 0.32 and 188 ± 0.45 cm/W for BST-0.5_1 and BST-0.5_2 thin films, respectively. The β value of BST-0.5_2 thin film was around three times higher than that of pristine BST-0.5_1 thin film. The large value of the NLO absorption observed for the second thin film is attributed to the local field enhancement due to the SPR peak at the metal-dielectric interface.

6.4 Conclusions

BST-x (x = 0, 0.3, 0.4, 0.5, 0.7, and 1) thin films were fabricated via PLD and deposited on both quartz substrate and silicon substrates. Structural, linear, and nonlinear optical properties of all thin films were reported. Structural properties confirmed that the deposited BST-0.4, BST-0.5, BST-0.7, and STO thin films were predominately in the cubic phase,

whereas BTO and BST-0.3 were in the tetragonal phase. The lattice parameter, density, and crystallite size were decreased with increasing Sr concentration in BST thin films. The linear optical properties were studied by UV-Vis-NIR transmission Spectroscopy. The optical bandgap of the thin films calculated using the Tauc plot was red-shifted from 3.62 ± 0.02 to 3.38 ± 0.03 eV with increasing Sr concentration. The refractive index of BST thin films was decreasing with increasing Sr concentration and it attains minimum for STO thin film. All thin films exhibit absorptive and refractive nonlinearity and exhibited RSA behavior. The values of the third-order nonlinear optical coefficients (β, n_2, $\chi_R^{(3)}$, $\chi_I^{(3)}$ *and* $\chi^{(3)}$) in $Ba_{1-x}Sr_xTiO_3$ ($0 \leq x \leq 1$) thin films were found to be in the range of (64.74 – 74.85) cm/W, (0.18– 6.35) $\times 10^{-3}$ cm^2/W, (12.37-63.05)$\times 10^{-4}$ esu, (1.23-2.88)$\times 10^{-4}$ esu, and (12.43-63.11)$\times 10^{-4}$ esu, respectively. The maximum value of both NLO coefficients at $x = 0.5$ sample (i.e. BST-0.5) is due to the uniform grain growth with good homogeneity. At optimum Sr concentration, Cu nano-layer embedded on BST-0.5 thin film fabricated and its structural, linear and nonlinear optical properties were studied through UV-Visible-NIR spectroscopy and the modified *Z*-scan technique. The nonlinear absorption coefficients of BST-0.5_1 and BST-0.5_2 thin films were found to be (73.24 ± 0.32) and (188 ± 0.45) cm/W, respectively. The BST-0.5_2 film attains a higher β value compared to BTO2_1 and STO2_1 thin films.

Chapter 7 : Influence of Cu nano-layer on optical limiting in BTO, STO, and BST PLD thin films

In previous chapters Chapter 3 - Chapter 6, it has been observed that the thin films of BTO, STO, and BST-0.5 and the sandwiched Cu nano-layer in between substrate and these films are exhibited RSA in OA *Z*-scan spectra with a cw laser. All those films were deposited on the quartz substrate. The optical nonlinear response can be further enhanced by appropriate selection of the crystalline substrate [227]. All those films reported in the previous chapters having RSA response can be also suitable for optical limiting (OL) response. Optical limiting is a nonlinear optical phenomenon where the transmittance, T, of the thin films is constant with the increase in input laser intensity, then after a certain point the transmittance starts following down [150]. OL is particularly useful in protecting the human eye and delicate optical instruments against intense laser radiations [216, 228]. Therefore, the spotlight of this chapter is on the OL response of thin films of BTO, STO, BST-0.5 and Cu sandwiched nano-layer in these films. The comparison of quartz and MgO substrates on OL response is also presented for these films.

7.1 Experimental details

To investigate the effect of the substrate (quartz and MgO) on OL response of BTO, STO, and BST-0.5 thin films, another two sets of the films were deposited for 180 minutes as per list Table 2-7, Section 2.3, Chapter 2. The deposition parameters for Cu-infused BTO, STO, and BST-0.5 thin films have also been detailed in Section 2.3, Chapter 2. Raman spectra,

UV-Visible-NIR spectra and NLO properties of thin film are desired for these samples in the following section.

7.2 Effect of substrate on BTO, STO, and BST-0.5 thin films

Quartz is an amorphous substrate whereas MgO possess NaCl-type structure (cubic). The lattice constant of MgO is 4.21 Å, while tetragonal BTO (perovskite structure) has lattice constants of a = 3.99 and c = 4.03 Å (determined from Table 3-1). Moreover, the lattice constant of bulk cubic STO (another perovskite structure) is 3.91 Å. The lattice misfit between MgO and tetragonal BTO & cubic STO is 5.2 and 4.4 %, along with a and c-axes & 7.2 % along with a -axis, respectively. Therefore, to compare the properties of thin films of BTO, STO, and BST-0.5 on quartz and MgO substrate each of these were deposited for 180 minutes at optimized 700 °C substrate temperature and 0.1 mbar background oxygen pressure.

7.2.1 Raman analysis for the film deposited for 180 minutes

RT micro-Raman spectra of BTO, STO and BST-0.5 thin films deposited on quartz and MgO substrates recorded in the range of 50 to 900 cm^{-1} are shown in Figure 7-1 (a) - (f).

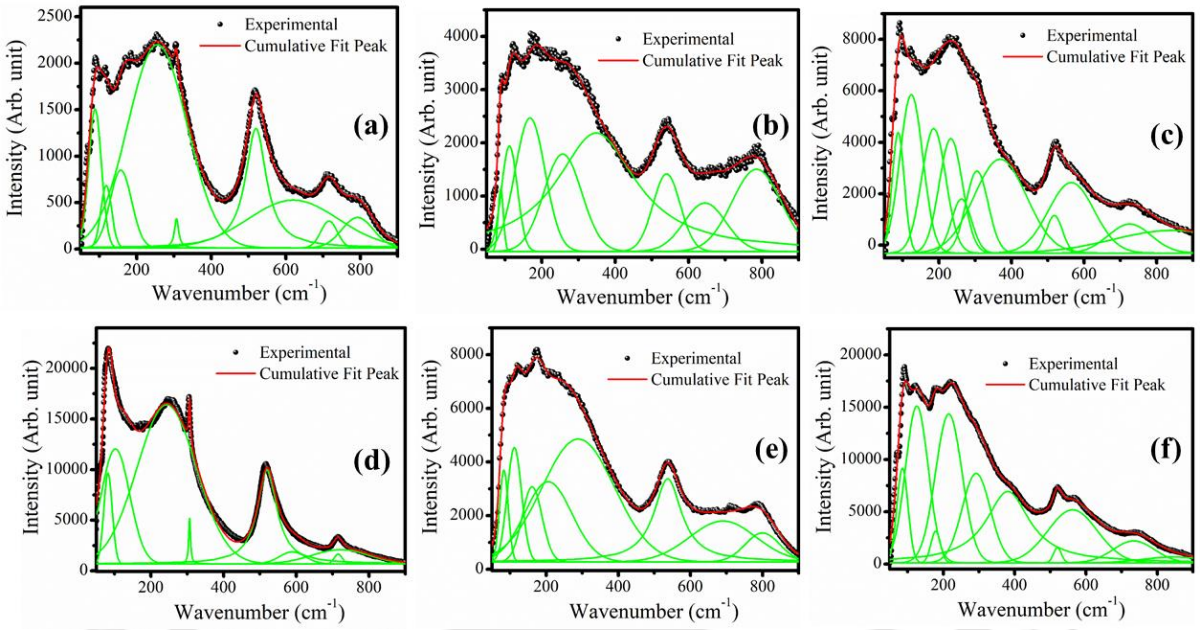

Figure 7-1 *De-convoluted Raman spectra of (a)BTO_Q, (b) STO_Q, (c) BST-0.5_Q, (d) BTO_M,(e) STO_M, and BST-0.5_M thin films deposited for 180 minutes duration.*

Raman spectra consist of multiple peaks and thus, de-convoluted to multiple peaks using Gaussian and Lorentzian line shape. From Raman analysis, it was found that BTO thin film is in a tetragonal structure, whereas the other two films are in cubic crystal symmetry. The peak at 306 cm^{-1} (E(TO+LO)) was observed in the Raman spectrum of BTO film deposited on quartz and MgO substrate, Figure 7-1 (a) and (d), respectively. This peak indicates the tetragonal structure of BTO. It can also be clearly observed from Figure 7-1 (a) that with the increase in deposition time and hence thickness, this peak was more pronounced compared to that of reported in Chapter 4 for one hour deposition Figure 4-13 (a). For the film deposited on MgO substrate, Figure 7-1 (d), this peak was emerged out very distinctly and of very large

intensity as compared to that of quartz. On increasing deposition time, lattice strain present at the interface slowly decreases with increasing film thickness, and films were attaining close to that of bulk properties.

7.2.2 UV-Visible-NIR spectra of BTO, STO and BST-0.5 thin films deposited on quartz and MgO substrates for 180 minutes

In this section, linear optical properties measured from UV-Visible-NIR spectra are reported as these are required for calculating the nonlinear optical absorption and refractive index coefficients. Figure 7-2 shows the transmission spectra of BTO, STO, and BST-0.5 thin films deposited on quartz as well as on MgO substrates. The film shows optical transparency about 75 - 90 % in the visible region. These spectra clearly displayed two regions; one was a strong absorption region, and the other was a transparent but oscillating region due to the multiple beam interface. The spectral transmittance of all thin films shows a strong absorption below 400 nm. Further, it can be seen that the absorption edge of all the films is shifted towards a higher wavelength (lower energy / red shift) for MgO substrate as compared to that of quartz.

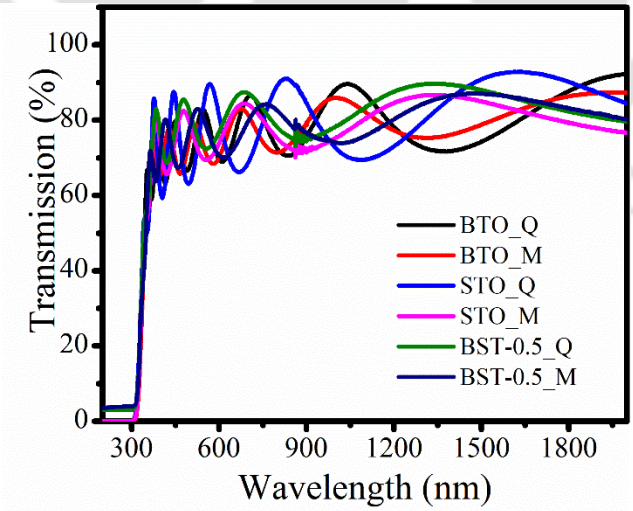

Figure 7-2 *UV-Visible-NIR transmission spectra of BTO, STO, and BST-0.5 thin films deposited on quartz and MgO substrates.*

The fringes are more closely spaced on increasing the deposition time, confirming the increase in thickness with the increase in deposition time. The absorption coefficient and refractive index at λ = 488 nm were calculated from equations (2.6) and (2.3), respectively and shown in Figure 7-3. The values of the refractive index of the films obtained from UV-Visible-NIR spectra were in good agreement with that of refractive bulk crystal [51, 229].

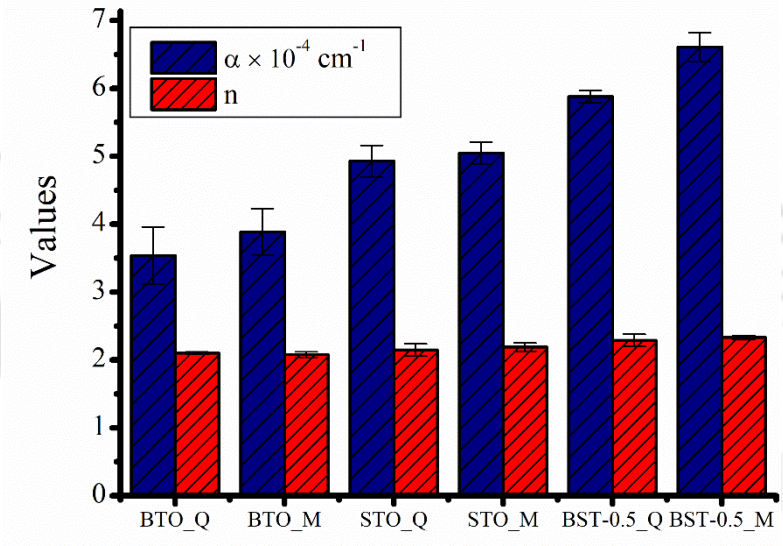

Figure 7-3 *Values of absorption coefficient and refractive index of BTO, STO and BST-0.5 thin films deposited on quartz and MgO substrate.*

Furthermore, the thickness of all these films was obtained from equation (2.4) using the Swanepoel envelope approximation and listed in Table 7-1. The estimated thickness for all these samples found to be 680, 650 and 643 & 730, 692 and 685 nm for BTO, STO, and BST-0.5 films deposited on quartz & MgO substrate, respectively. The increase in film thickness with the deposition time is due to the impingement of more and more ablated target material on the substrate surface. The effect of substrate on the thickness of thin films can be observed for the films deposited on both substrates. It clearly shows films have higher slightly deposition rate on MgO substrate as compared to that of quartz. This could be due to lattice matching on MgO substrate. The bandgap (E_g) of these thin films was determined from equation (2.7),

considering BTO, BST-0.5, and STO thin films being indirect bandgap. The bandgap values were found to be (3.62 ± 0.22), (3.22 ± 0.09), and (3.25 ± 0.12) eV & (3.45 ± 0.08), (3.34 ± 0.17), and (3.42 ± 0.32) eV for BTO, BST-0.5 and STO thin films deposited on MgO & quartz substrates, respectively.

Table 7-1 *Values of thickness, absorption coefficient, bandgap, and refractive index of BTO, STO and BST-0.5 thin films deposited on quartz and MgO substrate.*

Thin film	**Thickness (nm)**	**Absorption coefficient (α) (cm-1) 10^{-4} (at λ = 488 nm)**	**Bandgap (E_g) eV**	**Refractive index (n)**
BTO_Q	680	3.54 ± 0.42	3.62 ± 0.22	2.1 ± 0.02
BTO_M	730	3.89 ± 0.34	3.45 ± 0.08	2.08 ± 0.04
STO_Q	643	4.93 ± 0.23	3.22 ± 0.09	2.15 ± 0.09
STO_M	692	5.05 ± 0.16	3.34 ± 0.17	2.19 ± 0.06
BST-0.5_Q	650	5.88 ± 0.06	3.25 ± 0.12	2.29 ± 0.09
BST-0.5_M	685	6.61± 0.21	3.42 ± 0.32	2.33 ± 0.03

7.2.3 NLO properties of BTO, STO, and BST-0.5 thin films deposited for 180 minutes

Figure 7-4 (a) – (c) & (d) – (f) shows the normalized OA Z-scan plot for the three samples deposited on quartz and MgO substrates along with the data fitted to equation (2.8), Chapter 2. All the films exhibit a transmittance minimum at $z = 0$ in the spectra, suggesting the RSA behavior similar to these of documented in previous chapters. In the present Z-scan measurement, under the cw laser illumination ($\lambda = 488$ nm), the dominant process for the NLO process is due to TPA absorption as all the thin films are satisfying the TPA condition as already discussed in Section 3.3, Chapter 3.

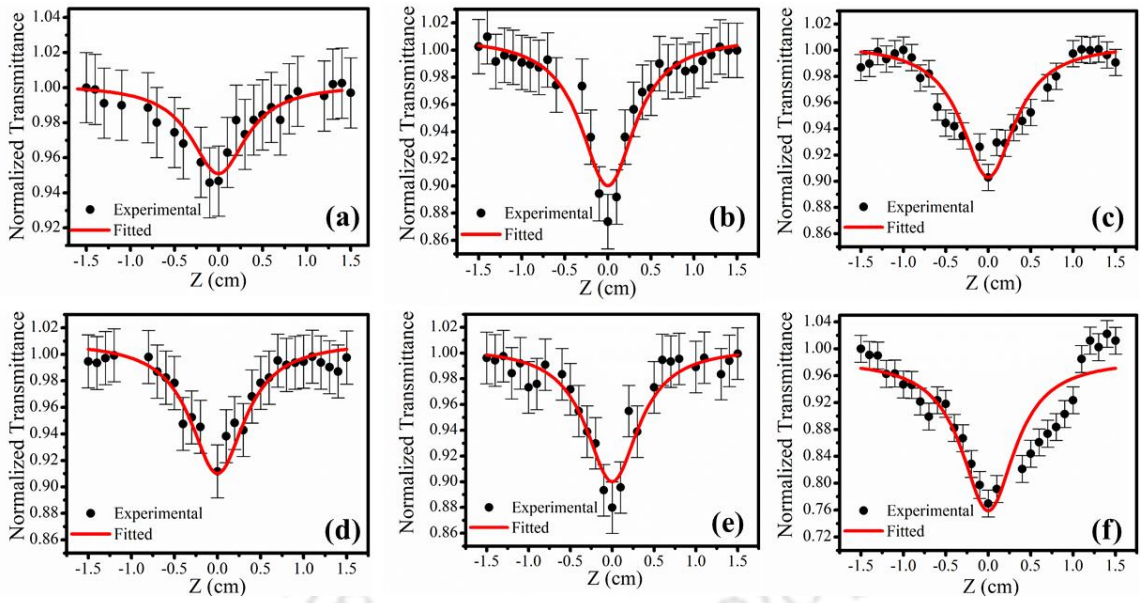

Figure 7-4 *OA Z-scan curves for (a) BTO_Q (b) STO_Q, and (c) BST-0.5_Q thin films & (d) BTO_M, (e) STO_M, and (f) BST-0.5_M thin films.*

Due to the higher thickness all the six films also display CA *Z*-scan behavior. Figure 7-5 (a) – (c) & (d) – (f) shows the normalized CA *Z*-scan plot for the films deposited on quartz and MgO substrates along with the data fitted with equation (2.10), Chapter 2.

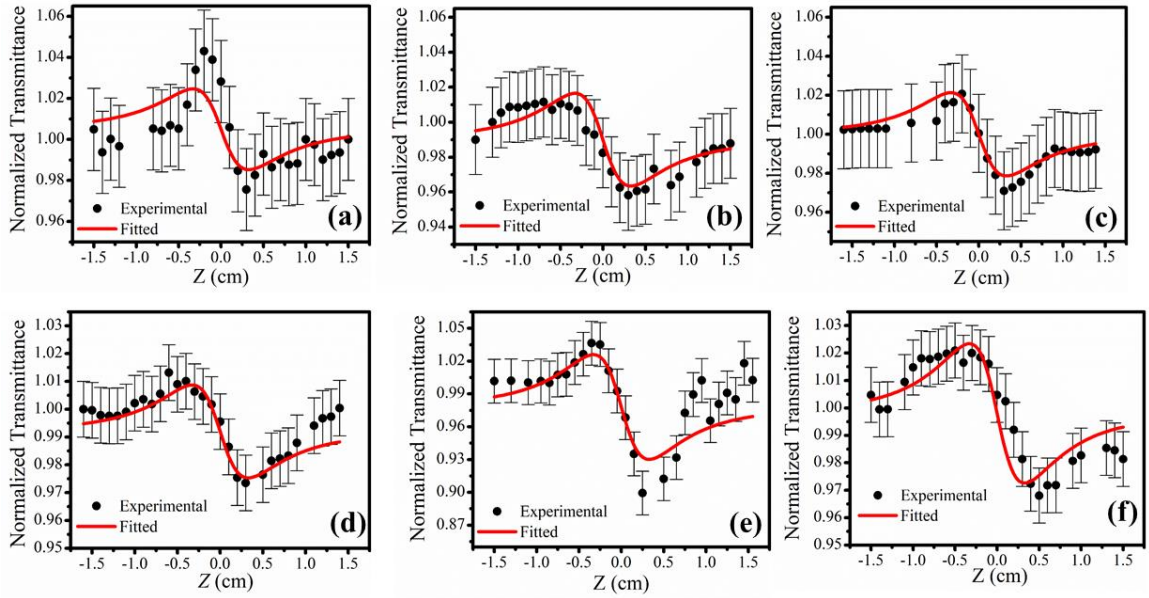

Figure 7-5 *CA Z-scan spectra for (a) BTO_Q (b) STO_Q, and (c) BST-0.5_Q thin films & (d) BTO_M, (e) STO_M, and (f) BST-0.5_M thin films.*

From equation (2.8) and (2.10), the nonlinear coefficient of absorption and refraction were determined and listed in Table 7-2.The values of $\chi^{(3)\prime}$, $\chi^{(3)\prime\prime}$ and $\chi^{(3)}$ were estimated by using the equations (2.15), (2.16), and (2.14), respectively, Chapter 2. The estimated these third-order NLO coefficients, $\chi^{(3)\prime}$ and $\chi^{(3)\prime\prime}$ are also listed in Table 7-2.

Table 7-2 *NLO coefficients (β, n_2, $\chi^{(3)'}$, $\chi^{(3)''}$ and $\chi^{(3)}$) of all thin films deposited on quartz and MgO substrates.*

Thin film	β (cm/W)	n_2 (cm^2/W) x10^{-3}	$\chi^{(3)'}$ (esu) ×10^{-4}	$\chi^{(3)''}$ (esu) ×10^{-4}	$\chi^{(3)}$ (esu) ×10^{-4}
BTO-Q	77.74±0.85	1.66 ± 0.67	41.38±3.32	3.88±0.65	41.56±3.37
BTO-M	85.62±0.07	3.11±1.45	55.38±2.41	4.70±0.25	55.57±2.42
STO-Q	87.57±0.17	3.54±0.38	61.25±2.33	4.48±0.52	61.41±2.36
STO-M	88.03±0.04	4.01±0.14	64.95±3.44	5.63±0.11	65.19±3.43
BST-0.5-Q	91.31±0.13	4.22± 0.21	78.36±6.54	5.13±0.87	78.52±6.58
BST-0.5-M	97.58±0.23	4.81±1.50	78.83±7.52	6.62±0.34	79.10±7.52

All these coefficients were observed to be higher for the films deposited on the MgO substrate as compared to that of quartz. As discussed in Section 6.2.6, Chapter 6, the NLO coefficients are inversely proportional to bandgap energy. Therefore, the NLO coefficients of BST-0.5 and STO thin films are higher than that of BTO films deposited on MgO substrate. But, BST-0.5 thin film has slightly higher absorption coefficient compared to that of STO thin film. Therefore, BST-0.5_M thin film has high nonlinear absorption and refractive index coefficients.

7.2.4 Optical limiting of BTO, STO, and BST-0.5 thin films deposited for 180 minutes

Materials with significant nonlinear RSA can be used as good optical limiters. An ideal optical limiter has a constant values of transmission (I_{out}/I_{in}) below a particular threshold, and above that, it falls down. The OL response of all the films was studied under cw laser

illumination using the set-up shown in Figure 2-8 and as per details in Section 2.4.9, Chapter 2. Figure 7-6 (a) – (b) shows the characteristic OL curves for BTO, STO, and BST-0.5 thin films deposited on quartz substrate & MgO substrate for 180 minutes.

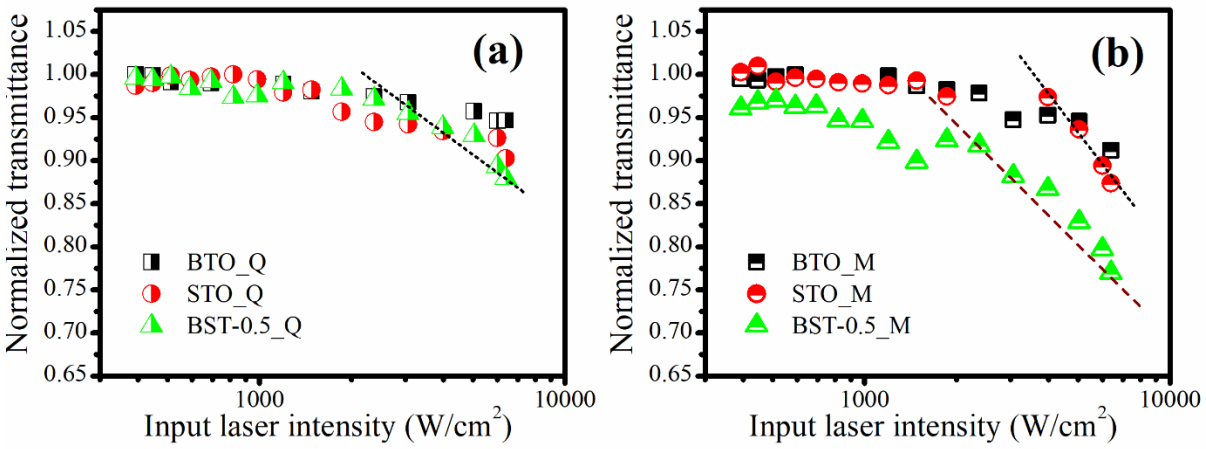

Figure 7-6 *Optical limiting response of (a) BTO_Q, STO_Q, and BST-0.5_Q thin films & (b) BTO_M, STO_M, and BST-0.5_M thin films for 180 minutes duration.*

In the present case, the OL is due to RSA induced by local heating caused by laser absorption in these films. The OL threshold of all thin films was calculated and listed in Table 7-3. It was shown clearly in Figure 7-6 that BST-0.5 thin films have a low OL threshold as it has a maximum β value (Table 7-2). The deviations from the asymptotic behavior (constant normalized T) began at around 3.97 kW/cm^2 for BST-0.5 film deposited on a quartz substrate, but for the film deposited on MgO substrate, threshold was observed at a slightly low value of around 1.85 kW/cm^2 as shown in Table 7-3.

Table 7-3 *Optical limiting threshold of BTO, STO, and BST-0.5 thin films deposited on quartz and MgO substrate.*

Thin film	OL threshold (kW/cm^2)	Thin film	OL threshold (kW/cm^2)
BTO_Q	6	BTO_M	3.97
STO_Q	2.32	STO_M	3.07
BST-0.5_Q	3.97	BST-0.5_M	1.85

7.3 Optical limiting in Cu infused BTO2_1, STO2_1, and BST-0.5_2 thin films

Figure 7-7 (a) and (b) shows optical limiting response of BTO, STO, and BST-0.5_1 & BTO2_1, STO2_1, and BST-0.5_2 thin films deposited on quartz substrate for 60 minutes, respectively.

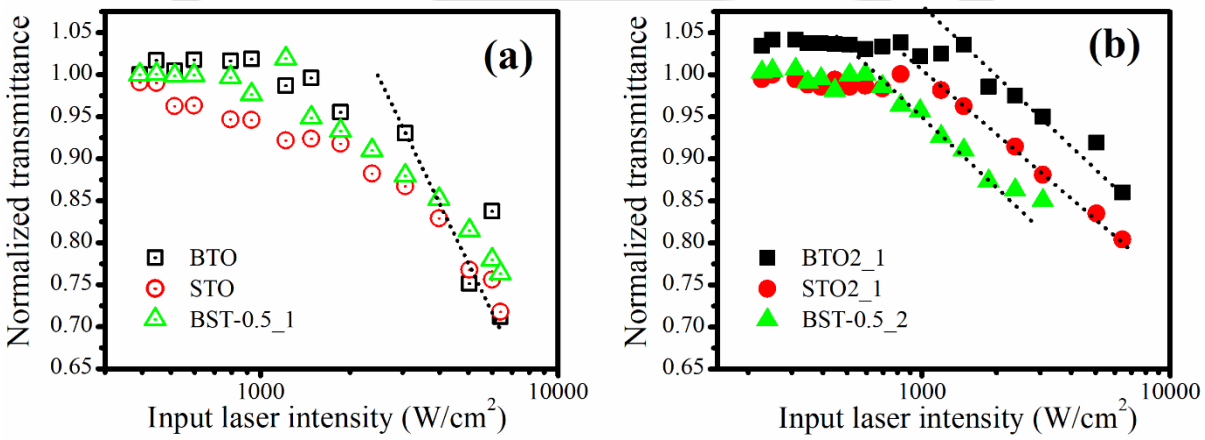

Figure 7-7 *Optical limiting response of (a) BTO, STO, and BST-0.5_1 (b) BTO2_1, STO2_1, and BST-0.5_2 thin films deposited on quartz substrate for 60 minutes duration.*

The OL threshold of all the films was determined from Figure 7-7 and listed in Table 7-4. OL threshold of BST-0.5_1 thin film was minimum as compared to those of other two thin films. For Cu infused samples, BST-0.5_2 thin film also possessed minimum OL threshold

compared that of BTO2_1 and STO2_1 thin films. The OL threshold for all the three system has fallen down in the presence of nano-layer of Cu.

Table 7-4 *Optical limiting threshold of BTO, STO, BST-0.5 and its Cu infused BTO, STO and BST-0.5 thin films deposited for 60 minutes.*

Thin film	**OL threshold (kW/cm^2)**	**Thin film**	**OL threshold (kW/cm^2)**
BTO	1.85	BTO2_1	1.19
STO	1.21	STO2_1	0.82
BST-0.5_1	0.93	BST-0.5_2	0.69

7.4 Conclusions

The influence of the substrate on the linear and nonlinear optical properties of BTO, STO and BST-0.5 thin films deposited for 180 minutes via PLD was investigated. Under cw Ar-Ion laser irradiation, the third-order NLO coefficients of all thin films were analyzed via modified *Z*-scan technique. The thin film of BST-0.5 deposited on the MgO substrate has higher NLO coefficients than that of other two thin films. The NLO coefficients have been obtained to be enhanced on MgO substrate as compared to that of quartz. The OL responses of all the thin films were analyzed. The thin film of BST-0.5 deposited on MgO substrate has an OL threshold of 1.85 kW/cm^2, whereas cu infused BST-0.5_2 thin film deposited on quartz substrate for 60 minutes has an OL threshold of 0.69 kW/cm^2.

Chapter 8 : Conclusions and Future scope

The present research work was aimed towards the fabrication and characterization of BTO, STO and BST thin films via the pulsed laser deposition (PLD) technique. Initially the optimized substrate temperature and background gas pressure as that of the major deposition parameters were attained for the BTO film. Later on all the other thin film of BTO, STO and BST thin films were fabricated all these optimum deposition parameters. The influence of Cu nano-layer on BTO, STO, and BST-0.5 thin films particularly on linear and nonlinear optical properties and PL properties were investigated. Various characterization tools were employed for studying morphology, structural, linear, and nonlinear optical properties. RT PL properties of Cu nano-layer infused BTO thin films, along with their possible origins were investigated. Finally, optical limiting threshold was obtained for the film deposited on quartz and MgO substrates.

BTO thin films were fabricated via PLD technique on a quartz and Si (100) substrates by varying the substrate temperature 400 – 700 °C and oxygen pressure 0.005 -1 mbar. The substrate temperature and oxygen pressure dependence on morphological, linear and nonlinear optical properties of BTO thin films deposited for 60 minutes were studied. EDX analysis also confirmed that BTO film deposited at 700 °C and 0.1 mbar has attained stoichiometry more close to actual stoichiometry of BTO i.e. (Ba:Ti:O :: 1:1:3). Structural properties confirmed that the deposited films fabricated at T_s 400, and 500 °C were amorphous whereas 600, 650, and 700 °C were polycrystalline with pseudocubic phase. Films deposited at various oxygen pressures were also in polycrystalline structures with (110) orientation being the dominating one and in the pseudocubic phase. The Raman peak at 306 cm^{-1} (E (TO+LO)) was not sharp

confirming the pseudocubic phase of thin films. UV-Vis-NIR transmission spectroscopy results were indicating that all films have 75 - 85% optical transparency in the Visible to NIR region. The fluctuation of fringes indicated the good optical quality. The nonlinear absorption coefficients (β) of all the BTO thin films were estimated from the modified Z- scan technique using the cw Ar-Ion laser source (λ = 488 nm). The value of β was found to be increasing with an increase in substrate temperature while increasing with an increase in oxygen pressure till 0.1 mbar and falls down for higher oxygen pressure. By comparing all the results, finally, it was concluded that at the optimum substrate temperature of 700 °C and oxygen pressure of 0.1 mbar for BTO films. This film has a crack-free surface, low roughness (2.93 ± 0.66) nm, more than 80% transparency, and a high β value (57.54±0.05) cm/W.

It is well known fact that the NLO properties can be further enhanced by embedding with metal nanoparticles. Therefore, Cu nano-layer was embedded on BTO thin films at same optimized deposition condition. Three thin films i.e. BTO1, BTO2, and BTO3 were fabricated via the PLD technique on quartz and Si substrates. BTO thin films were deposited for 15 minutes duration whereas Cu thin films were deposited for 3 minutes duration. XRD analysis confirmed that the deposited films were in the pseudocubic phase. The crystallite size of BTO1, BTO2 and BTO3 thin films deposited on Si substrate was 17, 13 and 11 nm, respectively. Moreover, the crystallite size of BTO1, BTO2 and BTO3 thin films deposited on quartz substrate was 16, 12 and 10 nm, respectively. The values of strain of BTO2 and BTO3 thin films was higher than that of BTO1 thin film due to addition of Cu nano-layer. The thickness of the thin films was varying from 50 to 78 nm, which was confirmed from the Profilometer and cross-sectional FESEM analysis. From Raman analysis, it was verified that the films consist of mixed-phase of cubic and tetragonal phases. Raman intensity of BTO2 thin film was

five times higher than BTO1 thin film. The SPR peak was observed at 620 nm in BTO2 thin film which is due to the confinement of Cu-NPs in the vicinity of the high refractive index of the BTO dielectric medium. The nonlinear absorption coefficient estimated from the modified *Z*-scan technique was found to be (7.53± 0.32) cm/W for BTO2 thin film which was higher than that of the other two films. All three films showed broad visible PL spectra from 360 to 600 nm with a 355 nm excitation source. The four-fold enhancement of the PL intensity was observed with the Cu nano-layer sandwiched in between quartz and the BTO film. As, the β value and PL intensity of BTO2 thin film got enhanced more than three times than that of the pure BTO thin film, another BTO2_1 film (here BTO thin film deposited for 60 minutes) was fabricated at the same optimized deposition conditions. With the increase in the deposition time of BTO from 15 minutes to 60 minutes, the β value enhanced drastically from (57.54±0.05) to (155.04 ± 5.39) cm/W and PL intensity of BTO2_1 thin film also increased more than five-fold than that of pristine BTO thin film.

The influence of Cu nano layer on structural, linear, nonlinear optical properties of STO (another perovskite material of same ABO_3 group) thin films was studied. For this, three polycrystalline thin films in three different configurations: pristine STO, Cu nano-layer sandwiched between substrate and STO, and Cu nano-layer on top of STO; STO, STO2_1, and STO3_1 thin films, respectively were fabricated on quartz substrate at the same optimized deposition conditions of BTO. The thickness of the all thin films were measured by Stylus Profilometer and again verified from cross sectional FESEM analysis. The RMS roughness was calculated from AFM analysis and found to be 1.94 ± 1.71 nm for pure STO thin film, increased to 4.57 ± 1.05 nm for STO2_1, and 5.08 ± 1.35 nm for STO3_1 thin film. The XRD and Raman analysis confirmed that these films were in cubic phase. Raman intensity of

STO2_1 film was three times higher than that of STO thin film due to the SERS effect. The PLD thin films of STO1, STO2_1, and STO3_1 were subjected to UV-Vis-NIR spectroscopy to unveil SPR property, the linear absorption coefficient, and band gap energy. The SPR peak appeared at 610 nm wavelength in STO2 configuration. STO nanocomposite thin films were also monitored via modified *Z*-scan measurement to study NLO properties and found to be around three-fold enhancement in STO2_1 thin film (β value = 182.34 cm/W) compared to pristine STO thin film (β value = 63.51 cm/W).

The third set of system, $Ba_{1-x}Sr_xTiO_3$ ($0 \leq x \leq 1$) (BST) thin films were fabricated having around 360 nm thickness via the PLD technique and deposited on quartz and Si substrates. Structural properties confirmed that the deposited BST-0.4, BST-0.5, BST-0.7, and STO thin films were predominately in the cubic phase, whereas BTO and BST-0.3 were in the tetragonal phase. The lattice parameter, density, and crystallite size were decreased with increasing Sr concentration in BST thin films. The optical bandgap of the BST thin films calculated using the Tauc plot was red-shifted from 3.62 ± 0.02 eV (for BTO thin film) to 3.38 ± 0.03 eV (pure STO thin film). The refractive index of BST thin films was decreasing with increasing Sr concentration and it attains minimum for STO thin film. All thin films exhibited absorptive and refractive nonlinearity and exhibited RSA behavior. The values of the third-order nonlinear optical coefficients (β, n_2, $\chi_R^{(3)}$, $\chi_I^{(3)}$ and $\chi^{(3)}$) in $Ba_{1-x}Sr_xTiO_3$ ($0 \leq x \leq 1$) thin films were found to be in the range of (64.74 – 74.85) cm/W, (0.18– 6.35) $\times 10^{-3}$ cm^2/W, (12.37-63.05)$\times 10^{-4}$ esu, (1.23-2.88)$\times 10^{-4}$ esu, and (12.43-63.11) $\times 10^{-4}$ esu, respectively. At optimum Sr concentration (x = 0.5), Cu nano-layer embedded on BST-0.5 thin film fabricated and the nonlinear absorption coefficients of BST-0.5_1 and BST-0.5_2 thin films were found to be (73.24 ± 0.32) and (188 ± 0.45) cm/W, respectively. The film of BST-0.5_2 attains a higher β

value compared to that of BTO2_1 and STO2_1 thin films. The obtained optical parameters regarding linear and NLO properties of BTO, STO, BST-0.5 and their Cu infused thin films are summarized in Table 8-1.

Table 8-1 *Linear and nonlinear optical properties of BTO, STO, BST-0.5 and Cu infused BTO, STO and BST-0.5 thin films.*

Thin Film	**Bandgap (E_g) (eV)**	**Refractive index (n) (at λ = 488 nm)**	**Linear absorption coefficient (α) $\times 10^{-4}$ cm^{-1}**	**Nonlinear absorption coefficient (β) (cm/W)**
BTO	3.70	1.99	5.22	57.54 ± 0.05
STO	3.51	1.93	4.32	63.51 ± 0.13
BST-0.5_1	3.64	1.95	6.43	73.24 ± 0.32
BTO2_1	3.86	-	6.27	155.04 ± 5.39
STO2_1	3.53	-	7.45	182.34 ± 7.23
BST-0.5_2	3.82	-	8.02	188 ± 0.45

The influence of the quartz and MgO substrates on the properties of BTO, STO and BST-0.5 thin films deposited for 180 minutes was investigated. Under a cw Ar-Ion laser irradiation, the third-order NLO coefficients of all these six thin films were analyzed using a modified *Z*-scan technique. The optical limiting (OL) response of all these six thin films were analyzed, and OL threshold values were derived using the OL curve. BST-0.5_1 thin film deposited on MgO substrate has an OL threshold of 1.85 kW/cm^2, whereas BST-0.5_2 thin film deposited on quartz substrate for 60 minutes has an OL threshold of 0.69 kW/cm^2. The obtained linear and nonlinear optical parameters are listed in Table 8-2.

Table 8-2 *Linear and nonlinear optical properties of BTO_Q, BTO_M, STO_Q, STO_M, BST-0.5_Q, and BST-0.5_M thin films.*

Thin film	Bandgap (E_g) (eV)	Linear absorption coefficient (α) × 10^{-4} cm^{-1}	Nonlinear absorption coefficient (β) (cm/W)	Nonlinear refractive index coefficient (n_2) (cm^2/W) × 10^{-3}	$\chi^{(3)}$ (esu) × 10^{-4}
BTO_Q	3.62	3.54	77.74 ± 0.85	1.66 ± 0.67	41.56±3.37
BTO_M	3.45	3.89	85.62 ± 0.07	3.11±1.45	55.57±2.42
STO_Q	3.42	4.93	87.57 ± 0.17	3.54±0.38	61.41±2.36
STO_M	3.22	5.05	88.03 ± 0.04	4.01±0.14	65.19±3.43
BST-0.5_Q	3.34	5.88	91.31 ± 0.13	4.22± 0.21	78.52±6.58
BST-0.5_M	3.25	6.61	97.58 ± 0.23	4.81±1.50	79.10±7.52

Future scopes

The heterostructure of BTO/STO or STO/BTO and BTO/BST-0.5/STO thin films can be fabricated via PLD technique, and metal particles can be infused on these structures and for the plasmonic and nonlinear optical properties.

The films of BTO exhibiting photoluminescence can be subjected to time-resolved PL and temperature dependent PL studies for further detailed understanding of the possible emission mechanisms involved. Moreover, STO and BST thin films can be examined for RT PL study along with time resolved and temperature dependent PL study.

The third order optical nonlinearity of Cu nano-layer sandwiched BTO, STO and BST-0.5 thin films was reported in this thesis. The similar studies are to be taken up for Ag and Au noble metals instead of Cu and study its effects on linear and nonlinear optical properties via cw, nanosecond and femtosecond laser.

BST thin films are regarded as a new lead free material for electro-optic (EO) modulators as it has relatively high EO coefficient compared to BTO and STO thin films as reported in the literature. These studies will be undertaken for future.

Bibliography

[1] J. Jana, M. Ganguly, T. Pal, Enlightening surface plasmon resonance effect of metal nanoparticles for practical spectroscopic application, *RSC advances*, **6** (2016) 86174-86211.

[2] A. Parretta, M. Jayaraj, A. Di Nocera, S. Loreti, L. Quercia, A. Agati, Electrical and optical properties of copper oxide films prepared by reactive RF magnetron sputtering, *physica status solidi (a)*, **155** (1996) 399-404.

[3] G. Hai-Zhong, L. Li-Feng, L. Hui-Bin, F. Yi-Yan, X. Wen-Feng, Z. Yue-Liang, C. Zheng-Hao, Structure, electrical, and optical properties of Nb-doped BaTiO3 thin films grown by laser molecular beam epitaxy, *Chinese Physics Letters*, **21** (2004) 396.

[4] S. Behera, A. Khare, Tuning of optical properties of Cu doped BTO thin films fabricated by PLD Technique, *2019 Workshop on Recent Advances in Photonics (WRAP)*, (2019) 1-3.

[5] R. Ganeev, A. Ryasnyansky, A. Stepanov, T. Usmanov, Saturated absorption and reverse saturated absorption of Cu: SiO2 at λ= 532 nm, *physica status solidi (b)*, **241** (2004) R1-R4.

[6] A. Spetanov, Nonlinear optical properties of implanted metal nanoparticales in various transparent matrixes, *Rev. Adv. Mater. Sci*, **27** (2011) 115.

[7] W. Wang, L. Qu, G. Yang, Z. Chen, Large third-order optical nonlinearity in BaTiO3 matrix-embedded metal nanoparticles, *Applied surface science*, **218** (2003) 24-28.

[8] S. Zhang, B. Zhang, S. Li, X. Li, Z. Huang, SPR enhanced photocatalytic properties of Au-dispersed amorphous BaTiO3 nanocomposite thin films, *Journal of Alloys and Compounds*, **654** (2016) 112-119.

[9] T. Ning, C. Chen, Y. Zhou, H. Lu, H. Shen, D. Zhang, P. Wang, H. Ming, G. Yang, Third-order optical nonlinearity of gold nanoparticle arrays embedded in a BaTiO 3 matrix, *Applied optics*, **48** (2009) 375-379.

[10] H. Lu, W.J.A.o. Wang, Picosecond nonlinear optical properties of SrTiO 3 composite films doped with gold and nickel nanoparticles, **56** (2017) 4690-4694.

[11] G. Yang, H. Wang, G. Tan, A. Jiang, Y. Zhou, Z.J.A.o. Chen, Rh: BaTiO 3 thin films with large nonlinear optical properties, **41** (2002) 1729-1732.

[12] W. Wei-Tian, Y. Guang, D. Ping, Z. Yue-Liang, C.J.C.p.l. Zheng-Hao, Fe-doped BaTiO3 thin films with large third-order nonlinear optical susceptibility, **19** (2002) 1122.

[13] R. Kesarwani, A. Khare, Surface plasmon resonance and nonlinear optical behavior of pulsed laser-deposited semitransparent nanostructured copper thin films, *Applied Physics B*, **124** (2018) 1-8.

[14] B.G. Yust, N. Razavi, F. Pedraza, Z. Elliott, A.T. Tsin, D.K. Sardar, Enhancement of nonlinear optical properties of BaTiO 3 nanoparticles by the addition of silver seeds, *Optics express*, **20** (2012) 26511-26520.

[15] J. Zhang, L. Zhang, W. Xu, Surface plasmon polaritons: physics and applications, *Journal of Physics D: Applied Physics*, **45** (2012) 113001.

[16] H. Raether, Surface plasmons on gratings, in: Surface plasmons on smooth and rough surfaces and on gratings, Springer, 1988, pp. 91-116.

[17] F. Hache, D. Ricard, C. Flytzanis, Optical nonlinearities of small metal particles: surface-mediated resonance and quantum size effects, *JOSA B*, **3** (1986) 1647-1655.

[18] F. Hache, D. Ricard, C. Flytzanis, U. Kreibig, The optical Kerr effect in small metal particles and metal colloids: the case of gold, *Applied Physics A*, **47** (1988) 347-357.

[19] Y. Zhu, X. Hu, Y. Fu, H. Yang, Q. Gong, Ultralow-power and ultrafast all-optical tunable plasmon-induced transparency in metamaterials at optical communication range, *Scientific reports*, **3** (2013) 1-7.

[20] E. Ozbay, Plasmonics: merging photonics and electronics at nanoscale dimensions, *science*, **311** (2006) 189-193.

[21] R. Zia, J.A. Schuller, A. Chandran, M.L. Brongersma, Plasmonics: the next chip-scale technology, *Materials today*, **9** (2006) 20-27.

[22] S.A. Maier, H.A. Atwater, Plasmonics: Localization and guiding of electromagnetic energy in metal/dielectric structures, *Journal of applied physics*, **98** (2005) 10.

[23] C. Flytzanis, F. Hache, M. Klein, D. Ricard, P. Roussignol, V Nonlinear Optics in Composite Materials: 1. Semiconductor and Metal Crystallites in Dielectrics: 1. Semiconductor and Metal Crystallites in Dielectrics, *Progress in optics*, **29** (1991) 321-411.

[24] R. Serna, C.N. Afonso, J. Ballesteros, A. Naudon, D. Babonneau, A. Petford-Long, Size, shape anisotropy, and distribution of Cu nanocrystals prepared by pulsed laser deposition, *Applied surface science*, **138** (1999) 1-5.

[25] A.N. Koya, X. Zhu, N. Ohannesian, A.A. Yanik, A. Alabastri, R. Proietti Zaccaria, R. Krahne, W.-C. Shih, D. Garoli, Nanoporous Metals: From Plasmonic Properties to Applications in Enhanced Spectroscopy and Photocatalysis, *ACS nano*, **15** (2021) 6038-6060.

[26] S.A.M. Ealia, M. Saravanakumar, A review on the classification, characterisation, synthesis of nanoparticles and their application, *IOP Conference Series: Materials Science and Engineering*, **263** (2017) 032019.

[27] Y. Gao, D. Kong, Nonlinear optical response of noble metal nanoparticles, *Laser Technology and its Applications*, (2019) 43.

[28] M.B. Gawande, A. Goswami, F.-X. Felpin, T. Asefa, X. Huang, R. Silva, X. Zou, R. Zboril, R.S. Varma, Cu and Cu-Based Nanoparticles: Synthesis and Applications in Catalysis, *Chemical Reviews*, **116** (2016) 3722-3811.

[29] A.M. Ealias, M.P. Saravanakumar, A review on the classification, characterisation, synthesis of nanoparticles and their application, *IOP Conference Series: Materials Science and Engineering*, **263** (2017) 032019.

[30] J. Niittynen, E. Sowade, H. Kang, R.R. Baumann, M. Mäntysalo, Comparison of laser and intense pulsed light sintering (IPL) for inkjet-printed copper nanoparticle layers, *Scientific reports*, **5** (2015) 8832.

[31] A.A. Rakhmetova, T.P. Alekseeva, O.A. Bogoslovskaya, I.O. Leipunskii, I.P. Ol'khovskaya, A.N. Zhigach, N.N. Glushchenko, Wound-healing properties of copper nanoparticles as a function of physicochemical parameters, *Nanotechnologies in Russia*, **5** (2010) 271-276.

[32] J. Bhattacharya, U. Choudhuri, O. Siwach, P. Sen, A.K. Dasgupta, Interaction of hemoglobin and copper nanoparticles: implications in hemoglobinopathy, *Nanomedicine: Nanotechnology, Biology and Medicine*, **2** (2006) 191-199.

[33] R.K. Sahu, S.H. Somashekhar, P.V. Manivannan, Investigation on Copper Nanofluid Obtained through Micro Electrical Discharge Machining for Dispersion Stability and Thermal Conductivity, *Procedia Engineering*, **64** (2013) 946-955.

[34] S. Dhara, Surface Plasmon Polariton Assisted Optical Switching in Noble Metal Nanoparticle Systems: A Sub-Band Gap Approach, in: Reviews in Plasmonics 2015, Springer, 2016, pp. 1-17.

[35] M. Acosta, N. Novak, V. Rojas, S. Patel, R. Vaish, J. Koruza, G. Rossetti Jr, J. Rödel, BaTiO3-based piezoelectrics: Fundamentals, current status, and perspectives, *Applied Physics Reviews*, **4** (2017) 041305.

[36] W. Zhang, Y. Huang, M. Zhang, Z. Liu, Nonlinear optical absorption in undoped and cerium-doped BaTiO 3 thin films using Z-scan technique, *Applied Physics Letters*, **76** (2000) 1003-1005.

[37] M.-H.M. Hsu, A. Marinelli, C. Merckling, M. Pantouvaki, J. Van Campenhout, P. Absil, D. Van Thourhout, Orientation-dependent electro-optical response of BaTiO 3 on SrTiO 3-buffered Si (001) studied via spectroscopic ellipsometry, *Optical Materials Express*, **7** (2017) 2030-2039.

[38] C. Randall, R. Newnham, L. Cross, History of the first ferroelectric oxide, BaTiO3, *Materials Research Institute, The Pennsylvania State University, University Park, Pa, USA*, **1** (2004).

[39] Z. Cheng, J. Lin, Layered organic–inorganic hybrid perovskites: structure, optical properties, film preparation, patterning and templating engineering, *CrystEngComm*, **12** (2010) 2646-2662.

[40] T.E. Warner, *Synthesis, properties and mineralogy of important inorganic materials*, John Wiley & Sons, 2012.

[41] W.J. Merz, Switching time in ferroelectric BaTiO3 and its dependence on crystal thickness, *Journal of Applied Physics*, **27** (1956) 938-943.

[42] A. Mackenzie, S. Julian, A. Diver, G. McMullan, M. Ray, G. Lonzarich, Y. Maeno, S. Nishizaki, T. Fujita, Quantum Oscillations in the Layered Perovskite Superconductor S r 2 Ru O 4, *Physical review letters*, **76** (1996) 3786.

[43] H. Asano, J. Hayakawa, M. Matsui, Preparation and properties of triple perovskite La 3− 3x Ca 1+ 3x Mn 3 O 10 ferromagnetic thin films, *Applied physics letters*, **71** (1997) 844-846.

[44] A. Karvounis, F. Timpu, V.V. Vogler-Neuling, R. Savo, R. Grange, Barium titanate nanostructures and thin films for photonics, *Advanced Optical Materials*, **8** (2020) 2001249.

[45] D. Tenne, A. Soukiassian, X. Xi, H. Choosuwan, R. Guo, A. Bhalla, Lattice dynamics in Ba x Sr 1− x Ti O 3 thin films studied by Raman spectroscopy, *Journal of applied physics*, **96** (2004) 6597-6605.

[46] E. Chernova, O. Pacherova, D. Chvostova, A. Dejneka, T. Kocourek, M. Jelinek, M. Tyunina, Strain-controlled optical absorption in epitaxial ferroelectric BaTiO3 films, *Applied Physics Letters*, **106** (2015) 192903.

[47] L.-z. Xuan, S.-h. Pan, Z.-h. Chen, R.-p. Wang, W.-s. Shi, C.-l. Li, Second-harmonic generation in BaTiO 3 films doped with cerium, *Applied physics letters*, **73** (1998) 2896-2898.

[48] A. Brignon, S. Breugnot, J.-P. Huignard, Very high-gain two-wave mixing in BaTiO 3 with a self-bent pump beam, *Optics letters*, **20** (1995) 1689-1691.

[49] S. Kumari, A. Khare, Effect of Pump Intensity on Slowing Down of Light in ${\rm Ce {:} BaTiO} _ {3} $ Crystal via Degenerate Two-Wave Mixing Using Chopped Pulses, *IEEE Journal of Quantum Electronics*, **47** (2011) 972-976.

[50] I.-D. Kim, Y. Avrahami, L. Socci, F. Lopez-Royo, H.L. Tuller, Ridge waveguide using highly oriented BaTiO3 thin films for electro-optic application, *Journal of Asian Ceramic Societies*, **2** (2014) 231-234.

[51] T. Supasai, S. Dangtip, P. Learngarunsri, N. Boonyopakorn, A. Wisitsoraat, S.K. Hodak, Influence of temperature annealing on optical properties of SrTiO3/BaTiO3 multilayered films on indium tin oxide, *Applied surface science*, **256** (2010) 4462-4467.

[52] Ľ. Scholtz, P. Šutta, P. Calta, P. Novák, M. Solanská, J. Müllerová, Investigation of barium titanate thin films as simple antireflection coatings for solar cells, *Applied Surface Science*, **461** (2018) 249-254.

[53] S.-H. Yoon, H. Kim, Effect of donor (Nb) concentration on the bulk electrical resistivity of Nb-doped barium titanate, *Journal of applied physics*, **92** (2002) 1039-1047.

[54] J.Q. Qi, W.P. Chen, Y. Wang, H.L.W. Chan, L.T. Li, *Dielectric properties of barium titanate ceramics doped by B 2 O 3 vapor*, in, American Institute of Physics, 2004.

[55] A. Fasasi, M. Maaza, E. Rohwer, D. Knoessen, C. Theron, A. Leitch, U. Buttner, Effect of Zn-doping on the structural and optical properties of BaTiO3 thin films grown by pulsed laser deposition, *Thin Solid Films*, **516** (2008) 6226-6232.

[56] Z. Fu, B.K. Moon, H.K. Yang, J.H. Jeong, Synthesis, characterization, and luminescent properties of Pr3+-doped bulk and nanocrystalline BaTiO3 phosphors, *The Journal of Physical Chemistry C*, **112** (2008) 5724-5728.

[57] A.E. Souza, S.R. Teixeira, C. Morilla-Santos, W.H. Schreiner, P.N. Lisboa Filho, E. Longo, Photoluminescence activity of Ba 1− x Ca x TiO 3: dependence on particle size and morphology, *Journal of Materials Chemistry C*, **2** (2014) 7056-7070.

[58] F.A. Rabuffetti, S.P. Culver, J.S. Lee, R.L. Brutchey, Local structural investigation of Eu 3+-doped BaTiO 3 nanocrystals, *Nanoscale*, **6** (2014) 2909-2914.

[59] J. Hao, Y. Zhang, X. Wei, Electric-induced enhancement and modulation of upconversion photoluminescence in epitaxial BaTiO3: Yb/Er thin films, *Angewandte Chemie International Edition*, **50** (2011) 6876-6880.

[60] H. Zhan, X. Jiang, M. Zhu, X. Li, Z. Luo, K. Shu, Photoluminescence activity of BaTiO3 nanocrystals dependence on the structural evolution, *Journal of Crystal Growth*, **433** (2016) 80-85.

[61] V. Rivera, I. Nogueira, E. Leite, M. Pereira-da-Silva, M.S. Li, E. Marega Jr, Effects of defects, grain size, and thickness on the optical properties of BaTiO3 thin films, *Journal of Luminescence*, **192** (2017) 969-974.

[62] M. Arya, S. Kumar, D. Hasina, S. Ojha, A. Arora, V.K. Malik, A. Mitra, T. Som, S. Dhar, Ta-doped SrTiO3 epitaxial thin film: A promising perovskite for optoelectronics, *Journal of Applied Physics*, **129** (2021) 145109.

[63] W. Lin, T.-Y. Tseng, H. Lu, S. Tu, S. Yang, I. Lin, Growth and ferroelectricity of epitaxial-like BaTiO3 films on single-crystal MgO, SrTiO3, and silicon substrates synthesized by pulsed laser deposition, *Journal of applied physics*, **77** (1995) 6466-6471.

[64] H. Gao, W. Peng, X. Zhu, T. Hu, X. Xie, J. Zhu, Epitaxial growth and transport properties of BaTiO3/LaAlO3/SrTiO3 heterostructures, *Ceramics International*, **40** (2014) 13763-13769.

[65] H. Tabata, H. Tanaka, T. Kawai, Formation of artificial BaTiO3/SrTiO3 superlattices using pulsed laser deposition and their dielectric properties, *Applied physics letters*, **65** (1994) 1970-1972.

[66] J. Hiltunen, M. Karppinen, P. Karioja, J. Lappalainen, J. Puustinen, V. Lantto, H.L. Tuller, Electro-optical properties of BaTiO3-SrTiO3 multilayer thin films for waveguide modulators, *Silicon Photonics and Photonic Integrated Circuits*, **6996** (2008) 69960H.

[67] Y. Deng, Y. Du, M. Zhang, J. Han, Z. Yin, Nonlinear optical properties in SrTiO3 thin films by pulsed laser deposition, *Solid state communications*, **135** (2005) 221-225.

[68] H. Lu, W. Wang, Picosecond nonlinear optical properties of SrTiO 3 composite films doped with gold and nickel nanoparticles, *Applied optics*, **56** (2017) 4690-4694.

[69] G. Wang, Y. Zhang, C. Mao, X. Dong, J. Chu, Composition dependence of structural and optical properties for sol-gel derived (100)-oriented Ba 1− x Sr x Ti O 3 thin films, *Applied Physics Letters*, **91** (2007) 061104.

[70] T.S. Kim, M.H. Oh, C.H. Kim, Influences of indium tin oxide layer on the properties of RF magnetron-sputtered (BaSr) TiO3 thin films on indium tin oxide-coated glass substrate, *Japanese journal of applied physics*, **32** (1993) 2837.

[71] D.-Y. Kim, S.E. Moon, E.-K. Kim, S.-J. Lee, J.-J. Choi, H.-E. Kim, Electro-optic characteristics of (001)-oriented Ba 0.6 Sr 0.4 TiO 3 thin films, *Applied physics letters*, **82** (2003) 1455-1457.

[72] E. Mishina, N. Sherstyuk, V. Stadnichuk, A. Sigov, V. Mukhorotov, Y.I. Golovko, A. Van Etteger, T. Rasing, Nonlinear-optical probing of nanosecond ferroelectric switching, *Applied physics letters*, **83** (2003) 2402-2404.

[73] P. Shi, X. Yao, L. Zhang, X. Wu, M. Wang, X. Wan, Third-order optical nonlinearity of (Ba0. 7Sr0. 3) TiO3 ferroelectric thin films fabricated by soft solution processing, *Solid state communications*, **134** (2005) 589-593.

[74] S. Liu, J. Xu, D. Guzun, G. Salamo, C. Chen, Y. Lin, M. Xiao, Nonlinear optical absorption and refraction of epitaxial Ba 0.6 Sr 0.4 TiO 3 thin films on (001) MgO substrates, *Applied Physics B*, **82** (2006) 443-447.

[75] W. Wang, Z. Dai, Y. Sun, Y. Sun, D. Guan, Picosecond nonlinear optical response of Ba0. 5Sr0. 5TiO3 thin films fabricated by pulsed laser deposition, *Applied surface science*, **250** (2005) 268-272.

[76] K.V. Saravanan, K.J. Raju, M.G. Krishna, S.P. Tewari, S.V. Rao, Large three-photon absorption in Ba 0.5 Sr 0.5 TiO 3 films studied using Z-scan technique, *Applied Physics Letters*, **96** (2010) 232905.

[77] L.H. Parker, A.F. Tasch, Ferroelectric materials for 64 Mb and 256 Mb DRAMS, *IEEE Circuits and Devices Magazine*, **6** (1990) 17-26.

[78] G. Niu, S. Yin, G. Saint-Girons, B. Gautier, P. Lecoeur, V. Pillard, G. Hollinger, B. Vilquin, Epitaxy of BaTiO3 thin film on Si (0 0 1) using a SrTiO3 buffer layer for non-volatile memory application, *Microelectronic Engineering*, **88** (2011) 1232-1235.

[79] Y. Guo, M. Li, W. Zhao, D. Akai, K. Sawada, M. Ishida, M. Gu, Ferroelectric and pyroelectric properties of (Na0. 5Bi0. 5) TiO3–BaTiO3 based trilayered thin films, *Thin Solid Films*, **517** (2009) 2974-2978.

[80] A. Petraru, J. Schubert, M. Schmid, C. Buchal, Ferroelectric BaTiO 3 thin-film optical waveguide modulators, *Applied Physics Letters*, **81** (2002) 1375-1377.

[81] D. Fuchs, C. Schneider, R. Schneider, H. Rietschel, High dielectric constant and tunability of epitaxial SrTiO 3 thin film capacitors, *Journal of Applied Physics*, **85** (1999) 7362-7369.

[82] S.G. Manavalan, A. Kumar, T. Weller, A. Sikder, Structural and electrical properties of Ba0. 5Sr0. 5TiO3 thin films for tunable microwave applications, *MRS Online Proceedings Library (OPL)*, **811** (2004).

[83] T. Hara, T. Ishiguro, Oxygen sensitivity of SrTiO3 thin film prepared using atomic layer deposition, *Sensors and Actuators B: Chemical*, **136** (2009) 489-493.

[84] J. Gao, D. Xue, W. Liu, C. Zhou, X. Ren, Recent progress on BaTiO3-based piezoelectric ceramics for actuator applications, *Actuators*, **6** (2017) 24.

[85] M. Klee, H. Boots, B. Kumar, C. Van Heesch, R. Mauczok, W. Keur, M. De Wild, H. Van Esch, A. Roest, K. Reimann, Ferroelectric and piezoelectric thin films and their applications for integrated capacitors, piezoelectric ultrasound transducers and piezoelectric switches, *IOP Conference Series: Materials Science and Engineering*, **8** (2010) 012008.

[86] J. Li, S. Li, F. Liu, M. Alim, G. Chen, The origin of varistor property of SrTiO 3-based ceramics, *Journal of Materials Science: Materials in Electronics*, **14** (2003) 483-486.

[87] L. Pellegrino, I. Pallecchi, D. Marre, E. Bellingeri, A. Siri, Fabrication of submicron-scale SrTiO 3− δ devices by an atomic force microscope, *Applied physics letters*, **81** (2002) 3849-3851.

[88] N. Bodenmüller, *Cation nonstoichiometry in SrTiO3 based solid oxide solar cells*, in, Wien, 2020.

[89] H. Ohta, Thermoelectrics based on strontium titanate, *Materials today*, **10** (2007) 44-49.

[90] S. Mseddi, A. Njeh, D. Schneider, H. Fuess, M. Hédi Ben Ghozlen, X-ray diffraction and surface acoustic wave analysis of BST/Pt/TiO2/SiO2/Si thin films, *Journal of Applied Physics*, **110** (2011) 104506.

[91] K. Jim, D. Wang, C.W. Leung, C. Choy, H.L. Chan, One-dimensional tunable ferroelectric photonic crystals based on Ba 0.7 Sr 0.3 TiO 3/MgO multilayer thin films, *Journal of applied physics*, **103** (2008) 083107.

[92] G.Z. Mashanovich, Optical switches and modulators in deep freeze, *Nature Materials*, **19** (2020) 1135-1136.

[93] J. Nath, D. Ghosh, J. Maria, M. Steer, A. Kingon, G.T. Stauf, Microwave properties of BST thin film interdigital capacitors on low cost alumina substrates, *34th European Microwave Conference, 2004.*, **3** (2004) 1497-1500.

[94] M. Imran, R. Ahmad, N. Afzal, M. Rafique, Copper ion implantation effects in ZnO film deposited on flexible polymer by DC magnetron sputtering, *Vacuum*, **165** (2019) 72-80.

[95] Y. Yang, J. Shi, W. Huang, S. Dai, L. Wang, Preparation and optical properties of gold nanoparticles embedded in barium titanate thin films, *Journal of materials science*, **38** (2003) 1243-1248.

[96] M. Suja, S.B. Bashar, M.M. Morshed, J. Liu, Realization of Cu-doped p-type ZnO thin films by molecular beam epitaxy, *ACS Applied materials & interfaces*, **7** (2015) 8894-8899.

[97] J.-S. Kim, K.-S. Lee, S.S. Kim, Third-order optical nonlinearity of Cu nanoparticle-dispersed Ba0. 5Sr0. 5TiO3 films prepared by alternating pulsed laser deposition, *Thin Solid Films*, **515** (2006) 2332-2336.

[98] H.M. Smith, A. Turner, Vacuum deposited thin films using a ruby laser, *Applied Optics*, **4** (1965) 147-148.

[99] I.-T. Kim, C.-H. Lee, S.J. Park, Preparation of BaTiO3 thin films by metalorganic chemical vapor deposition using ultrasonic spraying, *Japanese journal of applied physics*, **33** (1994) 5125.

[100] T. Hosokura, A. Ando, T. Konoike, Orientation-controlled BaTiO 3 thin films fabricated by chemical solution deposition, *RSC Advances*, **5** (2015) 97563-97567.

[101] R. Thomas, D. Dube, M. Kamalasanan, S. Chandra, Optical and electrical properties of BaTiO3 thin films prepared by chemical solution deposition, *Thin solid films*, **346** (1999) 212-225.

[102] R. Ashiri, A. Nemati, M.S. Ghamsari, Crack-free nanostructured BaTiO3 thin films prepared by sol–gel dip-coating technique, *Ceramics International*, **40** (2014) 8613-8619.

[103] H. Zhang, C. Kam, Y. Zhou, X. Han, Y. Lam, Y. Chan, K. Pita, Optical and electrical properties of sol–gel derived BaTiO3 films on ITO coated glass, *Materials chemistry and physics*, **63** (2000) 174-177.

[104] X. Han, C. Kam, S. Cheng, Y. Zhou, H. Zhang, K. Pita, Y. Chan, Y. Lam, Ferroelectric properties of SOL-GEL derived thin solid film of barium titanate on ITO-glass, *Integrated Ferroelectrics*, **33** (2001) 221-226.

[105] Y.V. Reddy, D. Mergel, S. Reuter, V. Buck, M. Sulkowski, Structural and optical properties of BaTiO3 thin films prepared by radio-frequency magnetron sputtering at various substrate temperatures, *Journal of Physics D: Applied Physics*, **39** (2006) 1161.

[106] A. Ianculescu, B. Despax, V. Bley, T. Lebey, R. Gavrilă, N. Drăgan, Structure–properties correlations for barium titanate thin films obtained by rf-sputtering, *Journal of the European Ceramic Society*, **27** (2007) 1129-1135.

[107] D.J. Appleby, N.K. Ponon, K.S. Kwa, S. Ganti, U. Hannemann, P.K. Petrov, N.M. Alford, A. O'Neill, Ferroelectric properties in thin film barium titanate grown using pulsed laser deposition, *Journal of Applied Physics*, **116** (2014) 124105.

[108] S. Canulescu, G. Dinescu, G. Epurescu, D. Matei, C. Grigoriu, F. Craciun, P. Verardi, M. Dinescu, Properties of BaTiO3 thin films deposited by radiofrequency beam discharge assisted pulsed laser deposition, *Materials Science and Engineering: B*, **109** (2004) 160-166.

[109] E. Enriquez, D. Shreiber, S. Hirsch, C. Hubbard, E. Ngo, M. Cole, *Optimization of Strontium Titanate (SrTiO3) Thin Films Fabricated by Metal Organic Chemical Vapor Deposition (MOCVD) for Microwave-Tunable Devices*, in, ARMY RESEARCH LAB ABERDEEN PROVING GROUND MD ABERDEEN PROVING GROUND, 2015.

[110] F. Pontes, E. Leite, E. Lee, E. Longo, J.A. Varela, Preparation, microstructural and electrical characterization of SrTiO3 thin films prepared by chemical route, *Journal of the European Ceramic Society*, **21** (2001) 419-426.

[111] D. Bao, H. Yang, L. Zhang, X. Yao, Structure and optical properties of SrTiO3 thin films prepared by a sol–gel technique, *physica status solidi (a)*, **169** (1998) 227-233.

[112] K. Radhakrishnan, C. Tan, H. Zheng, G. Ng, Preparation and characterization of rf-sputtered SrTiO 3 thin films, *Journal of Vacuum Science & Technology A: Vacuum, Surfaces, and Films*, **18** (2000) 1638-1641.

[113] D. Su, T. Yamada, R. Gysel, A.K. Tagantsev, P. Muralt, N. Setter, N. Jiang, Growth-mode induced defects in epitaxial SrTiO3 thin films grown on single crystal LaAlO3 by a two-step PLD process, *Journal of Materials Research*, **26** (2011) 770-774.

[114] J. Baniecki, R. Laibowitz, T. Shaw, P. Duncombe, D. Neumayer, D. Kotecki, H. Shen, Q. Ma, Dielectric relaxation of Ba 0.7 Sr 0.3 TiO 3 thin films from 1 mHz to 20 GHz, *Applied physics letters*, **72** (1998) 498-500.

[115] M. Yamamuka, T. Kawahara, T. Makita, A. Yuuki, K. Ono, Thermal desorption spectroscopy of (Ba, Sr) TiO3 thin films prepared by chemical vapor deposition, *Japanese journal of applied physics*, **35** (1996) 729.

[116] W. Li, Z. Xu, R. Chu, P. Fu, J. Hao, Sol–gel synthesis and characterization of Ba (1− x) SrxTiO3 ceramics, *Journal of Alloys and Compounds*, **499** (2010) 255-258.

[117] J. Wang, C. Zhang, J.-M. Liu, Revisiting the phase transitions in BaxSr1-xTiO3 at low doping range (x≤ 0.1), *Journal of Alloys and Compounds*, **749** (2018) 276-282.

[118] M. Jain, S. Majumder, R. Katiyar, A. Bhalla, Structural and dielectric properties of heterostructured BST thin films by sol–gel technique, *Thin Solid Films*, **447** (2004) 537-541.

[119] W.-J. Lee, I.-K. Park, G.-E. Jang, H.-G. Kim, Electrical properties and crystal structure of (Ba0. 5Sr0. 5) TiO3 thin films prepared on Pt/SiO2/Si by RF magnetron sputtering, *Japanese journal of applied physics*, **34** (1995) 196.

[120] S. Lu, X. Zhu, C.L. Mak, K. Wong, H. Chan, C. Choy, Compositionally graded epitaxial barium strontium titanate thin films derived from pulsed laser deposition, *Materials chemistry and physics*, **79** (2003) 164-168.

[121] F. Wang, J. Huang, Multifunctional Cu–BaTiO3 nanocomposite thin film fabricated via pulsed laser deposition, *Ceramics International*, **46** (2020) 25817-25821.

[122] E. Venkata Ramana, S. Yang, R. Jung, M. Jung, B. Lee, C. Jung, Ferroelectric and magnetic properties of Fe-doped BaTiO3 thin films grown by the pulsed laser deposition, *Journal of Applied Physics*, **113** (2013) 187219.

[123] R. Eason, *Pulsed laser deposition of thin films: applications-led growth of functional materials*, John Wiley & Sons, 2007.

[124] D.B. Chrisey, G.K. Hubler, Pulsed laser deposition of thin films, (1994).

[125] S. Friberg, P. Smith, Nonlinear optical glasses for ultrafast optical switches, *IEEE journal of quantum electronics*, **23** (1987) 2089-2094.

[126] M. Moran, C.-Y. She, R. Carman, Interferometric measurements of the nonlinear refractive-index coefficient relative to CS 2 in laser-system-related materials, *IEEE Journal of Quantum Electronics*, **11** (1975) 259-263.

[127] A. Owyoung, Ellipse rotation studies in laser host materials, *IEEE Journal of Quantum Electronics*, **9** (1973) 1064-1069.

[128] W.E. Williams, M. Soileau, E.W. Van Stryland, Optical switching and n2 measurements in CS2, *Optics communications*, **50** (1984) 256-260.

[129] M. Sheik-Bahae, A.A. Said, T.-H. Wei, D.J. Hagan, E.W. Van Stryland, Sensitive measurement of optical nonlinearities using a single beam, *IEEE journal of quantum electronics*, **26** (1990) 760-769.

[130] M. Saravanan, T.S. Girisun, G. Vinitha, Third-order nonlinear optical properties and power limiting behavior of magnesium ferrite under CW laser (532 nm, 50 mW) excitation, *Journal of materials science*, **51** (2016) 3289-3296.

[131] J. Kim, Y. Kim, Y.S. Kim, J. Lee, L. Kim, D. Jung, Large nonlinear dielectric properties of artificial BaTiO 3/SrTiO 3 superlattices, *Applied physics letters*, **80** (2002) 3581-3583.

[132] L. Sarkhosh, N. Mansour, Analysis of Z-scan measurement for large thermal nonlinear refraction in gold nanoparticle colloid, *Journal of Nonlinear Optical Physics & Materials*, **24** (2015) 1550014.

[133] I. Kumar, A. Khare, Modified Z-scan set-up using CCD for measurement of optical nonlinearity in PLD carbon thin film, *Optics & Laser Technology*, **77** (2016) 51-54.

[134] G. Vinitha, A. Ramalingam, Third-order optical nonlinearities and optical-limiting properties of a pararosanilin dye in liquid and solid media, *Laser physics*, **18** (2008) 1070-1073.

[135] K. Nagaraja, S. Pramodini, P. Poornesh, H. Nagaraja, Effect of annealing on the structural and nonlinear optical properties of ZnO thin films under cw regime, *Journal of Physics D: Applied Physics*, **46** (2013) 055106.

[136] T. Woldu, B. Raneesh, P. Sreekanth, M.R. Reddy, R. Philip, N. Kalarikkal, Size dependent nonlinear optical absorption in BaTiO3 nanoparticles, *Chemical Physics Letters*, **625** (2015) 58-63.

[137] P. Tang, A. Meier, D. Towner, B.W. Wessels, BaTiO 3 thin-film waveguide modulator with a low voltage–length product at near-infrared wavelengths of 0.98 and 1.55 μm, *Optics letters*, **30** (2005) 254-256.

[138] J. Hiltunen, J. Lappalainen, J. Puustinen, V. Lantto, H. Tuller, Size-dependent optical properties of BaTiO 3-SrTiO 3 superlattices, *Optics express*, **16** (2008) 8219-8228.

[139] C.R. Brundle, C.A. Evans, L. Wilson, S. Wilson, G. Wilson, *Encyclopedia of materials characterization: surfaces, interfaces, thin films*, Gulf Professional Publishing, 1992.

[140] R. Young, International Union of Crystallography, *The Rietveld method*, (1993).

[141] A.W. Varnes, F. Settle, Inductively coupled plasma mass spectrometry, *Handbook of instrumental techniques for analytical chemistry: Upper Saddle River, New Jersey, Prentice Hall*, (1997) 419-439.

[142] D. Nečas, P. Klapetek, Gwyddion: an open-source software for SPM data analysis, *Open Physics*, **10** (2012) 181-188.

[143] R. Swanepoel, Determination of the thickness and optical constants of amorphous silicon, *Journal of Physics E: Scientific Instruments*, **16** (1983) 1214.

[144] D.F. Swinehart, The beer-lambert law, *Journal of chemical education*, **39** (1962) 333.

[145] F. Abeles, *Optical properties of solids*, in, 1972.

[146] M. Cardona, Y.Y. Peter, *Fundamentals of semiconductors*, Springer, 2005.

[147] D.D. Smith, Y. Yoon, R.W. Boyd, J.K. Campbell, L.A. Baker, R.M. Crooks, M. George, Z-scan measurement of the nonlinear absorption of a thin gold film, *Journal of applied physics*, **86** (1999) 6200-6205.

[148] R.W. Boyd, The nonlinear optical susceptibility, *Nonlinear optics*, **3** (2008) 1-67.

[149] E.W. Van Stryland, Y.-Y. Wu, D.J. Hagan, M. Soileau, K.J.J.B. Mansour, Optical limiting with semiconductors, **5** (1988) 1980-1988.

[150] V. Kumari, V. Kumar, B. Malik, R. Mehra, D. Mohan, Nonlinear optical properties of erbium doped zinc oxide (EZO) thin films, *Optics Communications*, **285** (2012) 2182-2188.

[151] K. Nagaraja, S. Pramodini, A.S. Kumar, H. Nagaraja, P. Poornesh, D.J.o.m. Kekuda, Third-order nonlinear optical properties of Mn doped ZnO thin films under cw laser illumination, **35** (2013) 431-439.

[152] A.R. Barron, Physical methods in chemistry and nano science, (2015).

[153] P. Yeh, *Introduction to photorefractive nonlinear optics*, Wiley-Interscience, 1993.

[154] F.-S. Yen, H.-I. Hsiang, Y.-H. Chang, Cubic to tetragonal phase transformation of ultrafine BaTiO3 crystallites at room temperature, *Japanese journal of applied physics*, **34** (1995) 6149.

[155] J. Feinberg, D. Heiman, A. Tanguay, R. Hellwarth, Photorefractive effects and light-induced charge migration in barium titanate, in: Landmark Papers On Photorefractive Nonlinear Optics, World Scientific, 1995, pp. 69-77.

[156] H.W. Lee, S. Moon, C.H. Choi, D.K. Kim, Synthesis and size control of tetragonal barium titanate nanopowders by facile solvothermal method, *Journal of the American Ceramic Society*, **95** (2012) 2429-2434.

[157] B. Cullity, S. Stock, Diffraction III: real samples, *Elements of X-ray Diffraction*, **3** (2001) 174-177.

[158] C. Shu, *Investigation of the structural and functional properties of lead-free barium calcium zirconate titanate piezoceramics*, in, University of Birmingham, 2018.

[159] H. Guo, L. Liu, H. Lu, S. Ding, Z. Chen, Structural and transport properties of heteroepitaxial BaNbxTi1− xO3 (x= 0.05, 0.2) thin films, *Thin solid films*, **497** (2006) 341-346.

[160] M. DiDomenico Jr, S. Wemple, S. Porto, R. Bauman, Raman Spectrum of Single-Domain BaTi O 3, *Physical Review*, **174** (1968) 522.

[161] Q. Hao, J. Pang, Y. Zhang, J. Wang, L. Ma, O.G.J.A.O.M. Schmidt, Boosting the photoluminescence of monolayer MoS2 on high-density nanodimer arrays with sub-10 nm gap, **6** (2018) 1700984.

[162] M. Selvaraj, V. Venkatachalapathy, J. Mayandi, S. Karazhanov, J.M. Pearce, Preparation of meta-stable phases of barium titanate by Sol-hydrothermal method, *AIP Advances*, **5** (2015) 117119.

[163] M. Singh, B. Yadav, A. Ranjan, M. Kaur, S. Gupta, Synthesis and characterization of perovskite barium titanate thin film and its application as LPG sensor, *Sensors and Actuators B: Chemical*, **241** (2017) 1170-1178.

[164] R. Katiyar, Y.I.J.V.s. Yuzyuk, Stress manipulation in ferroelectric thin films and superlattices, **45** (2007) 108-111.

[165] J. Den Toonder, J. Van Dommelen, F.J.M. Baaijens, S.i.M. Science, Engineering, The relation between single crystal elasticity and the effective elastic behaviour of polycrystalline materials: theory, measurement and computation, **7** (1999) 909.

[166] J. Den Toonder, J. Van Dommelen, F. Baaijens, The relation between single crystal elasticity and the effective elastic behaviour of polycrystalline materials: theory, measurement and computation, *Modelling and Simulation in Materials Science and Engineering*, **7** (1999) 909.

[167] A. Gajović, J.V. Pleština, K. Žagar, M. Plodinec, S. Šturm, M. Čeh, Temperature-dependent Raman spectroscopy of BaTiO3 nanorods synthesized by using a template-assisted sol–gel procedure, *Journal of Raman Spectroscopy*, **44** (2013) 412-420.

[168] K.C. Verma, V. Gupta, J. Kaur, R. Kotnala, Raman spectra, photoluminescence, magnetism and magnetoelectric coupling in pure and Fe doped BaTiO3 nanostructures, *Journal of Alloys and Compounds*, **578** (2013) 5-11.

[169] M. El Marssi, F. Le Marrec, I. Lukyanchuk, M. Karkut, Ferroelectric transition in an epitaxial barium titanate thin film: Raman spectroscopy and x-ray diffraction study, *Journal of applied physics*, **94** (2003) 3307-3312.

[170] Q. Jia, J. Smith, L. Chang, W. Anderson, Characteristics of BaTiO3 thin films on Si deposited by rf magnetron sputtering, *Philosophical Magazine B*, **77** (1998) 163-175.

[171] M. Kamalasanan, N.D. Kumar, S. Chandra, Structural and microstructural evolution of barium titanate thin films deposited by the sol-gel process, *Journal of applied physics*, **76** (1994) 4603-4609.

[172] K. Chen, H. Gu, Y. Cai, J. Xiong, A.J.J.o.a. Wang, compounds, Fe/SrBi2Nb2O9 composite thin films with large third-order optical nonlinearities, **476** (2009) 635-638.

[173] K. Upadhya, U. Deekshitha, A. Antony, A. Ani, I. Kityk, J. Jedryka, A. Wojciechowski, K. Ozga, P. Poornesh, S.D.J.O.M. Kulkarni, Second and third harmonic nonlinear optical process in spray pyrolysed Mg: ZnO thin films, **102** (2020) 109814.

[174] Y. Guang, W. Wei-Tian, Y. Guo-Zhen, C. Zheng-Hao, Enhanced nonlinear optical properties of laser deposited Ag/BaTiO3 nanocomposite films, *Chinese physics letters*, **20** (2003) 924.

[175] J. John, S. Chalana, R. Prabhu, V.M. Pillai, Effect of oxygen pressure on the structural and optical properties of BaSnO 3 films prepared by pulsed laser deposition method, *Applied Physics A*, **125** (2019) 155.

[176] T.K.O. Vu, D.U. Lee, E.K. Kim, The effect of oxygen partial pressure on band gap modulation of Ga2O3 grown by pulsed laser deposition, *Journal of Alloys and Compounds*, **806** (2019) 874-880.

[177] J. Zhang, D. Cui, Y. Zhou, L. Li, Z. Chen, M. Szabadi, P. Hess, Effect of oxygen pressure on the orientation, lattice parameters, and surface morphology of laser ablated BaTiO3 thin films, *Thin Solid Films*, **287** (1996) 101-103.

[178] Z. Saroukhani, N. Tahmasebi, S.M. Mahdavi, A. Nemati, Effect of working pressure and annealing temperature on microstructure and surface chemical composition of barium strontium titanate films grown by pulsed laser deposition, *Bulletin of Materials Science*, **38** (2015) 1645-1650.

[179] S. Pattipaka, J.P. Goud, G.P. Bharti, K.J. Raju, A. Khare, D. Pamu, Effect of oxygen partial pressure on nonlinear optical and electrical properties of BNT–KNNG composite thin films, *Journal of Materials Science: Materials in Electronics*, **31** (2020) 2986-2996.

[180] L. Huang, Z. Chen, J.D. Wilson, S. Banerjee, R.D. Robinson, I.P. Herman, R. Laibowitz, S. O'Brien, Barium titanate nanocrystals and nanocrystal thin films: Synthesis, ferroelectricity, and dielectric properties, *Journal of Applied Physics*, **100** (2006) 034316.

[181] U.D. Venkateswaran, V.M. Naik, R. Naik, High-pressure Raman studies of polycrystalline BaTiO 3, *Physical Review B*, **58** (1998) 14256.

[182] P. Nagaraju, Y. Vijayakumar, R. Reddy, Effect of oxygen partial pressure on the microstructural, optical and gas sensing characterization of nanostructured Gd doped ceria thin films deposited by pulsed laser deposition, *Journal of Asian Ceramic Societies*, **5** (2017) 402-409.

[183] Y. Guang, W. Huan-Hua, T. Guo-Tai, J. An-Quan, Z. Yue-Liang, Y. Guo-Zhen, C. Zheng-Hao, Large third-order nonlinear optical susceptibility of Rh-doped BaTiO3 thin films prepared by pulsed laser deposition, *Chinese Physics Letters*, **18** (2001) 1598.

[184] J. Xu, W. Ji, Z. Shen, S. Tang, X. Ye, D. Jia, X. Xin, Preparation and characterization of CuO nanocrystals, *Journal of Solid State Chemistry*, **147** (1999) 516-519.

[185] A. Shukla, R. Choudhary, A. Thakur, D. Pradhan, Structural, microstructural and electrical studies of La and Cu doped BaTiO3 ceramics, *Physica B: Condensed Matter*, **405** (2010) 99-106.

[186] S. Horzum, E. Torun, T. Serin, F. Peeters, Structural, electronic and optical properties of Cu-doped ZnO: experimental and theoretical investigation, *Philosophical Magazine*, **96** (2016) 1743-1756.

[187] Q.-j. Lin, W. Jing, S.-m. Yang, Z.-d. Jiang, C.-y. Wang, Agglomeration and dendritic growth of Cu/Ti/Si thin film, *Journal of Nanomaterials*, **2014** (2014).

[188] N. Venugopal, A. Mitra, Optical transparency of ZnO thin film using localized surface plasmons of Ag nanoislands, *Optical Materials*, **35** (2013) 1467-1476.

[189] H. Guo, L. Liu, Z. Chen, S. Ding, H. Lu, K.-j. Jin, Y. Zhou, B. Cheng, Structural and optical properties of BaTiO3 ultrathin films, *EPL (Europhysics Letters)*, **73** (2005) 110.

[190] N. Kainbayev, M. Sriubas, D. Virbukas, Z. Rutkuniene, K. Bockute, S. Bolegenova, G. Laukaitis, Raman Study of Nanocrystalline-Doped Ceria Oxide Thin Films, *Coatings*, **10** (2020) 432.

[191] I. Alessandri, J.R. Lombardi, Enhanced Raman scattering with dielectrics, *Chemical reviews*, **116** (2016) 14921-14981.

[192] J. Tauc, The optical properties of solids, *The Optical Properties of Solids*, (1966).

[193] S. Ramakanth, K. James Raju, Band gap narrowing in BaTiO3 nanoparticles facilitated by multiple mechanisms, *Journal of Applied Physics*, **115** (2014) 173507.

[194] N. Venugopal, A.J.O.M. Mitra, Optical transparency of ZnO thin film using localized surface plasmons of Ag nanoislands, **35** (2013) 1467-1476.

[195] R.D. Averitt, S.L. Westcott, N.J. Halas, Ultrafast optical properties of gold nanoshells, *JOSA B*, **16** (1999) 1814-1823.

[196] R. Ganeev, A. Ryasnyanskii, A. Stepanov, T. Usmanov, Nonlinear absorption in dielectric layers containing copper nanoparticles, *Physics of the Solid State*, **45** (2003) 1355-1359.

[197] M. Moreira, M. Gurgel, G. Mambrini, E. Leite, P. Pizani, J.A. Varela, E. Longo, Photoluminescence of barium titanate and barium zirconate in multilayer disordered thin films at room temperature, *The Journal of Physical Chemistry A*, **112** (2008) 8938-8942.

[198] L. Maneeshya, P. Thomas, K. Joy, Effects of annealing temperature on the photoluminescence of RF sputtered Barium titanate thin films, *Materials Science in Semiconductor Processing*, **30** (2015) 688-693.

[199] A. Rubano, D. Paparo, F.M. Granozio, U. Scotti di Uccio, L. Marrucci, Blue luminescence of SrTiO 3 under intense optical excitation, *Journal of Applied Physics*, **106** (2009) 103515.

[200] T. Sequinel, I. Garcia, S. Tebcherani, E. Kubaski, L. Oliveira, M.S. Li, E. Longo, J.A. Varela, Red shift and higher photoluminescence emission of CCTO thin films undergoing pressure treatment, *Journal of alloys and compounds*, **583** (2014) 488-491.

[201] B. Allabergenov, U. Shaislamov, H. Shim, M.-J. Lee, A. Matnazarov, B. Choi, Effective control over near band-edge emission in ZnO/CuO multilayered films, *Optical Materials Express*, **7** (2017) 494-502.

[202] S. Paul, P. Chetri, A. Choudhury, Effect of manganese doping on the optical property and photocatalytic activity of nanocrystalline titania: Experimental and theoretical investigation, *Journal of alloys and compounds*, **583** (2014) 578-586.

[203] K. Puech, W. Blau, A. Grund, C. Bubeck, G.J.O.l. Cardenas, Picosecond degenerate four-wave mixing in colloidal solutions of gold nanoparticles at high repetition rates, **20** (1995) 1613-1615.

[204] D.W. Brandl, N.A. Mirin, P. Nordlander, Plasmon modes of nanosphere trimers and quadrumers, *The Journal of Physical Chemistry B*, **110** (2006) 12302-12310.

[205] W. Ji-Fei, L. Hong-Jian, Z. Zi-You, L. Xue-Yong, L. Ju, Y. Hai-Yan, Tunable surface-plasmon-resonance wavelength of silver island films, *Chinese Physics B*, **19** (2010) 117310.

[206] M. Horowitz, B. Fischer, Y. Barad, Y. Silberberg, Photorefractive effect in a BaTiO 3 crystal at the 1.5-μm wavelength regime by two-photon absorption, *Optics letters*, **21** (1996) 1120-1122.

[207] J. Padilla, E. Xuriguera, L. Rodríguez, A. Vannozzi, M. Segarra, G. Celentano, M. Varela, Epitaxial Growth of SrTiO 3 Films on Cube-Textured Cu-Clad Substrates by PLD at Low Temperature Under Reducing Atmosphere, *Nanoscale research letters*, **12** (2017) 1-7.

[208] E. Drożdż, A. Koleżyński, The structure, electrical properties and chemical stability of porous Nb-doped SrTiO 3–experimental and theoretical studies, *RSC advances*, **7** (2017) 28898-28908.

[209] A. Souza, G. Santos, B. Barra, W. Macedo Jr, S. Teixeira, C. Santos, A. Senos, L. Amaral, E. Longo, Photoluminescence of SrTiO3: influence of particle size and morphology, *Crystal growth & design*, **12** (2012) 5671-5679.

[210] Y. Du, G. Chen, M. Zhang, Investigation of structural phase transition in polycrystalline SrTiO3 thin films by Raman spectroscopy, *Solid state communications*, **130** (2004) 577-580.

[211] W. Kleemann, A. Albertini, M. Kuss, R. Lindner, Optical detection of symmetry breaking on a nanoscale in SrTiO3: Ca, *Ferroelectrics*, **203** (1997) 57-74.

[212] V.I. Merkulov, J.R. Fox, H.-C. Li, W. Si, A. Sirenko, X. Xi, Metal–oxide bilayer Raman scattering in SrTiO 3 thin films, *Applied physics letters*, **72** (1998) 3291-3293.

[213] M.L. Moreira, V.M. Longo, W. Avansi Jr, M.M. Ferrer, J. Andres, V.R. Mastelaro, J.A. Varela, E. Longo, Quantum mechanics insight into the microwave nucleation of SrTiO3 nanospheres, *The Journal of Physical Chemistry C*, **116** (2012) 24792-24808.

[214] A.S. Zoolfakar, R.A. Rani, A.J. Morfa, A.P. O'Mullane, K. Kalantar-Zadeh, Nanostructured copper oxide semiconductors: a perspective on materials, synthesis methods and applications, *journal of materials chemistry c*, **2** (2014) 5247-5270.

[215] E.W. Van Stryland, M. Woodall, H. Vanherzeele, M. Soileau, Energy band-gap dependence of two-photon absorption, *Optics letters*, **10** (1985) 490-492.

[216] Y. Pepe, A. Karatay, Y.O. Donar, E.A. Yildiz, A. Sınağ, H. Unver, A. Elmali, Enhanced nonlinear absorption coefficient and low optical limiting threshold of NiO nanocomposite films, *Optik*, **227** (2021) 165975.

[217] L. Zhou, P. Vilarinho, J. Baptista, Dependence of the structural and dielectric properties of Ba1-xSrxTiO3 ceramic solid solutions on raw material processing, *Journal of the European Ceramic Society*, **19** (1999) 2015-2020.

[218] B. Jaffe, W. Cook, H. Jaffe, Piezoelectric Ceramics Academic Press London, in: JCPDS 71-2171, 1971.

[219] B. Vigneshwaran, P. Kuppusami, S. Ajithkumar, H. Sreemoolanadhan, Study of low temperature-dependent structural, dielectric, and ferroelectric properties of Ba x Sr (1− x) TiO 3 (x= 0.5, 0.6, 0.7) ceramics, *Journal of Materials Science: Materials in Electronics*, **31** (2020) 10446-10459.

[220] S.C. Roy, G. Sharma, M. Bhatnagar, S. Samanta, Novel ammonia-sensing phenomena in sol–gel derived Ba0. 5Sr0. 5TiO3 thin films, *Sensors and Actuators B: Chemical*, **110** (2005) 299-303.

[221] P. Bao, T. Jackson, X. Wang, M. Lancaster, Barium strontium titanate thin film varactors for room-temperature microwave device applications, *Journal of physics D: applied physics*, **41** (2008) 063001.

[222] B. Vigneshwaran, P. Kuppusami, S. Ajithkumar, H.J.J.o.M.S.M.i.E. Sreemoolanadhan, Study of low temperature-dependent structural, dielectric, and ferroelectric properties of Ba x Sr (1− x) TiO 3 (x= 0.5, 0.6, 0.7) ceramics, **31** (2020) 10446-10459.

[223] D.A. Tenne, X. Xi, Raman spectroscopy of ferroelectric thin films and superlattices, *Journal of the American Ceramic Society*, **91** (2008) 1820-1834.

[224] S. Dutta, S. Chattopadhyay, M. Sutradhar, A. Sarkar, M. Chakrabarti, D. Sanyal, D. Jana, Defects and the optical absorption in nanocrystalline ZnO, *Journal of Physics: Condensed Matter*, **19** (2007) 236218.

[225] R. Reshmi, R. Sreeja, M. Jayaraj, J. James, M. Sebastian, Linear and nonlinear optical properties of rare earth doped of Ba 0.7 Sr 0.3 TiO 3 thin films, *Applied Physics B*, **96** (2009) 433-437.

[226] R.W. Boyd, *Nonlinear optics*, Academic press, 2020.

[227] V. Kapustianyk, B. Turko, A. Kostruba, Z. Sofiani, B. Derkowska, S. Dabos-Seignon, B. Barwiński, Y. Eliyashevskyi, B. Sahraoui, Influence of size effect and sputtering conditions on the crystallinity and optical properties of ZnO thin films, *Optics Communications*, **269** (2007) 346-350.

[228] K. Nagaraja, S. Pramodini, A.S. Kumar, H. Nagaraja, P. Poornesh, D. Kekuda, Third-order nonlinear optical properties of Mn doped ZnO thin films under cw laser illumination, *optical materials*, **35** (2013) 431-439.

[229] M. Gaidi, M. Chaker, P. Ndione, R. Morandotti, B. Bessais, Microstructural and optical properties of Ba 0.5 Sr 0.5 Ti O 3 thin film deposited by pulsed laser deposition for low loss waveguide applications, *Journal of applied physics*, **101** (2007) 063107.

List of Publications

Journal Publications

1. **Sasmita Behera** and Alika Khare, "Influence of substrate temperature and oxygen pressure on the structural and optical properties of polycrystalline $BaTiO_3$ thin films grown by PLD" *Material Science in Semiconductor processing* **140** (2022) 106379.
2. **Sasmita Behera** and Alika Khare, "Tuning of optical properties of Cu doped BTO thin films fabricated by PLD technique" 2019 Workshop on Recent Advances in Photonics (WRAP), *IEEE conference proceeding*, 2019, pp. 1-3.
3. **Sasmita Behera** and Alika Khare "Linear and Nonlinear Optical Properties of $BaTiO_3$ and $Ba_{0.5}Sr_{0.5}TiO_3$ Thin Films Fabricated by Pulsed Laser Deposition Technique", International Conference on Optoelectronics and Nanomaterial for Advanced Technology, Cochin University and Technology Kochi, *AIP conference proceeding* 2082, 040006 (2019).
4. **Sasmita Behera** and Alika Khare, "Characterization of Sapphire (α-Al_2O_3) Thin Film Fabricated by Pulsed Laser Deposition", International Conference on Fiber Optics and Photonics, *Optical Society of America*, 15 (2016), pp. P1A.
5. **Sasmita Behera** and Alika Khare, "The effect of Cu nano-layer on linear, nonlinear, and photoluminescence properties of $BaTiO_3$ thin films fabricated via PLD" (to be submitted).
6. **Sasmita Behera** and Alika Khare, "Influence of Cu nano-layer on linear and nonlinear optical properties of $SrTiO_3$ thin films**"** (to be submitted).
7. **Sasmita Behera** and Alika Khare, "Linear and nonlinear optical properties of PLD deposited $Ba_{1-x}Sr_xTiO_3$ ($0 \leq x \leq 1$) thin films" (to be submitted).
8. **Sasmita Behera** and Alika Khare, "Influence of Cu nano-layer on optical limiting in BTO, STO, and BST PLD thin films**"** (to be communicated).

Conferences attended in National /International conference

1. **Sasmita Behera** and Alika Khare, Characterization of sapphire (α-Al_2O_3) thin film fabricated by pulsed laser deposition, "International Conference on Fibre Optics and Photonics" held at IIT Kanpur during 2-6 December 2016.
2. Gobinda Pradhan, Rahul Kesarwani, **Sasmita Behera**, Ashwini K. Sharma, and Alika Khare, "Study of surface morphology and optical properties of thin films grown via PLD" held at Research Conclave, IIT Guwahati during 16-19 March 2016.

3. **Sasmita Behera** and Alika Khare, "Effect of substrate temperature on $BaTiO_3$ thin films fabricated by pulsed laser deposition technique'', International conference on thin films (ICTF 2017), Department of Physics, CSIR-National Physical Laboratory New Delhi, India, 14-17 November 2017.

4. **Sasmita Behera** and Alika Khare, "Structural and optical properties of $BaTiO_3$ thin films fabricated by pulsed laser deposition technique" held at Research Conclave, IIT Guwahati during 8-11 March 2018.

5. **Sasmita Behera**, Amandeep Kaur, and Alika Khare, "Structural and optical properties of $SrTiO_3$ thin films fabricated by pulsed laser deposition technique," National Conference on Recent Advances in Science and Technology (NCRAST-2018), Assam Science and Technology University, Assam, India, 15-17 March 2018.

6. **Sasmita Behera** and Alika Khare "Effect of Cu nanolayer on linear and nonlinear optical properties of $BaTiO_3$ thin films", 5th International Conference on Nanoscience and Nanotechnology (ICONN 2019), SRM Institute of Science and Technology Chennai, India January 28-30, 2019.

7. **Sasmita Behera** and Alika Khare "Linear and nonlinear optical properties of $BaTiO_3$ and $Ba_{0.5}Sr_{0.5}TiO_3$ thin films fabricated by pulsed laser deposition technique", International Conference on Optoelectronics and Nanomaterial for Advanced Technology (ICONMAT 2019), Cochin University and Technology Kochi, India January 3-5, 2019.

8. **Sasmita Behera** and Alika Khare, "Structural and optical properties of Perovskite thin films fabricated by pulsed laser deposition technique" held at Research Conclave, IIT Guwahati during 14-17 March 2019.

9. **Sasmita Behera** and Alika Khare, "Composition dependent structural and optical properties of PLD deposited BST thin films," National Conference on Recent Advances in Science and Technology (NCRAST-2019), NEDFi House, NEDFi Convention Center, Dispur-Guwahati, Assam, India, 15-17 May 2019.

Workshops/ Schools attended

1. TEQIP Symposium to celebrate the 2015 international year of light, 31 October 2015, Organized by Department of Physics, IIT Guwahati.

2. SERB School on "Optical Metrology" held in Tezpur University Assam during 1-21 June 2016.

3. National workshop on "Advanced Probing Technique in TEM" held at Department of Physics, IIT Guwahati during 15-16 February 2016.

4. One- Day Workshop on Vacuum Technology and its Application in Optical Science, 19 August 2017 organized by SPIE student chapter, IIT Guwahati.

5. Technical Education Quality Improvement Programme (TEQIP) short term course on "Nanomaterials and Smart Devices" held at Centre for Educational Technology (CET) IIT Guwahati during 17-21 September 2018.

6. **Sasmita Behera**, and Alika Khare, "Tuning of optical properties of Cu doped BTO thin films fabricated by PLD Technique" Workshop on Recent Advances in Photonics (WRAP-2019) IIT Guwahati during 13-14 December 2019.